5-2016

Development and Application of 3-D Fuel Performance Modeling to Assess Missing Pellet Surface Influence on Pellet Clad Interaction and Clad Failure

Nathan Allen Capps
University of Tennessee - Knoxville, ncapps@utk.edu

To the Graduate Council:

I am submitting herewith a dissertation written by Nathan Allen Capps entitled "Development and Application of 3-D Fuel Performance Modeling to Assess Missing Pellet Surface Influence on Pellet Clad Interaction and Clad Failure." I have examined the final electronic copy of this dissertation for form and content and recommend that it be accepted in partial fulfillment of the requirements for the degree of Doctor of Philosophy, with a major in Nuclear Engineering.

Brian D. Wirth, Major Professor

We have read this dissertation and recommend its acceptance:

William Weber, Lawerence Miller, Ivan Maldonado

Accepted for the Council:
Dixie L. Thompson

Vice Provost and Dean of the Graduate School

(Original signatures are on file with official student records.)

Development and Application of 3-D Fuel Performance Modeling to Assess Missing Pellet Surface Influence on Pellet Clad Interaction and Clad Failure

A Dissertation Presented for the
Doctor of Philosophy
Degree
The University of Tennessee, Knoxville

Nathan Allen Capps
May 2016

Abstract

In the late 1970s PCI related failures caused the implementation of startup ramp restrictions. These ramp restrictions where intended to reduce the stresses caused by pellet cladding contact. These ramp restrictions had a significant impact on Westinghouse fueled PWRs, reducing PCI related failure until 2003. Through investigation into these fuel rod failures lead to the conclusion that missing pellet surfaces (MPS) were the root cause of the failures. MPS are local geometric defects in nuclear fuel pellets that result from pellet mishandling or the manufacturing process. The presence of MPS defects can cause stress concentrations in the clad of sufficient magnitude to produce through-wall cladding failure for certain combinations of fuel burnup, and reactor power level or power change. Consequently, the impact of potential MPS defects has significant ly limited the rate of power increase, or ramp rate, in both pressurized and boiling water reactors (PWRs and BWRs, respectively). Improved three-dimensional (3-D) fuel performance models of MPS defect geometry can provide better understanding of the probability for pellet clad mechanical interaction (PCMI), and correspondingly the available margin against cladding failure by stress corrosion cracking (SCC). The Bison fuel performance code has been developed within the Consortium of Advanced Simulations of Light Water Reactors (CASL) to consider the inherently multi-physics and multi-dimensional mechanisms that control fuel behavior, including cladding stress concentrations resulting from MPS defects. Bison is built upon the Multi-physics Object-Oriented Simulation Environment (MOOSE) developed at Idaho National Laboratory (INL). MOOSE is a massively parallel finite element computational system that uses a Jacobian-free, Newton-Krylov (JFNK) method to solve coupled systems of non-linear partial differential equations. In addition, the MOOSE framework provides the ability to effectively use massively parallel computational capabilities needed to create high fidelity 3-D models of a fuel rod, as well as full-length R-Z rods, and R-Theta geometric representation. This PhD dissertation documents my contributions to the development of Bison, specifically focused on verification and validation of a 2-D, axi-symmetric version of Bison through benchmarking comparisons to Falcon model predictions and Halden Instrumented Fuel Assembly (IFA) experiments of both thermal and mechanical behavior. Initial benchmark comparisons indicate that Bison predictions agree quite well with 2-D Falcon predictions and Halden experimental data on fuel centerline temperature but that further developments are necessary for some models, including fission gas release and gaseous swelling. The mechanical behavior benchmarking study has compared predictions of clad deformation to dilatational measurements, and the results show promising agreement. Subsequently, this dissertation documents my evaluation of the cladding hoop stress distributions as a function of MPS defect geometry and the presence of discrete pellet cracks for a set of typical operating conditions in a PWR fuel rod, as a function of reactor operating history. These results provide a first step in a probabilistic approach to assess cladding failure during power maneuvers. My research provides insight into how varying pellet defect geometries affect the distribution of the cladding stress, as well as the temperature distributions within the fuel and clad; and are used to develop stress concentration factors for comparing 2-D and 3-D models. Finally, the objective of this dissertation is to develop a methodology to determine rod failure, and then to utilize the resulting failure criteria to evaluate specific historical MPS and PCI failures.

Table of Contents

List of Tables

List of Figures

Chapter 1: Introduction

1.1 Overview of Pellet-Cladding Interactions

Crack formation at the inner surface of zirconium alloy cladding by stress corrosion cracking (SCC) has been present in LWR fuel since the early days of reactor operation [1-4]. This process, commonly referred to as pellet-cladding interaction (PCI), is a consequence of the UO_2 ceramic pellets developing radial crack producing shear stresses on the Zr cladding. The small residual gap between the pellet and cladding tube, along with high operating temperatures and volatile fission products leads to the process of SCC. PCI represents an important failure mechanism in modern LWR fuel performance. Losses are measured by reductions in plant capacity factor and have historically ranged from 2 to 4% due to power restrictions imposed to mitigate PCI failures.

There are many nuclear reactors designs in the world today, but there are only two types of commercial nuclear reactors in the US, pressurized water reactors (PWRs) and boiling water reactors (BWRs). PCI was first in BWRs in the 70s, but since the early 90s PWRs have seen a rise in PCI related failures. The work in this dissertation will focus on PCI related failure in a PWR. Westinghouse PWR designs use a 12 foot active core housed in 17 by 17 fuel assemblies, and in these fuel assemblies each rod can hold ~372 fuel pellets. Steady state linear heat rates range from 4 to 7 kW/ft. Table 1-1 shows typical geometries and reactor operating conditions.

Table 1-1. Typical fuel rod geometries and reactor operating conditions for a PWR [20].

Cladding outer diameter (inch)	0.360
Cladding inner diameter (inch)	0.3375
Cladding Material	ZIRLO^{TM}
Pellet outer diameter (inch)	0.3088
Radial gap (mils)	28.7
Enrichment (%)	4.6-4.95
Fuel density [% of T.D.]	95
Internal gas pressure [He] (psig)	275
Dished pellet	Yes
Fuel stack length (inch)	144.0
Coolant Temperature (K)	293
Coolant Pressure (psig)	2257

The occurrence of PCI failures is associated with an increase in the local power over a short time, in fuel that has been exposed to previous irradiation cycles. A schematic of the mechanisms active in the classical PCI process is presented in Figure 1. This figure shows a representation of a cracked pellet impinging on the cladding as a consequence of thermal expansion of the pellet. The tangential and shear forces applied to the cladding by the pellet are a function of the equilibrium pellet-cladding gap size as well as the residual contact pressure at the start of the transient, the power level at gap closure, the friction conditions between the pellet and cladding, and the maximum local power. Above a certain level of localized cladding stress and fuel temperature, a number of volatile fission products are released from the hotter central part of the pellet and begin to react with the cladding inner surface. The volatile fission products are believed to assist in crack nucleation as well as crack propagation, provided the local stress levels remain above a threshold condition. As highlighted in Figure 1, the circumstances that lead to PCI include a complex interaction between thermal, mechanical, and chemical processes active in the fuel rod.

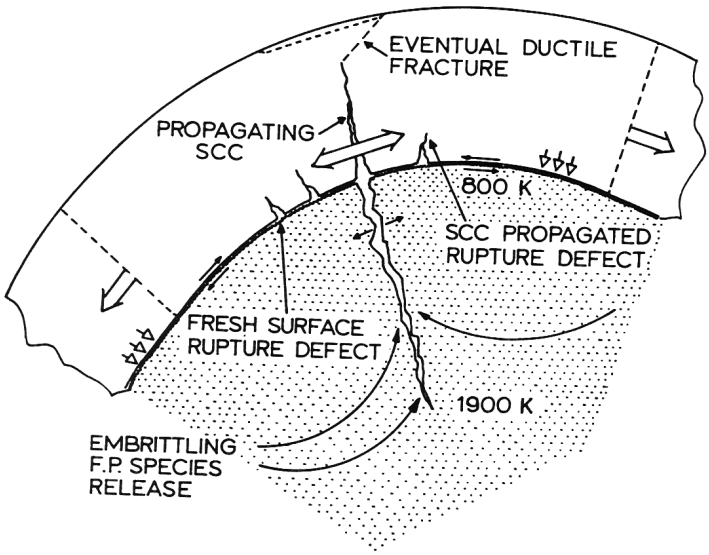

Figure 1-1. Schematic of the pellet-cladding interaction mechanisms seen during normal operations as well as during a failure event, as reproduced from Ref. [6].

The basic mechanisms of PCI leading to SCC can be categorized into two main processes. The first category are those mechanisms that establish the equilibrium or initial fuel rod conditions prior to a transient condition, such as fuel pellet cracking induced by thermal gradients in the fuel, reduction of the pellet-cladding gap by fuel swelling and fuel fragment relocation, fission product induced swelling of the fuel, and irradiation creep of the cladding, and fission gas release into the pellet-cladding gap. The second category are those mechanisms that occur during and shortly following an increase in power, such as rapid pellet thermal expansion

leading to high contract pressures with the cladding, localized cladding hoop stresses adjacent to a pellet crack due to induced shear forces, the release of volatile fission products, such as iodine, cadmium and cesium, swelling due to bubbles containing gaseous fission products in the fuel, and fuel and cladding stress relaxation due to thermal creep and pellet fragment accommodation.

The mechanisms listed above all depend on the operating history of the fuel rod since these are functions of the local conditions of temperature, burnup, fast flux, and fast fluence. This fact leads to the concept of conditioned versus de-conditioned states in the fuel rod. Simply put, these definitions relate to the ability of the fuel and clad to withstand a power change without failure. Fuel rod conditioning is a process of increasing the fuel power to a desired power level at a rate below a critical rate which would cause cladding damage. A conditioned fuel rod can accommodate a certain power change with minimal increase in cladding stress whereas fuel in a de-conditioned state will experience a sizeable stress increase in the clad, leading to the potential for PCI. Operating fuel is always transitioning from one state to another, depending on the local power conditions. The ability to evaluate the potential for PCI failure must include a means to determine the impact of operation on the state of the fuel and determine whether the fuel is in a conditioned or de-conditioned state during the transient.

Extensive experimental research has been performed to gain a better understanding of the mechanisms leading to PCI failures in the UO_2 pellet/zirconium-alloy cladding fuel system using separate effects tests, power ramp tests in material test reactors, and post-irradiation examination of experimental and commercial fuel rods [2]. These investigations have shown that a complicated combination of material susceptibility, local fission product environment, and pellet-cladding mechanical interaction can lead to local chemical attack of the cladding by SCC. The relationship between the different elements leading to PCI is highlighted in a classical Venn diagram shown in Figure 1-2.

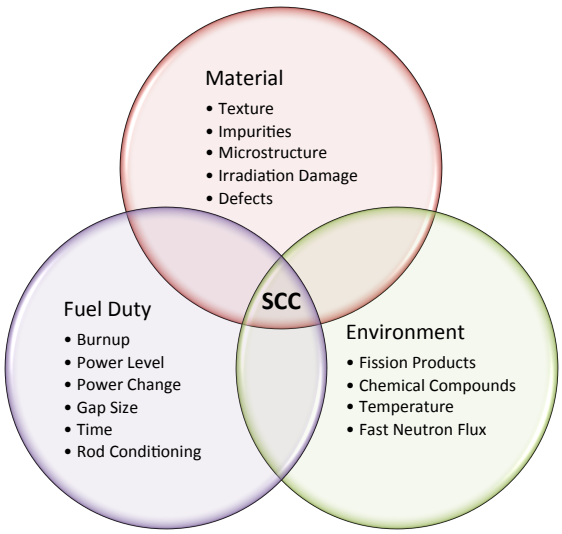

Figure 1-2. Venn diagram describing the key elements of PCI as seen in LWR fuel, as reproduced from Ref [2].

This diagram illustrates the relationship between the material susceptibility (blue circle), the corrosive environment (red circle), and the stress state (green circle). The necessary conditions in all three elements must be achieved before a SCC can initiate and propagate in the cladding, as indicated by the central overlapping region.

This understanding has been used as the basis for establishing power operating restrictions, which allow for stress relaxation to occur (green circle), or implementing fuel rod designs changes, which in turn reduces the material susceptibility (blue circle), that may mitigate the occurrence of PCI [6]. However, PCI failures in LWRs continue to occur, indicative of the complex nature of the processes leading to SCC in operating fuel rods, and the complex interplay with reactor operation and core loading patterns. These complexities arise from several sources, including the state of contact between the pellet and cladding prior to a power maneuver, the basic mechanisms of fission product attack at the cladding inner surface, as well as the irradiated material mechanical behavior during stress relaxation. Combined with uncertainties in local power and thermal-hydraulic conditions, the interaction of these complexities make predicting the conditions of PCI induced cladding failure difficult to completely prevent, and as a result, more conservative operating strategies as well as conservative fuel design methods have been selected by plant operators.

Experiences from operation of LWR fuel during power maneuvers have found that the processes leading to cladding failure by PCI can be separated into two separate classifications based on their time of discovery. Figure 3 shows examples of each type of cladding failure as observed in post-irradiation examination metallography/ceramography images.

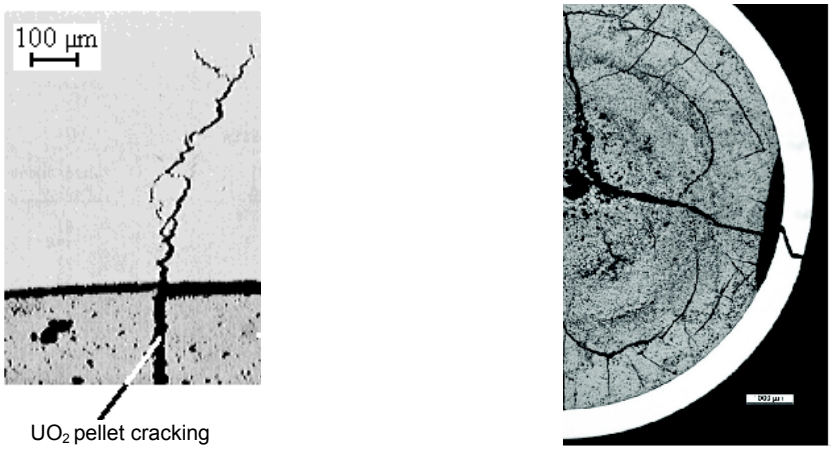

(a) (b)

Figure 1-3. Example of (a) Classical PCI and (b) Non-Classical PCI, as reproduced from Ref [8,9].

Classical PCI is driven by the localized strains in the vicinity of a pellet crack in the presence of a chemical agent, generally considered to be contributed to the fission products iodine and cesium, that gives rise to corrosion induced crack nucleation in the cladding material [1], see Figure 3(a). Non-classical PCI failure is associated with the presence of a manufacturing-related flaw in the cladding or pellet that leads to cladding stress concentration, see Figure 3(b).

During the last decade, a limited number of hot-cell examinations revealed the presence of missing pellet surface (MPS) defects in which some portion of the pellet volume had been removed during the manufacturing process [6,9]. Under normal operating conditions, the pellet-cladding gap will close, except in the location of the MPS defect. Due to a missing region of the pellet the cladding lacks the proper support and produces a local stress concentration localized in the cladding due to the bending moment when the fuel experiences a transient over its conditioned power level [9].

In both cases, it is believed that iodine from the pellet interior is released along the radial cracks in the pellet and collects at sites on the cladding inner surface in the vicinity of the pellet crack opening or the exposed cladding surface adjacent to an MPS defect. The combination of high localized cladding stress and aggressive chemical attack causes a crack to nucleate on the cladding inner surface, which has the potential to propagate through the cladding, depending on the duration of the stress and the claddings material characteristics.

As noted previously, the complexities of fuel rod operation, material performance, and fuel rod design characteristics, drive the need for an integral fuel performance and analysis code to simulate the multiple interacting processes that impact the mechanisms of PCI failure in UO_2-Zircaloy fuel rods. The multi-physics, multi-dimensional characteristics of the PCI failure mechanism makes it an ideal choice as a focus for advanced modeling and simulation. The Bison fuel performance code is being developed as a tool for calculating the fuel thermo-mechanical behavior during normal operation and operational transients. Such a capability can then be used to evaluate the PCI failure potential under a variety of operating conditions and fuel rod designs.

1.2 Role of Fuel Behavior Modeling in PCI

Fuel behavior modeling has been an integral part of the design, licensing, and utilization of nuclear fuel since the inception of nuclear reactors. In the beginning, simplified 1-D axisymmetric codes using analytical thermal and empirical mechanical solutions were used to ensure that fuel designs satisfied the safety requirements of maximum fuel centerline temperatures and cladding stresses, with many methods not considering the need for the coupled thermo-mechanical nature of fuel behavior. However, in the early 1970's, application of detailed material behavior models of fuel rods arose out of the need to better understand the role of fuel operating histories on PCI [1]. This included improved treatment of the mechanical behavior of the fuel and acknowledgement that local effects associated with pellet cracking and pellet-cladding gap closure were extremely important phenomena in fuel performance behavior [11-13]. The primary purpose of fuel behavior modeling is to illuminate the inner workings of the pellet and cladding states during steady state and transient conditions. The insights gained from fuel behavior modeling assists in understanding the experimental fuel rod data and observations

obtained from integral fuel rod experiments or post-irradiation examinations of fuel rods from commercial reactors.

As discussed in more detail below, fuel performance and behavior modeling has evolved from simplified 1-D axisymmetric codes using analytical solutions and empirical models to more advanced multi-dimensional geometric representations that solve the coupled thermal, chemical, and mechanical system of equations [10]. These codes are built on a system of material models that describe the important thermal, mechanical, and chemical properties and constitutive relationships as functions of temperature, chemistry, burnup, fission density, fast flux, fast fluence, and may other state variables. The non-linear behavior resulting from the interaction dependencies between these properties require key assumptions concerning material dependencies, numerical, and geometric representation to satisfy runtime, numerical convergence, and assumption limitations. These difficulties gave rise to simplifications in the fuel rod models to de-emphasize one phenomenon over others, depending on the priorities of the code developer or code purpose. Consequently, fuel performance codes require extensive verification, calibration, and validation exercises to demonstrate the ability of the codes to accurately represent fuel behavior.

The traditional 1 or 1.5-D approaches to model fuel behavior utilize a column of fuel represented by stacked cylindrical slices surrounded by a concentric cladding tube, as shown in Figure 1-4 (a). Each fuel slice is represented by a set of constant volume or constant radial width concentric rings or annuli. The heat conduction equation is solved by either an analytical solution or finite difference calculation, and the local temperature is usually determined at the surface of the rings. Burnup and fission gas behavior is calculated for each ring, and an average value is determined for each slice. In a 2-D finite element analysis (FEA) approach, as shown in Figure 1-4 (b), the fuel and cladding are modeled as elements, with properties evaluated at several integration or quadrature points within each element. Both the 1-D and 2-D models assume a continuum or smeared geometry, with axi-symmetry, and as such, the analyses fail to capture some important 3-D effects, such as pellet hour glassing, MPS, pellet cracking and re-location as a result of cycles of expansion and contraction, or eccentric pellet distribution. To analyze pellet geometrical effects or anomalies, one must apply geometric enhancement factors, or use external codes, e.g., ABAQUS or ANSYS, which require transfer of output from the fuel analysis code to the FEA code.

As shown in Figure 1-4 (c), the 3-D FEA approach extends the elements into full geometric representation and typically uses many more integration/quadrature points. This provides the ability to capture key local geometric effects within the same fuel performance analysis, without the need to transfer data to a different code system.

Two-dimensional FEA has also been extended to an R-θ geometry, as shown in Figure 1-5. The Falcon fuel performance code used such an R-θ geometry to capture localized stress distributions as well as temperature concentrations due to geometric non-uniformities. These plane geometry representations are idealized, with infinitely long non-uniformities. However, this approach has been shown to work well in understanding the impact of such geometric effects [17]. The R-θ models shown in Figure 1-5 include representations of a pellet crack or a MPS that can lead to local cladding stress concentrations. For large MPS defects, the wedge must be increased in size up to 90° in order to insure better symmetry representation. The analysis requires input developed from the output of the local power history, rod internal pressure history, and local fuel and cladding properties from the R-Z calculation

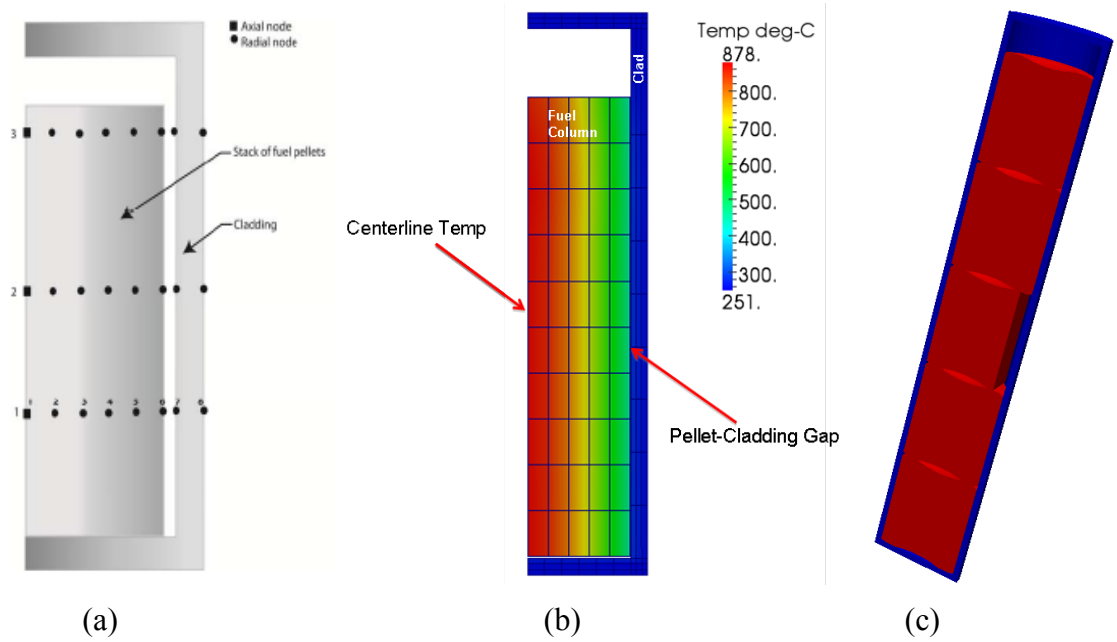

Figure 1-4. 1/1.5D-2D R-Z (a) 1/1.5-D Geometric Representation, (b) Falcon or Bison- 2-D R-Z Fuel Rod Representation, and (c) 3-D Bison 5-Pellet Model Containing a MPS and the Cladding.

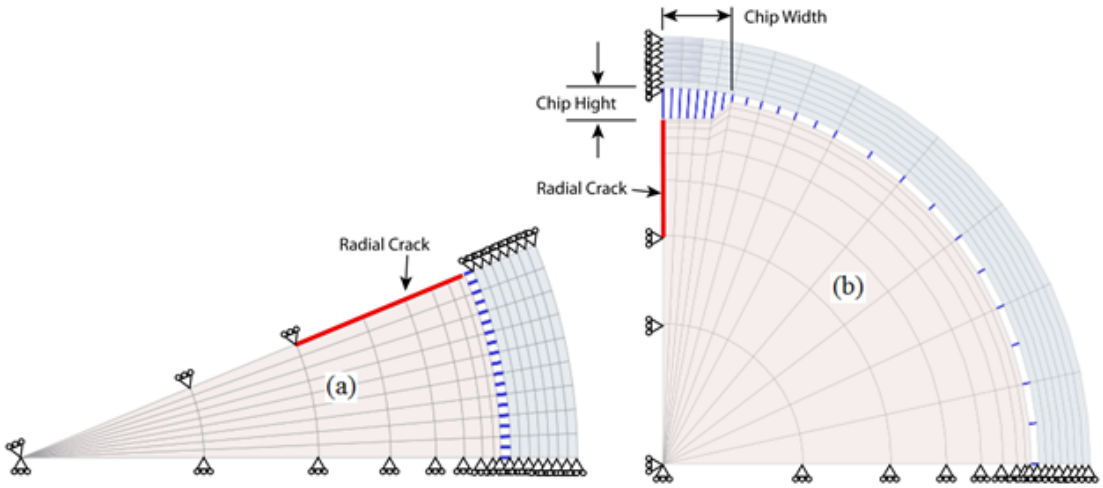

Figure 1-5. 2-D R-θ (a) Model of a Pellet Containing a Radial Crack and Model of a Pellet Containing a MPS as well as a Radial Crack, as reproduced from Ref. [17].

Among the most important physical phenomena in LWR fuel behavior are pellet cracking and re-location. Re-location is the outward movement, extending beyond normal pellet thermal expansion, of the fuel in response to pellet cracks and fragmentation from radial thermal stress gradients, and as such, causes a reduction in the pellet-cladding gap. For fresh fuel, this is not too significant with respect to pellet-cladding mechanical interaction (PCMI), however, it does affect PCMI during subsequent power ramps, particular when there is a power increase well beyond the level consisting of a conditioning fuel state. Pellet cracking also affects the effective compliance of the fuel pellet when the pellet thermally expands and contacts the cladding.

Transitioning from either a 1-D, or 2-D fuel rod modeling to a 3-D geometric representation will require increased physical representation of the cracked pellet behavior. As a result, a mechanistic model is currently being developed within Bison to capture the effects of pellet cracking and relocation on PCMI. Such a model must include mechanisms, such as pellet characteristics and microstructure on fracture strength, cracked-body behavior, and stochastic effects of fuel rod fabrication, handling and other body forces.

Traditionally, 1-D/1.5-D analysis methods typically use an empirically derived cladding stress threshold to establish a failure criterion or cumulative damage index (CDI). This failure criterion is then used to assess the potential for PCI failure to occur. Codes such as RODEX, XEDOR, and CYRANO3 have used PCI ramp test data to establish this stress threshold for use in calculating the performance of power reactor fuel [14-16]. In this proposal, that approach will be followed and extended using a combination of 2-D and 3-D modeling of the test reactor ramp test data.

For the combined 2-D R-Z/R-θ PCI analysis methodology used in Falcon, a three step process has previously been developed [17]. The first steps consist of a steady-state R-Z analysis of the base irradiation, followed by a power ramp or transient R-Z analysis. Finally, a local R-θ PCI analysis is conducted to calculate the maximum cladding hoops stress [17,18]. The first step evaluates the detailed fuel rod power history to establish the local conditions. The conclusion of this analysis provides the initial conditions for the power ramp or transient analysis. The second step of the combined 2-D approach includes a full-length, R-Z analysis of the power maneuver. Using the results from this analysis, the axial location of the maximum average cladding hoop stress is identified. This information along with other fuel rod data such as internal pressure history is used in the third and final step of the analysis, which is the R-θ analysis. This approach has been applied to experimental data developed in power ramp test programs, including OVERRAMP, SUPERRAMP, and TRANSRAMP [19], in order to validate the method and calibrate a cladding damage model and failure threshold, and to commercial power plants for PCI margin assessments [17,18].

Of particular interest is the impact of defective fuel pellets that contain missing pellet surface (MPS) defects, since such defects have been identified as a root cause of many recent occurrences of PCI fuel failures, including at the Braidwood and Byron reactors. From 2000 to 2005, there were a small number of PWR fuel rod failures, most of which coincided with the startup from refueling outages [20,21], and one case of a failure during a mid-cycle power maneuver [20]. During the same period, a small number of BWR failures were reported [8] which occurred during normal control blade adjustments. An initial analysis revealed that predicted stresses, assuming defect free pellets, were below levels at which classical PCI would be expected. Even when MPS defects were introduced into a R-θ model, the predicted stresses

remained relatively low with respect to PCI [20]. It was subsequently determined that the MPS defects were well beyond the established manufacturing limits as shown in Figure 6 [8,21].

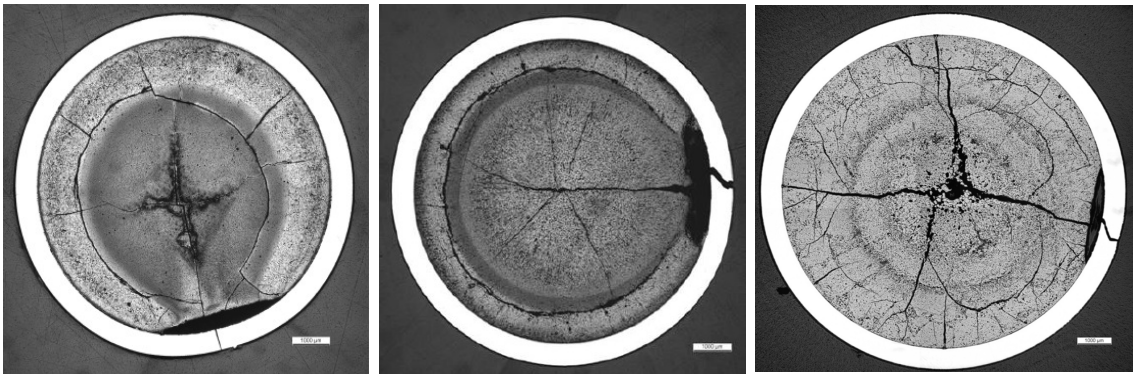

Figure 1-6. Photographs of MPS-related PCI failures in PWR fuel (left and center) and BWR fuel (right), as reproduced from Ref [22,9].

Previous efforts to evaluate the impact of MPS defects on cladding failure have used traditional 1-D/2-D fuel performance codes coupled with 3-D form factors derived from general purpose finite element codes [17]. The goal of this dissertation using the Bison code is to contribute to the development of a high fidelity 3-D thermal and mechanical representation of the pellet and cladding behavior coupled with a more physics-based representation of the underlying mechanisms that lead to cladding failure. These mechanisms include the role of fission product transport, chemical reactions with the cladding, and irradiation effects on the mechanical behavior of the fuel pellet and cladding materials.

1.3 Methodology for Evaluating PCI

The motivation for moving to higher fidelity, 3-D, models for PCI calculations is to reliably calculate the PCI failure potential for specific core loading patterns and operating strategies in use in LWRs, define the impact of component fabrication defects and material properties and characteristics on PCI failure potential, and highlight the role of plant operating strategy and fuel design on the potential for PCI failure. To fulfill these objectives requires the ability to consider the impact of core loading patterns on fuel operation and fuel performance, that incorporates the role of plant operational strategies on fuel performance, and considers the evolution in irradiated material behavior during fuel history. By developing and using advanced modeling and simulation capabilities that employ coupled multi-physics, multi-dimensional, and mechanistic modeling, should assist in reducing the uncertainties in the current models used to perform PCI failure potential assessments.

The approach to address the improve upon current geometric models and attempt to predict PCI failure is challenging. The process involves developing a methodology that can assess the potential for cladding failure contributed to PCI processes for a given core loading pattern as well as a planned operating strategy. The major elements of this methodology involves a best-estimate fuel performance modeling capability, an ability to quantitatively measure failure potential in a fuel rod due to PCI, a process to evaluate the local power changes for different operating conditions, and an approach to account for uncertainties in fuel rod quality, and local power. Researchers in the nuclear power industry have been working on various aspects of this methodology for more than 30 years, including fuel performance modeling of PCI, assessment of performance indicators of cladding failure, such as cladding stress or cumulative damage models, and evaluation of separate effects tests designed to replicate PCI failure.

Until the mid-2000's, the approach to manage cladding failure by PCI involved operating guidelines or rule-base algorithms that restricted the buildup of high cladding stresses. These operating restrictions were based on operation experiences, power ramp test programs using test reactors, and some analytical evaluations [22-24]. These approaches however were incapable of accounting for conditions that strayed from the norm, such as MPS, or the evolution of operating strategies to high burnup accumulation cycles, new fuel designs, or fuel rod materials.

In 2010, EPRI released a PCI Guidelines document that utility engineers can use to asses the PCI failure potential for certain fuel designs, core loadings, and operating strategies [25]. The methodology outlined in the EPRI Guidelines is based on Falcon fuel performance calculations embedded within a systematic process that evaluated real-life reactor operations to quantify the PCI failure potential [18]. These guidelines provide a PCI risk assessment procedure that could be used to evaluate reactor core designs and operating strategies during the core reload design process. Similarly, in an effort to improve fuel reliability for boiling water reactors (BWR), AREVA has recently implemented a reduced-order fuel rod stress calculation model, called XEDOR, within their core-wide power monitoring system to gauge the cladding stress and potential for PCI failure [26,27]. This system allows a reactor operator to check, in real-time, the evolution of the cladding stress during a power maneuver or off-line evaluate different power ramp rate scenarios prior to implementing them in the control room.

At the heart of these PCI failure evaluation methodologies is the calculation of a local performance indicator that provides a measure of cladding failure by the SCC process. The majority of the fuel performance codes have selected cladding stress as this performance indicator. As mentioned above however, stress is only one component to the failure process and as shown in Figure 1-7, does not necessarily provide a best-estimate prediction of the potential for cladding failure. Figure 1-7, shows the peak hoop stresses calculated by either XEDOR, as shown in Figure 1-7(a), or Falcon, as shown in Figure 1-7(b) for failed and non-failed rods from PCI ramp test programs. This illustrates that cladding hoop stress levels alone do not allow the necessary differentiation between failed and non-failed rods to provide a failure prediction. As a consequence, methodologies based on a stress-based performance indicator generally use conservative threshold values to account for these inaccuracies.

In addition to the computation of the stress concentrations on the clad inner surface, a second method calculates a cladding cumulative damage index (CDI) value for each element in the cladding as an indicator of failure potential. The CDI is calculated using a cumulative damage model based on a time-to-failure experimental data. The theoretical basis for the use of this model is discussed below. SCC data for Zr-2 and Zr-4 cladding have been accumulated over

the past thirty years. With more recent data becoming available, increased utilization of an SCC-based failure analysis methodology is becoming more justifiable.

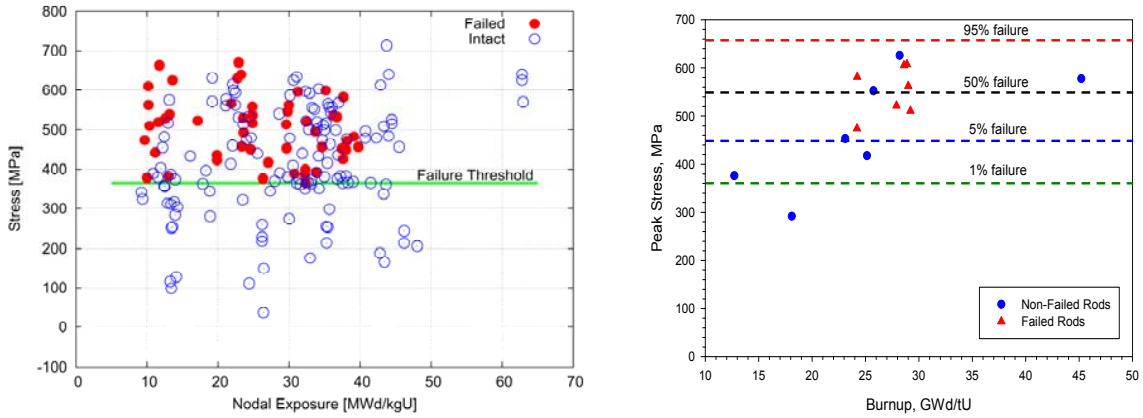

(a) (b)

Figure 1-7. Examples of Cladding Stress as Calculated Performance Indicator in (a) XEDOR and (b) Falcon, as reproduced from Ref. [27,17]

The phenomenon of PCI is a highly stochastic problem relying on a significant number of conditions, e.g irradiation time, corrosion, power maneuvers, and material properties, for rod failure to occur. The accumulation of these parameters leads to prediction of failure to be a stochastic problem. Cladding failure by means of SCC can be broken down into two fundamental stages. The first stage is a nucleation stage. This stage accounts for the time it takes a crack to nucleate on the inner surface of the cladding from a local stress concentration or adjacent to a surface defect in the pellet. The second stage is a propagation stage. Time evolution of the first stage can take anywhere from a few seconds to a few hours, depending on cladding temperatures, these fission products responsible for corrosive effects, e.g. iodine, cesium, or cadmium, and the local stress levels above the SCC threshold. When the crack switches from the nucleation stage to the propagation stage, the crack will begin to extend in a stable fashion until the crack reaches a critical size. Once the crack reaches its critical size the cladding will immediately fail, e.g. a through wall crack, releasing fission products into the coolant. The CDI model treats both stages of the SCC mechanism as a cumulative damage process, in which the accumulation of damage is linear with time, such that a damage fraction D can be defined as follows[17]:

$$\boldsymbol{D = \int dt / t_f} \qquad (1\text{-}1)$$

where D is the damage fraction, t is time, and t_f is the time-to-failure in a material while under SCC conditions, defined as follows [17]:

$$\boldsymbol{t_f = f(\sigma, \sigma_y, \sigma_{ref}, B, T)} \quad (1\text{-}2)$$

The independent variables from equation 1-2 are described as:

- $\boldsymbol{\sigma}$ = Cladding hoop stress (MPa)
- $\boldsymbol{\sigma_y}$ = Cladding yield stress (MPa)
- $\boldsymbol{\sigma_{ref}}$ = Burnup dependent function for cladding material (MPa)
- B = Burnup (MWd/TU)
- T = Temperature (K)

In equation 1-2, t_f is the time it takes the cladding to fail in a SCC out of pile test, for a material that has accumulated a burnup level of B, in which the applied stress σ and the temperature T of the material are held constant. Equation (1-1) applies to a single continuous power event during a power cycle, such as a transient followed by a period of constant power, and is not continuously calculated from power ramp to a new power ramp. The damage fraction D is calculated incrementally as [17]:

$$\Delta D = \frac{\Delta t}{t_f(\sigma, T, \phi)} \quad (1\text{-}3)$$

where, t_f is the time to failure for a given stress (σ), temperature (T), and given fast neutron fluence (ϕ), and material conditions in the time incrament Δt. Experience with the SCC damage parameter defined above shows logarithmic behavior with stress and lends itself to a probabilistic interpretation as follows: $D = 1$ implies 50% probability of failure, with <5% and >95% failure probabilities assigned to $D = 0.1$ and $D = 10$, respectively [17].

Application of the above model to fuel rods requires special interpretation of the laboratory tests with respect to power transients, where the cladding stress can drop below the SCC threshold due to a reduction in power or relaxation of the hoop stresses when the power is held constant. However, Equation (1-3) does not fully account for the fission product environment inside the fuel rod as well as the out of pile test environment. These are important factors to consider and do play a role in SCC lead failures. To account for these, a deterministic form of Equation (1-4) is applied as follows [17]:

$$D = \sum_{i=1}^{n} \frac{\Delta t_i}{\beta t_{fi}} \quad (1\text{-}4)$$

where β is a single-valued parameter determined by benchmarking the model against SCC power ramp test data. This term accounts for the translation of the out-of-pile time-to-failure measurements of cladding tubes to the in-pile behavior of a fuel rod at the time of failure. This approach then provides a definable, probabilistic relationship between the value of D, the computed damage fraction, and fuel rod failure probability calibrated to actual power ramp test data.

A third way to analyze cladding failure probability is to calculate clad strain energy density (SED) and use it as a critical parameter for failure. The strain energy density in a body under a combination of elastic and plastic loading can be approximated by use of the equation:

$$U = \frac{\sigma_y^2}{2E} + \int_0^{\epsilon_{ij}} \sigma_{ij} d\epsilon_{ij} \qquad (1\text{-}5)$$

The first term accounts for the potential energy from elastic deformation, where E is the Zircaloy clad elastic modulus, and the second term accounts for the potential energy contributed to plastic deformation. Failure predictions are obtained by comparing the calculated SED under transient conditions with a threshold value, which is experimentally determined from mechanical tests on oxidized and irradiated clad materials.

Rashid and co-workers have proposed a correlation for this failure threshold, based on data from clad burst tests and uniaxial tensile tests in both the axial and hoop directions [28]. There critical strain energy density (CSED) is developed from material property tests as a function of material conditions, including temperature, fast fluence, outer surface corrosion, hydrogen concentration, and hydride morphology. Rashid's equation to calculate CSED is [28]:

$$U = \frac{\sigma_y^2}{2E} + \int_{\epsilon_e}^{\epsilon_e + \epsilon_{te}} K\varepsilon^n \left(\frac{\dot{\epsilon}}{\dot{\epsilon}_o}\right) d\epsilon \qquad (1\text{-}6)$$

where σ is the true stress, ε is the true strain, $\dot{\epsilon}$ is the strain rate, and K, n, and m are material properties, for Zircaloy, from MATPRO. Similar to equation 1-5, the first term is accounts or the elastic energy and the second term accounts for the plastic strain energy.

A key challenge will be to investigate and incorporate advanced modeling and analysis capabilities to improve the calculation of the PCI failure potential. This will require improvements in the material property and behavior models used in the fuel performance calculations, higher fidelity geometric modeling to account for material discontinuities such as pellet cracks or pellet defects, and a performance indicator that better represents the physics of SCC failure. Finally, the capability to calculate the potential for cladding failure must be coupled into the calculation of the fission density, fast neutron flux, and coolant channel heat transfer conditions throughout the reactor. This requires the ability to evaluate all the fuel rods in the code during operation.

1.4 Bison Overview

Bison is built upon the Multi-physics Object-Oriented Simulation Environment (MOOSE) [30] developed at Idaho National Laboratory (INL). MOOSE is a massively parallel finite element computational system that uses a Jacobian-free, Newton-Krylov (JFNK) method to solve coupled systems of non-linear partial differential equations. In addition, the MOOSE framework provides the ability to effectively use massively parallel computational capabilities needed to create high fidelity 3-D models of a fuel rod, as well as full-length R-Z rods, and R-Theta geometric representation.

Bison builds upon the underlying architecture of MOOSE, developed at INL [30]. This architecture includes the ability to incorporate, or develop, material properties libraries and fuel behavior models for UO_2 fuel and zirconium alloy cladding commonly used in PWRs. A major focus of the effort on modeling nuclear fuel performance, beyond the Bison development, has been to develop physics-based material models for ceramic UO_2 fuels and zirconium alloys [31]. These models consist of irradiation induced clad creep and growth, clad corrosion, the hydrogen pickup and hydride precipitation in the clad, and the release and transport of fission gas. However, since Bison is being developed simultaneously with the effort to develop improved mechanistic behavior models that are not yet ready for implementation, empirical models from the open literature and selected EPRI/Falcon models have been incorporated to date. This allows for testing of the numerical framework of Bison, as well as to identify material models that require further development.

1.5 Requirements for Bison-Analysis

Simulation of the processes leading to cladding failure by PCI requires a modeling approach that considers the coupled thermo-mechanical-chemical behavior on-going in a fuel rod during the operating life-time. Bison is being designed to model the behavior of a single fuel rod to establish the initial conditions of temperature, pellet and cladding deformations, and fission products prior to a power maneuver and then the evolution of these conditions during an increase in power to evaluate the potential for PCI induced failure. To accomplish these objectives, requires using a computational framework that has the versatility to model the local geometric conditions present in a fuel rod, the ability to couple the multiple physical processes that occur within a fuel rod, the capabilities to consider the multiple varieties of material property and behavior models needed to simulate the evolving conditions within the fuel rod, and the robust numerical solution to which a through time evolution can be conducted throughout the operating history in a computationally efficient manner. Previous efforts to construct fuel behavior modeling codes have varied from analytically-based solutions for simplified sets of equations to multi-dimensional finite element formulations. Each type of approach has various advantages and disadvantages. However, most of these approaches have proved useful in simulating fuel rod behavior during operation.

A standard LWR fuel rod contains a column of ~360 UO_2-based ceramic pellets (~8.1 mm outer diameter) that are encased in zirconium alloy cladding tubes (~9.5 mm outer diameter). Standard PWR cladding material, Zircaloy-4, has generally been replaced by Zr-Nb-

Fe-O (M5^{TM}) and Zr-Nb-Sn-Fe-O alloys (ZIRLO^{TM}) for fuel in operation today. Some fuel rod designs incorporate burnable poisons such as gadolinia (Gd_2O_3) or zirconium diboride (ZrB_2), which are used for power shaping or to control the reactivity in the core and fuel assembly. Initially, the Bison code will focus on UO_2 fuel and Zircaloy-4 cladding using standard PWR fuel rod designs. Eventually, the fuel material properties models must be expanded to include UO_2-Gd_2O_3 pellets, and UO_2 pellets coated with ZrB_2. Similarly, cladding models must eventually include more advanced zirconium alloys such as ZIRLO^{TM} and M5^{TM}.

In order to accurately simulate fuel rod behavior, including PCI, Bison- must model the pellet and cladding microstructure evolution over one or more cycles, where the cycles typically last 480 to 530 effective full power days (EFPDs) for 18-month cycles or 640 to 700 EFPD for 24-month cycles. The length of time depends on the plant operating strategy including practices like coast down, planned maintenance, and unplanned outages. During these operations power changes can occur every few weeks during normal operation. Furthermore, Bison must also capture the thermo-mechanical and thermo-chemical responses that occur over several hours during a startup or a return to full power following a period of reduced power operation.

The fundamentals of calculating the temperature distribution and stress/strain behavior of nuclear fuel rods has been described in many good papers in the literature [31,32]. This includes numerical solutions to the heat conduction and equilibrium statics equations with temperature and microstructure dependent properties. As such, the set of thermal and mechanical field equations that form the basis for Bison will not be discussed in detail. The focus will be more on incorporating the material and behavior models required to describe the response of the fuel within the operating environment. Building on this background of experience, the mechanisms important to pellet-cladding interaction that Bison will model include the following;

- Pellet
  - Thermal Expansion (function of conductivity and expansion coefficients)
  - Crack formation and fragment relocation
  - Thermal and Irradiation-Induced Densification
  - Swelling (Solid and Gaseous)
  - Interfacial contact and friction/bonding between pellet and cladding
  - Fabrication Imperfections (e.g., MPS)
  - Fission gas/product release/decay
- Cladding
  - Creepdown (irradiation and thermal creep)
  - Stress relaxation (thermal creep)
  - Chemical/metallurgical reactions leading to SCC of zirconium alloys
  - Outer Surface Reactions and Corrosion Layer Formation

Many of these phenomena depend on the ever changing irradiation conditions such as burnup, fast neutron fluence, fast neutron flux, local power and temperature conditions, and material microstructure state resulting from fission damage, neutron damage or chemical reactions. These dependencies must be properly accounted for and incorporated into the thermal and mechanical solutions to capture their feedback on overall fuel rod response.

Chapter 2: Validation and Benchmark Evaluation

2.1 Approach to Benchmark and Validation

The benchmark and validation approach for Bison consists of four main elements: First, to verify the temperature modeling capabilities; Second, to verify the mechanical modeling capabilities; Third, to verify fission gas release modeling capabilities; and Fourth, to verify the PCI failure modeling capabilities. As the fuel and cladding temperatures strongly impact most of the material behavior that control the performance of the fuel (e.g. pellet thermal expansion, fission product release, and cladding creep), the initial Bison benchmark activities focused on the temperature modeling, mechanical deformation, and fission gas release capabilities of the code. The primary objectives of the benchmark and validation activity are to demonstrate that the thermal solution and the mechanical solution are appropriately coupled; the material models that control thermal conductance are functioning as expected; the pellet-cladding mechanical interaction and mechanical constitutive model are operational; and that the integrated fuel rod response to irradiation is being calculated appropriately, as reflected in the fission gas release calculation.

Bison has been developed to support both axi-symmetric 2-D R-Z and detailed 3-D representations of a single fuel rod. The ability to perform both types of geometric representation provides for flexibility in the benchmark and validation process as detailed 3-D information is not readily available for most fuel rod irradiation tests. In addition, detailed 3-D problems require greater computational and data management resources, and considerably longer analysis time. As a result, the initial development of Bison has focused on the 2D R-Z axisymmetric models in order to be able to compare directly with similar models, available data, and the assessment cases run with Falcon. In the future, several of these 2-D cases will be developed into 3-D cases, and the results compared to ensure that the results obtained with the 3-D representation are consistent with the results obtained in 2-D.

Table 2-1 lists the initial benchmark validation cases selected to test the capabilities of Bison. These cases were chosen from the database of irradiated fuel rod cases available from the Falcon code [33]. This database includes more than 300 fuel rods irradiated in both test and commercial reactors to burnup levels near 80 GWd/tU. The thirty fuel rod cases listed in Table 1 were chosen to assess the thermal, mechanical, and fission gas release modeling capabilities of Bison and represent a range of irradiation tests designed to evaluate increasingly more complex operating conditions within the fuel rod.

The test rods listed in Table 2-1 were selected specifically to assess specific models in Bison over a range of fuel design parameters, linear power, fast fluence, and fuel burnup. For many of the rods selected, in-pile measurements of temperature and/or cladding deformations are available to compare directly with the calculate values. This type of data is invaluable to assess the capabilities of a fuel performance code because of the difficulties in characterizing the state of a fuel rod in operating reactors.

Table 2-1. Bison list of benchmark cases

Case	Ave. Burnup Fast Fluence	Description
IFA 504 Rod 2	~ 0.1 GWd/tU	He fill gas evaluated during startup, available up to ~50 GWd/tU
IFA 505.5 Rod 1	~ 40 GWd/tU	Various enrichments, fill gases, and gaps
IFA 509.1 Rod 1	~ 14 GWd/tU	10% enrichment, He-filled
IFA 513, Rod 2		He 2 bar
IFA 515.10 Rod A1	~ 76 GWd/tU	He-filled, UO_2 50 mm gap
IFA 515.10 Rod A2	~ 84 GWd/tU	He-filled, UO_2-8% Gd_2O_3 50 mm gap
IFA 562.1 rod 2	11.9 GWd/tU	Xe fill gas 1 bar, fuel roughness coeff, and gap size
IFA 562.1 rod 5	12.2 GWd/tU	He fill gas 1 bar, fuel roughness coeff, and gap size
IFA 562.1 rod 7	10.3 GWd/tU	Xe fill gas 1 bar, fuel roughness coeff, and gap size
IFA 562.1 rod 11	10.2 GWd/tU	He fill gas 1 bar, fuel roughness coeff, and gap size
IFA 562.2 rod 15	51 GWd/tU	He fill gas pressurized to 10 bar
IFA 562.2 rod 16	56 GWd/tU	He fill gas pressurized to 10 bar
IFA 585.4 Upper	1.2×10^{22} n/cm^2	Clad creep Zy-4 pre-irradiated
IFA 585.4 Lower	1.2×10^{22} n/cm^2	Clad creep Zy-4 pre-irradiated
Rod AN2	42 GWd/tU	PWR 14x14 UO_2 rod
Rod AN8	42 GWd/tU	PWR 14x14 UO_2 rod
Rod AN11	41 GWd/tU	PWR 14x14 UO_2 rod
Rod PK2-1	45.2 GWd/tU	PWR 14x14 UO_2 rod
Rod PK2-3	44.6 GWd/tU	PWR 14x14 UO_2 rod
Rod PK2-S	43.4 GWd/tU	PWR 14x14 UO_2 rod

All of these test rods were part of irradiation programs designed to study some parameter or phenomena of fuel performance, such as gap conductance, pellet-cladding mechanical interaction, irradiation behavior of material properties or fission gas release. For example, the cases include test rods that were connected to flowing internal gas systems to allow for specific control of the pellet-cladding gap heat transfer conditions. As a result, the benchmark and validation activities can focus on specific capabilities in Bison and potentially isolate model effects to gain better insights into areas for further improvement. However, it should be noted that these data have limitations because of the following; 1) most of these irradiation programs were performed in the 1970's and 1980's using fuel designs that differ significantly from current fuel; 2) these irradiation programs were conceived and executed to support modeling fuel performance using simplified geometric representation (1/1.5 D) and as such limit 3-D effects; and 3) the quality of the power history and measured data may be insufficient for the detailed modeling aspired to with Bison. Acknowledging these limitations is important in the Bison benchmark and validation effort, as it influences assumptions and approaches used to represent the test rod geometry and irradiation conditions. But even with these drawbacks, the available data from these tests are critical to the assessment of Bison's fuel modeling capabilities.

2.2 Benchmark and Validation Results

2.2.A Thermal Benchmark Analysis

Table 2-2 summarizes the experiments that were selected for benchmarking comparisons between Bison and Falcon. In these simulations and comparisons, the experimental data provides the fuel centerline temperature measured by a thermal couple inserted into annular fuel pellets, which were performed in the Halden IFA experiments. In this chapter, a select sub-set of detailed inter-comparisons associated with IFA-505.5 rod 1 and IFA-515 rod A1, as well as a summary of the agreement for the entire set of fuel centerline temperature predictions.

The IFA 505 experiment was designed to measure fuel centerline temperatures with small or closed xenon filled gaps [7,8]. The experiment used a wide range of fuel rod specifications, such as different plenum fill gas and gap sizes. The 505.5 Rod 1 that we have focused on modeling was 0.14 meters in length and consisted of 11 pellets, in which the top six pellets were annular to accommodate the insertion of a thermocouple. The rod had an initial diametral fuel-clad gap of 100 micrometers, and was pressurized to 1 bar with helium fill gas. The rod was then irradiated in the Halden reactor to a burnup of approximately 35 MWd/kgUO_2, during which many linear power maneuvers were performed that raised or lowered the rod average power. It is important to note that Falcon does not have the capability to model the thermal couple region and assumes solid pellet geometries. Bison does have the ability to model the thermal couple region using annular pellets.

Table 2-2. Description of Halden IFA test rods selected for thermal benchmark studies and key characteristics of each rod.

Thermal Benchmark IFAs		
Test Rods	**Burnup ($MWd/kgUO_2$)**	**Key Characteristics**
IFA 430 rod 2	~2.3	He (Ar, Xe) fill gas. BOL gap hydraulic diameter measurements, and temperature, 10 bar He, 230 μm diametral gap.
IFA 504 rod 2	~0.086	He (Ar, Xe) fill gas. BOL gap hydraulic diameter measurements, and temperature, 2 bar He, 200 μm diametral gap.
IFA 505.5 rod 1	~34	He fill gas pressurized to one bar
IFA 515 rod A1	~76	He fill gas pressurized to 10 bar
IFA 562.1 rod 5	~10.75	He fill gas 1 bar, fuel roughness coeff, and gap size
IFA 562.1 rod 11	~10.75	He fill gas 1 bar, fuel roughness coeff, and gap size
IFA 562.2 rod 15	~51	He fill gas 10 bar ran to high burnup
IFA 562.2 rod 16	~56	He fill gas 10 bar ran to high burnup

Figure 2-1 shows the fuel centerline temperatures measured experimentally (blue), and predicted by Falcon (green) or Bison (red) as a function of burnup. Overall, the Bison predictions are slightly lower than the predictions made by Falcon, and both codes are in generally good agreement with the experimental measurements of fuel temperature evolution with power ramps and burnup. In particular, both models follow the power history throughout the entire irradiation, including the operational maneuvers to increase or decrease the power. The most significant disagreement between the models and experimental results are observed between burnup values of about 5 to 10 $MWd/kgUO_2$, when both Bison and Falcon under predict the centerline temperature, and between about 32 and 35 $MWd/kgUO_2$, when Bison begins to diverge from its general trend. The lower burnup discrepancy may be attributed to the prediction of fuel–clad gap closure, although there is not experimental data to confirm this hypothesis. Bison predicts gap closure at about 14 $MWd/kgUO_2$, and for intermediate burnups between about 15 and 30 $MWd/kgUO_2$, Bison again predicts reasonable agreement with the measured values. With increasing burnup above 30 $MWd/kgUO_2$, the Bison and Falcon fuel centerline predictions diverge from each other, with the Bison predictions on the low side of the experimental data. The cause of the divergence is most likely related to the degradation of gap conductance due to fission gas release.

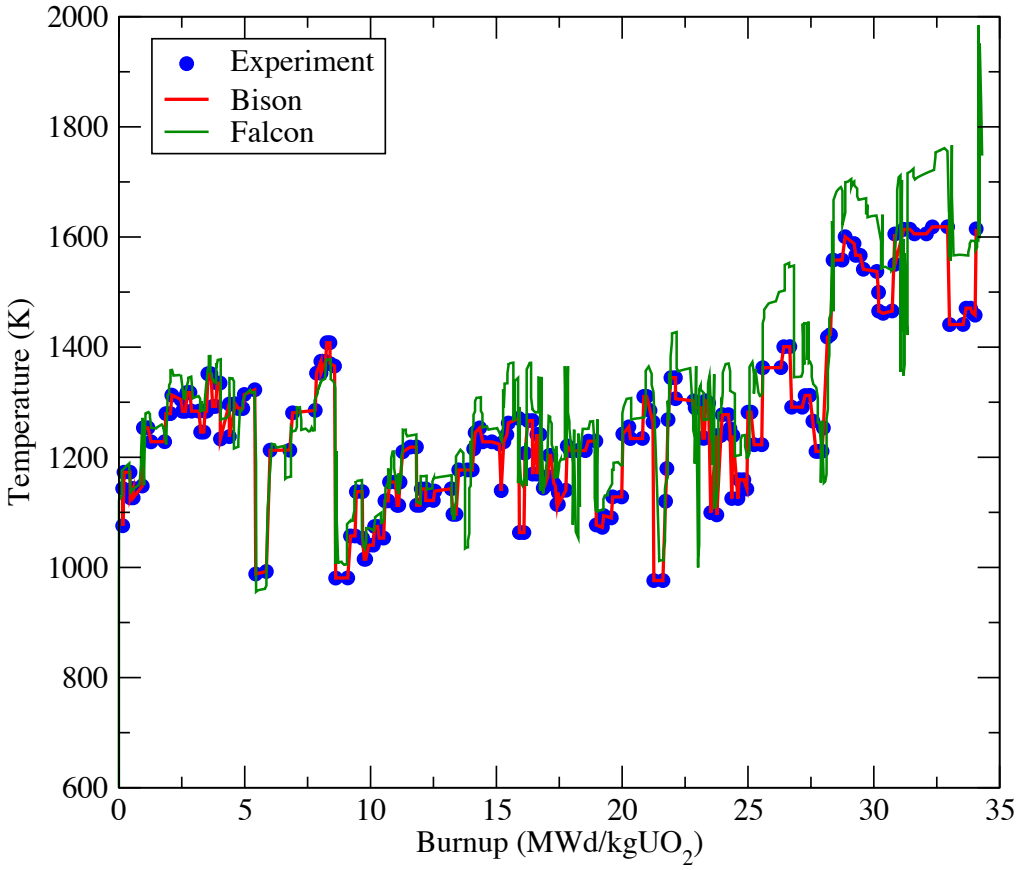

Figure 2-1. Fuel centerline predicted and experimentally measured in IFA 505.1 Rod 1, as a function of burnup. The Bison predictions are shown with a red line, whereas the Falcon predictions are shown with a green line.

Figure 2-2 shows the fission gas release predicted by Bison and Falcon. Falcon predicts ~13% fission gas release during the entire burnup history of this IFA 505.5 Rod 1. However, Bison predicts significantly lower fission gas release, which begins to occur at a burnup of 26 MWd/kgUO_2, as shown in Figure 2-2. It is not unexpected for Falcon to predict higher fission gas release than Bison, seeing as Falcon modeled solid pellets and Bison had taken into account the thermal couple region. Since the initial helium fill gas pressure had a relatively low value of about 1 bar, the release of Xe and Kr fission products into the plenum can significantly reduce the gap thermal conductivity, which we believe explains the lower fuel centerline temperatures predicted by Bison for burnup above 30 MWd/kgUO_2.

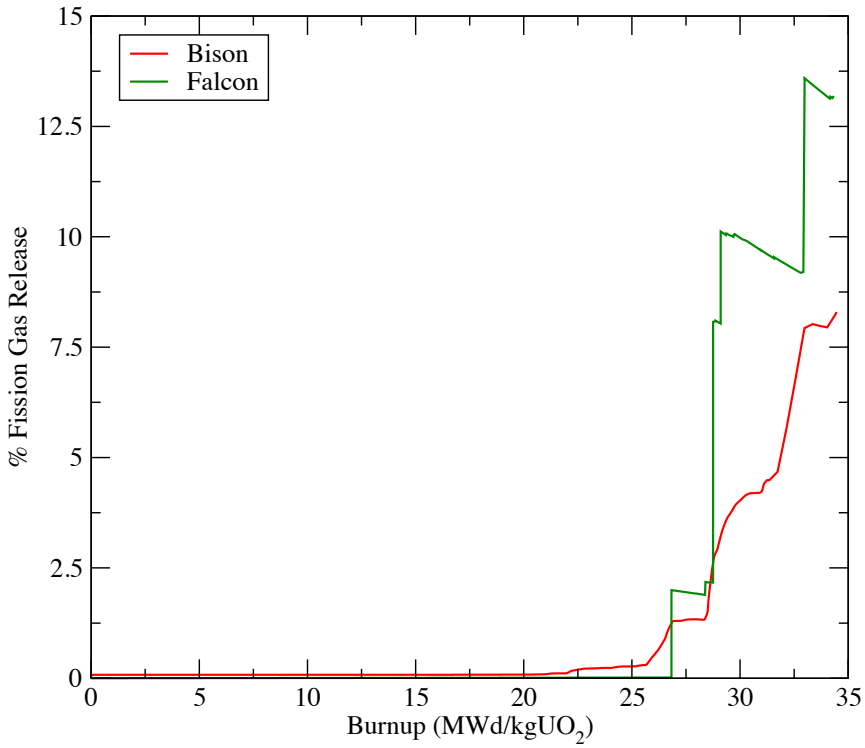

Figure 2-2. Predictions of fission gas release from IFA 505.1 Rod 1 by Bison (red) and Falcon (green), as a function of burnup.

The next benchmark comparison presented here is the IFA 515 experiment, which was selected in order to evaluate the effect of gadolinium on fuel thermal conductivity as a function of burnup. The 515 rods were 0.212 meters in length and modeled with completely annular fuel to account for the inserted thermocouple [34]. Both the A1 and A2 rods were irradiated to a burnup of 76 MWd/kgUO_2. The A2 rod is not shown here, since the appropriate behavioral models for burnable poisons have not yet been incorporated into Bison. The rods were filled with helium fill gas to a pressure of 10 bar.

The purpose of IFA 515 was to evaluate the performance of Bison to predict fuel centerline temperature to high burnup levels. Unlike the IFA 505.5 case that was just presented, IFA 515 extends the burnup to ~76 MWd/kgUO_2. Figure 2-3 shows the measured fuel centerline temperature for IFA 515 Rod A1 (blue), as well as the Falcon (green) and Bison (red) predictions. In general, both code predictions do a reasonable job following the power history evolution of the fuel centerline temperature with burnup, although there are differences between the Falcon and Bison predictions. Falcon generally over-predicts the fuel centerline temperature relative to both the experimental measurements and Bison predictions especially at relatively low burnup values, but the agreement between the two codes improves after gap closure, as shown in Figure 2-4.

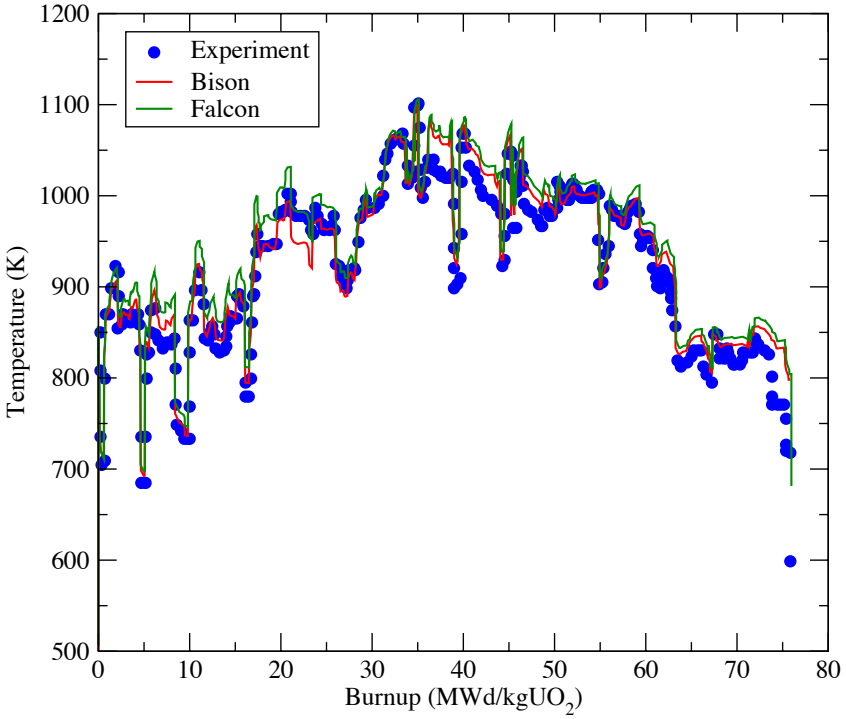

Figure 2-3. Fuel centerline predicted and experimentally measured in IFA 515 Rod A1, as a function of burnup. The Bison predictions are shown with a red line, whereas the Falcon predictions are shown with a green line.

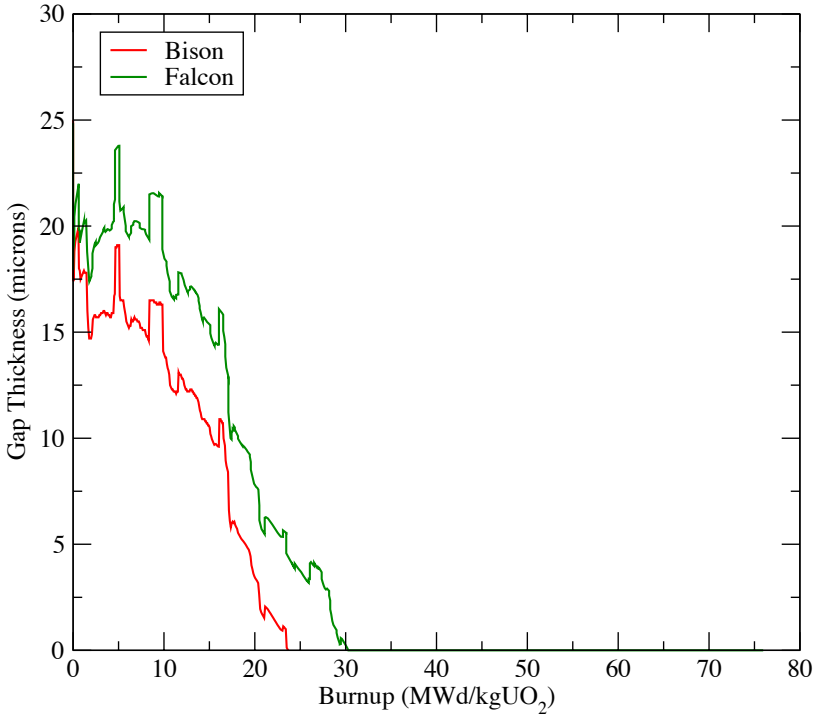

Figure 2-4. Calculated fuel – clad gap thickness for the IFA 515 Rod A1, with the Falcon results shown in green and the Bison results in red.

Figure 2-4 shows the predicted gap thickness. Both Bison and Falcon predict the gap to close between 25 and 30 MWd/kgUO_2. Bison uses a penalty contact algorithm [35]. In Figure 2-4, Bison shows the result of the penalty algorithm. The current penalty value predicts reasonable solutions but does require further investigation and optimization.

As seen in Figure 2-3, Bison appears to predict a better fuel centerline temperature than Falcon, and both codes over predict the measured temperature. There are several key factors which influence the over predictions of fuel centerline temperature, as compared to the experimental measurements. As stated before, both codes predict the fuel-cladding gap to close at slightly different burnup values, and the prediction of gap closure plays an important role in gap conduction as does the amount of fission gas release. In addition, Bison currently lacks the ability to partition the nuclear energy. This partitioning of the fission energy results in about 3±0.5% of the volumetric heat generation being deposited in the cladding, coolant, and core structures. While Falcon has the ability to partition the nuclear thermal energy, this function has been disabled to provide a more systematic comparison to Bison. With the addition of the partitioning of nuclear thermal energy into core structures and coolant, the Falcon and Bison fuel centerline temperatures would decrease, providing a better agreement with the experimental measurements.

Based on the results shown in Figures 2-1, 2-2, and 2-3, as well the other comparisons (listed in Table 2-1) that have been performed but are not shown here, we conclude that Bison is calculating fuel centerline temperature values that are in reasonable agreement with the experiment. Figure 2-5 shows a comparison of the calculated versus measured fuel centerline temperatures from all of the thermal benchmarking Falcon and Bison calculations performed to date. In Figure 5, the circle symbols denote Bison predictions, and the triangles denote Falcon results. As well, two deviation lines of 50 degrees in the positive and negative values are included. Figure 2-5 demonstrates a quite good agreement between the Bison predictions and the measured values, in which the vast majority of the predicted results are within a +- 50- Kelvin window. By comparison, Falcon tends to consistently calculate a higher fuel centerline temperature.

Bison appears to be reliably calculating reasonable fuel centerline temperatures compared to Falcon and the experimental measurements. However, there remain several fuel and materials related models and phenomena that Bison must incorporate. These include correctly accounting for the partitioning of nuclear fission energy and distribution of the volumetric heat generation rate, improvements in the gap closure and gap thermal conductivity models, as well as continued optimization of the penalty model for pellet–clad contact. Furthermore, gap thickness in IFA fuel is primarily driven by fuel thermal expansion, and it seems apparent that the differences between Bison and Falcon at relatively low burnups are associated with predicting gap thickness and fuel – clad gap closure could be related to differences in the models of fuel thermal expansion at temperatures between 300 K- 700 K. This is due to the fact that Bison has implemented a new model for UO_2 thermal expansion, whereas Falcon uses a modification of MATPRO-11 model [36]. Finally, it is also evident, by Bison predicting much lower temperatures, from Figure 2-2 that the fission gas release and swelling model implemented in Bison requires further work, which is also expected to influence the code predictions of clad deformation.

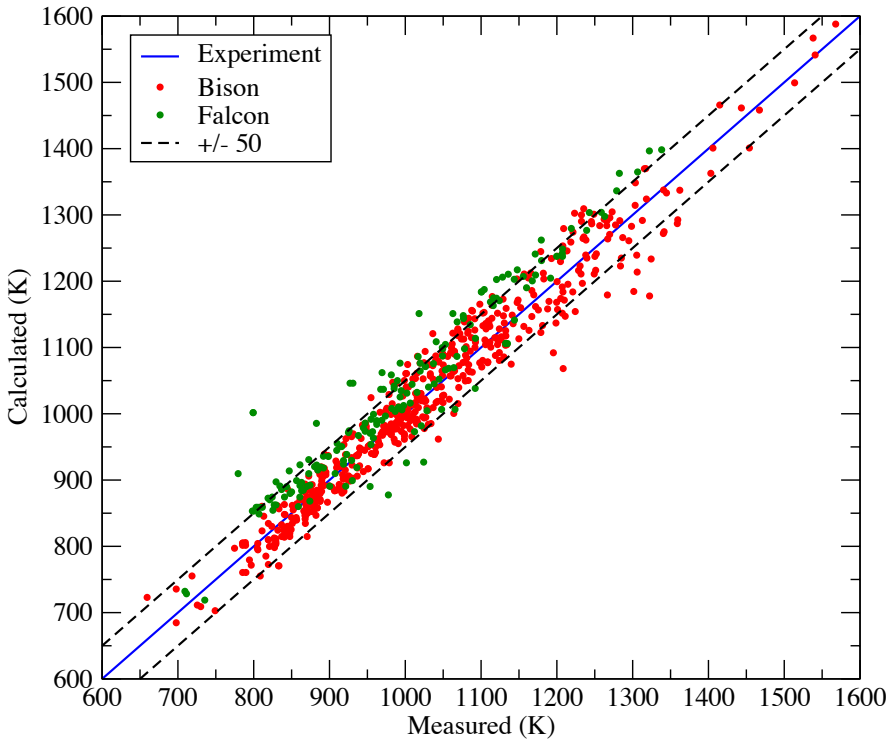

Figure 2-5. Calculated versus measured fuel centerline temperatures for the thermal benchmarking performed to date. The Bison predictions are shown as red circles, whereas the corresponding Falcon calculations are shown as green triangles.

2.2.B Mechanical Benchmark Analysis

The comparisons of Bison predictions of fuel centerline temperatures provide a good level of confidence in the current status of the Bison fuel performance code, and the next step towards the goal of developing predictive PCI failure probabilities is to benchmark the mechanical deformation predicted in the fuel cladding. It is important to note that predicting clad failures during PCI requires the ability to predict both steady state irradiation behavior as well as fuel performance during temperature-power ramp irradiations. The effort to benchmark the mechanical deformation has been performed systematically, first looking at the deformations resulting from thermal expansion and irradiation growth of clad due to the exposure to fast neutron irradiation, followed by clad deformation induced by thermal and irradiation creep. Again, these benchmark comparisons will involve the calculation of clad deformation during a steady-state or base irradiation, to a given burnup, followed by a ramp increase in power. Several cases were selected for the validation process, as presented in Table 2-3. This chapter will present the results for the comparisons from the IFA_562.1 rod 5, RISØ AN2 and AN8 rods, as well as the Super-Ramp PK2 rod tests.

Table 2-3. Description of Halden IFA, RISØ Fission Gas and Super Ramp test rods selected for mechanical benchmark studies and key characteristics of each rod

Mechanical Benchmark Cases		
Test Rod	**Burnup (MWd/kg UO_2)**	**Key Characteristics**
IFA 585.4	Defueled	Zr-4 cladding creep test by radiation flux
IFA 562.1 rod 5	~10.75	Irradiation induced cladding elongation
IFA 562.1 rod 11	~10.75	Irradiation induced cladding elongation
RISØ AN2	~37	Clad diametral change: base irradiation and power ramp
RISØ AN8	~37	"
Super-Ramp PK2-1	~38	"
Super-Ramp PK2-3	~38	"
Super-Ramp PK2-S	~38	"

IFA 562.1 contained axial elongation measurements at several different burnups. These measurements were conducted to analyze the effect of irradiation growth on the clad axial displacement [37-38]. Figures 2-6 and 2-7 present the Bison predictions compared to the measured axial displacement of the cladding. It is important to note that the Bison calculations were performed using a slip or zero friction model and did not model a plenum spring. This will certainly influence the results once the fuel-clad gap closes.

For the low burnup of 0.2 MWd/kg UO_2, the Bison prediction of clad axial displacement shown in Figure 2-6 is in good agreement with the measured axial displacement to a linear heat rate of about 25 kW/m. At these burnup and power levels, the majority of the clad displacement results from thermal expansion due to the clad temperature distribution and external forces, e.g plenum pressure, coolant pressures, and plenum springs. Beyond 25 kW/m, the measured values increase rapidly with increasing linear power and seem to indicate that the fuel-clad gap has closed. Therefore the increasing clad displacements may result from stress transfer from the fuel-clad contact.

Figure 2-7 shows the axial clad displacement experimentally measured as compared to the Bison predictions as a function of linear heat rate for fuel with an initial burnup of 9.1 MWd/kg UO_2. It is important to note here that while the difference between the model and experiments is much greater than shown in Figure 6, we believe this could again be related to deformation driven by the mechanical contact, stress transfer from the fuel to the clad following gap closure, and axial forces that are generated by the plenum spring. As well, since this test started with fuel of higher burnup, it is possible that the initial difference at low linear power is due to an inaccurate assessment of the fast neutron flux history of the cladding. The specific fast neutron flux history for the burnup of 9.1 MWd/kg UO_2 was not provided and we have assumed a fast flux profile based on the power history.

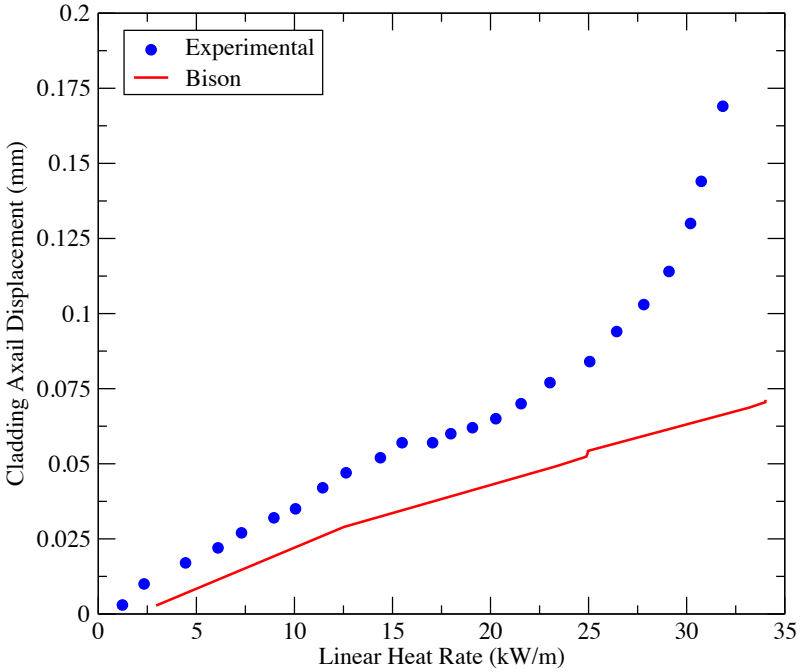

Figure 2-6. Bison predictions (red line) of clad axial displacement due to irradiation growth compared to those experimental measured (blue dots) for a rod with initial burnup of 0.2 MWd/kgUO_2

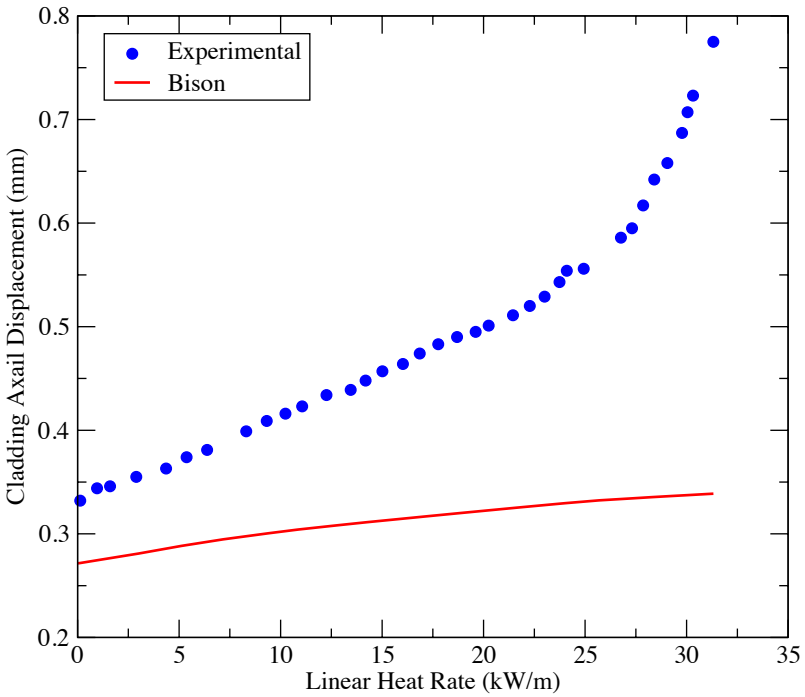

Figure 2-7. Bison predictions (red line) of clad axial displacement due to irradiation growth compared to those experimental measured (blue dots) for a rod with initial burnup of 9.1 MWd/kgUO_2.

The next set of mechanical benchmark cases considered were from the Third RISØ Fission Gas Project [39-40], and the rod segment that were chosen are AN2 and AN8. The base irradiation of the test rods was conducted in the Biblis PWR, under prototypical coolant temperatures of 285°C and pressure conditions of 15.5 MPa. The AN2 and AN8 fuel rod experiments contained fuel columns of solid pellets of approximately 0.54 meters in length. The cladding on these test rods was a cold worked stress-relieved (CWSR) Zr-4 with a zirconium liner. The base irradiation power history consisted of four cycles of irradiation in a commercial reactor. Each fuel rod segment was subsequently ramped in the DR-3 test reactor under PWR conditions. Rod diametral profiles were recorded during PIE following both the base irradiation and the power ramp tests [39-40]. For modeling the RISØ rods, Bison currently does not have material models for the zirconium liner, and it is assumed the zirconium liner is part of the Zr-4 cladding. Figures 2-8 through 2-11 show Bison calculation comparisons to the experimental measurements for the change in diameter as a function of axial position along the rod for the different experimental conditions.

The results from the RISØ AN2 case, shown in Figure 2-8, clearly indicate good agreement between the Bison prediction and the experimental measurements of cladding creep down due to the base irradiation in the Biblis reactor up to a burnup of 42 MWd/kg UO_2. The experiment contained an end plug and plenum spring located in the region of ~580-620 mm which was not included in the Bison model, and this is responsible for the discrepancy at the top end of the fuel rodlet. As well, Bison modeled the lower end similar to the upper portion of the rod. The axial mesh in the clad may be too coarse, thereby producing linear interpolation errors that explain the discrepancy of the model predictions in the lower several mm of the fuel rod. However, in general, the agreement of the change in diameter associated with the creep down of the clad between the experiments and modeling results is excellent.

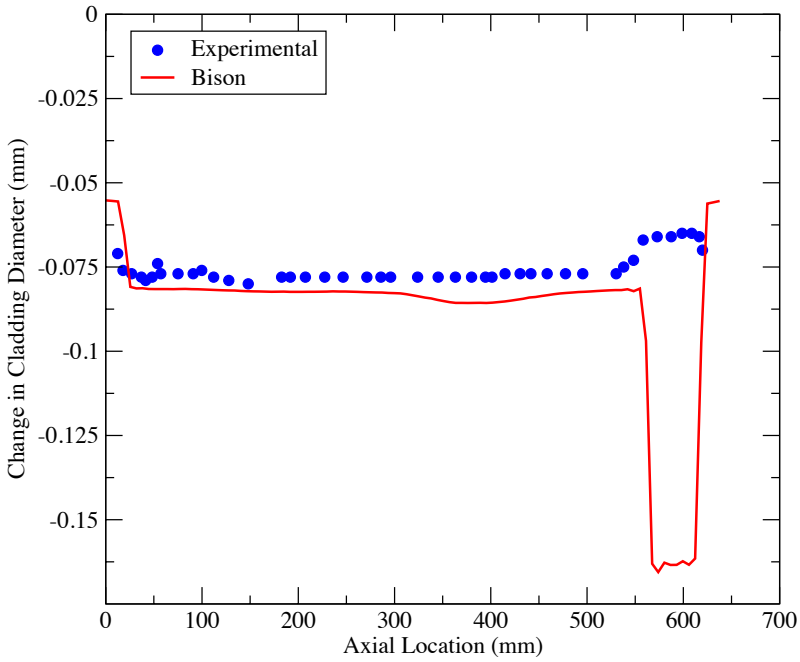

Figure 2-8. Bison predictions (red line) of change in clad diameter, resulting from steady irradiation in the power reactor Biblis for the rodlet AN2, as compared to the experimental measurements shown in blue.

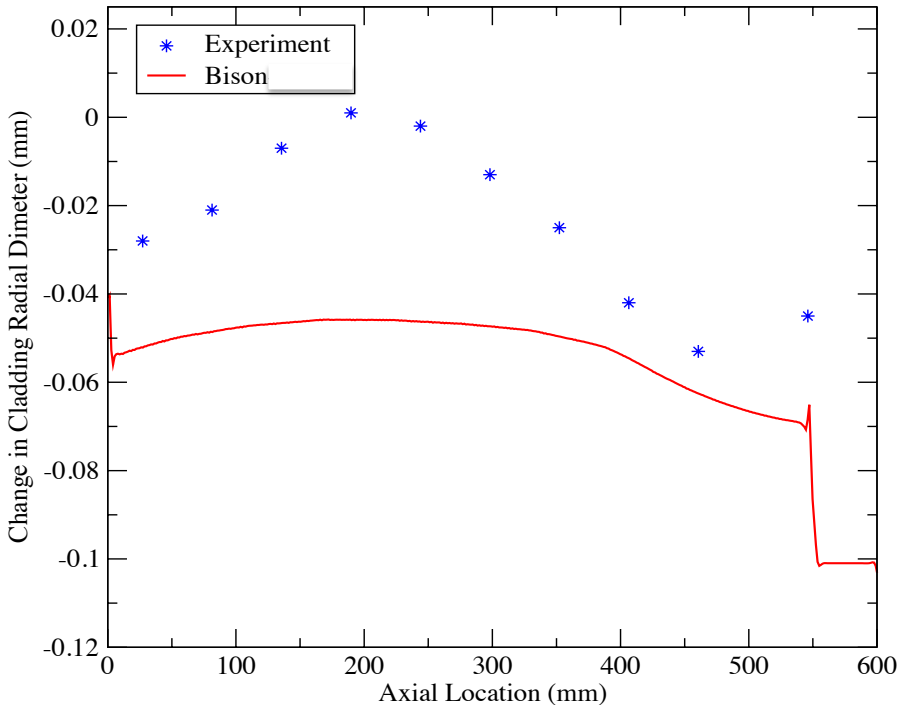

Figure 2-9. Bison predictions of change in clad diameter for the AN2 fuel rod during the power ramp (red line) and following cool down to room temperature (green line), as compared to the experimental measurements which were performed following removal of the fuel rod from the reactor.

Figure 2-9 shows the comparison between the Bison predictions and the experimental measurements following the RISØ ramp test, in which the power was ramped in the test reactor DR3 in a water cooled HP1 rig under PWR conditions. The ramp cycle consisted of ramping to 300 W/cm in ~5 hours and then holding this linear power for five hours. Following the hold at 300 W/cm, the power was then ramped up to 390 W/cm and held ~60 hours before shut down to zero power [39-40]. Cladding deformation during the ramp experiment is mainly caused by fuel swelling and stress transfer to the clad following gap closure, which acts to increase the clad diameter following the creep down stage. The fuel swelling is caused by a combination of fuel thermal expansion with increasing power and temperature and the solid and gaseous fission products. The models of solid fission product swelling of UO_2 are believed to be reasonably reliable, and Bison uses the MATPRO fuel swelling model. However, the swelling due to gaseous fission products is much more complicated, since the amount of swelling depends on the number density of fission gas bubbles as well as the release-to-birth ratio of the gaseous fission products. As can be seen in Figure 2-9, Bison has modeled the change in clad diameter following the removal of the fuel rod from the reactor for the diametral measurements. Overall, the model predictions track the axial variation of the diameter change poorly. Bison is under-predicting the clad deformation, which we believe is due to smeared cracking and swelling of gaseous fission products. Smeared cracking accounts for the pellet cracking when subject to very high internal stresses. This fracture mechanism causes the fuel to expand, almost instantaneously, closing the gap or exerting force on the cladding. Secondly, gaseous swelling accounts for the fission gas that remains inside the UO_2

matrix in the form of bubbles. These bubbles, when subjected to high delta T's, will expand causing the fuel to expand. Both of these mechanisms will have significant contributions to the expansion of the fuel and cladding deformation.

Figures 2-10 and 2-11 show results for the RISØ AN8 rodlet, first for the clad creep down following removal from the Biblis power reactor at a burnup of 42 MWd/kgUO_2 and then following the ramp irradiation in the DR3 reactor, respectively. Figure 2-10 shows a reasonable agreement of the axial variation for clad creep down but with a clear under-prediction in the magnitude of the change in clad diameter in the lower segment of the rod to about 300 mm. The disagreement at the lower position of the rod may be due to changes in the neutron flux spectrum resulting from the grid supports included in the RISØ Fission Gas project but that were not accurately included in the model predictions. Overall, the axial variation of the clad creep down is reasonable.

Figure 2-11 shows the comparison between the Bison predictions and the experimental measurements following the RISØ ramp test, in which the power was ramped in the DR3 reactor. The ramp cycle consisted of conditioning the rod at 220 W/cm for 4-6 hours, with an ensuing ramp to 298 W/cm which was held for ~5 hours before shut down [39-40]. As was the case for the AN2 rodlet, the Bison predictions do a reasonable job of modeling the axial variation but clearly are under-predicting the deformation on the lower portion of the rod. Again, this is not surprising since swelling from the gaseous fission products is not explicitly included in the model. However, the disagreement and under-prediction of the clad deformation during the ramp test is more striking since in this region of the rod Bison also under-predicted the amount of creep down of the clad during the base irradiation in the power reactor. Clearly this indicates that Bison is either under predicting the fuel swelling, which is responsible for the clad deformation during the ramp test, or the stress transfer from the fuel to the clad as a result of the fuel swelling into the clad following gap closure.

For both the AN2 and AN8 rods, it is again important to note that Bison does not currently have an appropriate pure Zr material model to correctly account for the zirconium liner, and thus, it has been modeled as a layer of Zr-4. We expect this assumption will produce lower predictions of cladding creep down than if the pure Zr liner were explicitly included. Therefore, it is expected that Bison will predict more cladding creep down with the inclusion of a zirconium liner.

While the initial comparisons to the RISØ experiments do not provide good quantitative agreement, the model predictions generally predict the overall behavior, especially related to the axial variation of the clad deformation, despite the need to incorporate a new model for gaseous fuel swelling. Thus, the mechanical benchmark comparisons were continued by modeling the Super Ramp experiments, which also couple clad creep down and fuel swelling. The purpose of the Super Ramp project was to gain a better understanding of fuel rod failure due to pellet clad interactions in typical LWRs. We selected the PK2 test rods for this benchmark. These rods were approximately 0.32 meters in length, were pressurized with helium to a pressure of 22.5 bar, and subjected to a base irradiation to a burnup of 44 MWd/kgUO_2 and a fluence of 8.1E25 neutrons (E > 1 MeV) per m^2. The base irradiation was performed in the commercial PWR Obrigheim. After the base irradiation, the fuel rods underwent non-destructive examinations to measure the rod diameter. The test rods were then transported to the R2 reactor for ramp testing, after which the diametral changes were measured for a second time [41]. All of the dimeteral measurements presented here are average values over multiple measurements. It is important to note that in the Bison modeling of the base irradiation and ramp tests, we have assumed a uniform axial profile for the power profile and fast neutron flux.

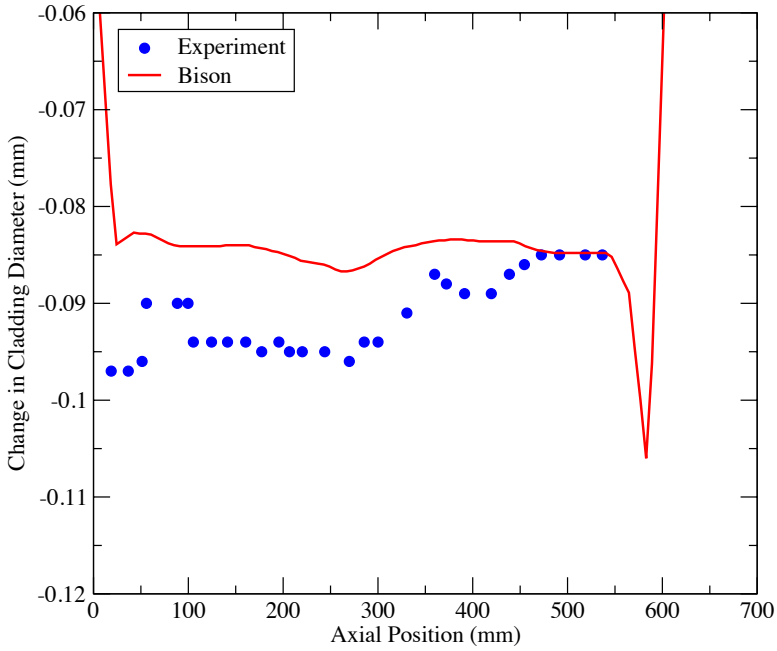

Figure 2-10. Bison predictions (red line) of change in clad diameter, resulting from steady irradiation in the power reactor Biblis for the rodlet AN8, as compared to the experimental measurements shown in blue.

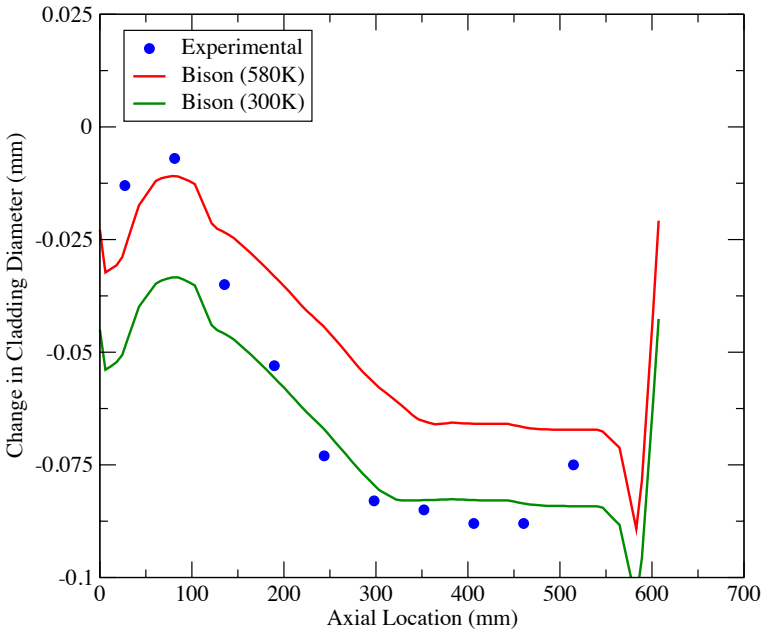

Figure 2-11. Bison predictions of change in clad diameter for the AN8 fuel rod during the power ramp (red line) and following cool down to room temperature (green line), as compared to the experimental measurements which were performed following removal of the fuel rod from the reactor.

The RISØ cases indicated that Bison was predicting of clad creep down well but generally under predicting clad expansion following gap closure with subsequent fuel swelling. Table 2-4 presents the initial and measured diameter for three rods in the PK2 ramp, following the base irradiation in the Obrigheim (KWO) commercial PWR, after which the ramp tests were performed in the R2 reactor. The ramp cycle consisted of a slow increase of the linear power to 250 W/cm and was conditioned for 24 hours. Following the conditioning phase, a ramp in power of ~ 100W/cm-min was performed to reach to the peak power level of ~ 410 W/m and held for 6 hours [41]. Also included in Table 2-4 are the Bison predictions, which indicate a small under-prediction of the amount of clad creep down during the power reactor irradiation, although the agreement is reasonable. The rods in the Super Ramp test have a much smaller gap than those in the RISØ experiment, which means that gap closure will occur sooner in the Super Ramp tests. As stated previously, the thermal expansion and swelling of the fuel drive clad deformation in the transition from creep down to diametral expansion. After comparing the fuel swelling models implemented in Bison and Falcon, it appears that Bison is over-predicting fuel swelling during the PWR irradiation by about 30%, which is consistent with the under-prediction of the clad creep down during PWR irradiation. Subsequently, Bison predicts diametral growth in the clad during the ramp irradiation although the amount of diameter increase during the ramp test (compared to that following PWR operation) is generally less than experimentally observed. This is consistent with the RISØ cases, in which due to poor modeling of fission gas swelling, Bison is under-predicting the clad deformation during the ramp test. In the PK2 ramp tests, Bison over-predicts fuel swelling during the base PWR irradiation, which results in under-predicting the amount of clad creep down. Since the over-predicted fuel swelling and gap closure limits clad creep-down within our model predictions, it is not unexpected that the clad deformation is over-predicted during the subsequent power ramp.

Table 2-4. Comparison of Bison predictions to experimental measurements for three rods from the Super Ramp project.

		Base Irradiation			Ramp Irradiation		
Test Rods	Initial Diameter (mm)	Measured Diameter (mm)	Predicted Diameter (mm)	Difference (μm)	Measured Diameter (mm)	Predicted Diameter (mm)	Difference (μm)
PK2-1	10.753	10.668	10.70	32	10.704	10.717	13
PK2-3	10.752	10.677	10.698	21	10.778	10.736	-42
PK2-S	10.754	10.664	10.698	34	10.674	10.728	54

2.2.C Fission Gas Release Analysis

2.2.C.1 RISØ Rods – Base Irradiation

Figure 2-12 and 2-13 show fission gas release fraction calculated using different models in Bison for AN2 and AN8 respectively. The Forsberg-Massih model predicts the thermal fission gas release starting at ~26 MWd/kgUO_2, which coincides with the onset of the rapid release predicted by the Sifgrs model, while the thermal fission gas release predicted by the Sifgrs model appears to start at a lower burnup ~10 MWd/kgUO_2 for AN2 and ~16 MWd/kgUO_2 for AN8. The decrease of fission gas release with burnup calculated using the Forsberg-Massih model indicates the fission gas atoms newly accumulated after previous release have not been released. Sifgrs model, computing a gradual increase of fission gas release instead, gives rise to a higher FGR at the end of the base irradiation.

Results of fission gas release using Falcon and Bison code calculations for AN2 and AN8 test rods at the end of base irradiation are shown in Table 2-5 measured fission gas release fraction based on sibling rods is also shown in **Table** 2-5 for comparison. .02% fission gas was measured from sibling rods, which could be primarily caused by the athermal fission gas release. Falcon calculation is also lower than the athermal fission gas release of 0.07% calculated using the Sifgrs model. Both the Sifgrs model and the Forsberg-Massih tend to predict higher fission gas release; the amount of the thermal release alone is higher than the measurement.

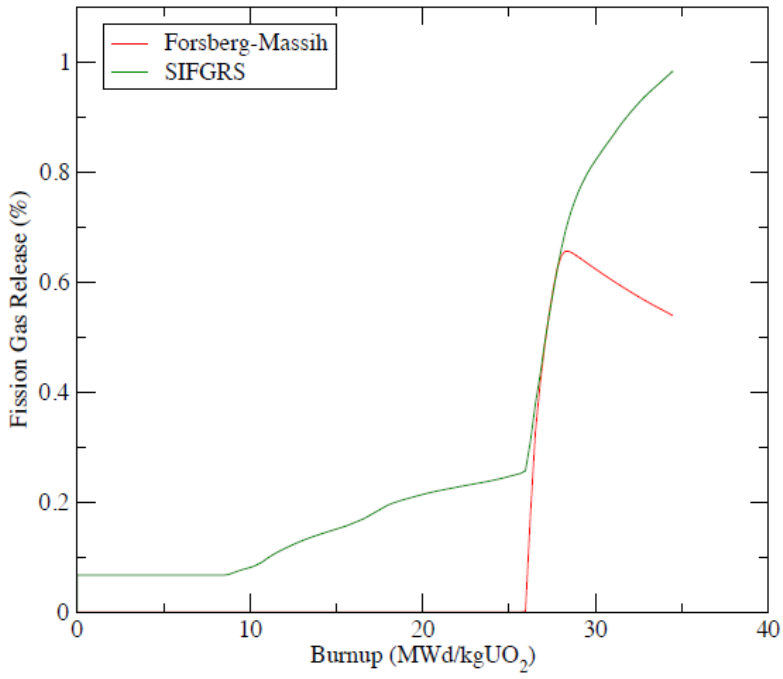

Figure 2-12. Fission gas release fraction calculated using different models in Bison for RISØ AN2 test rod in base irradiation

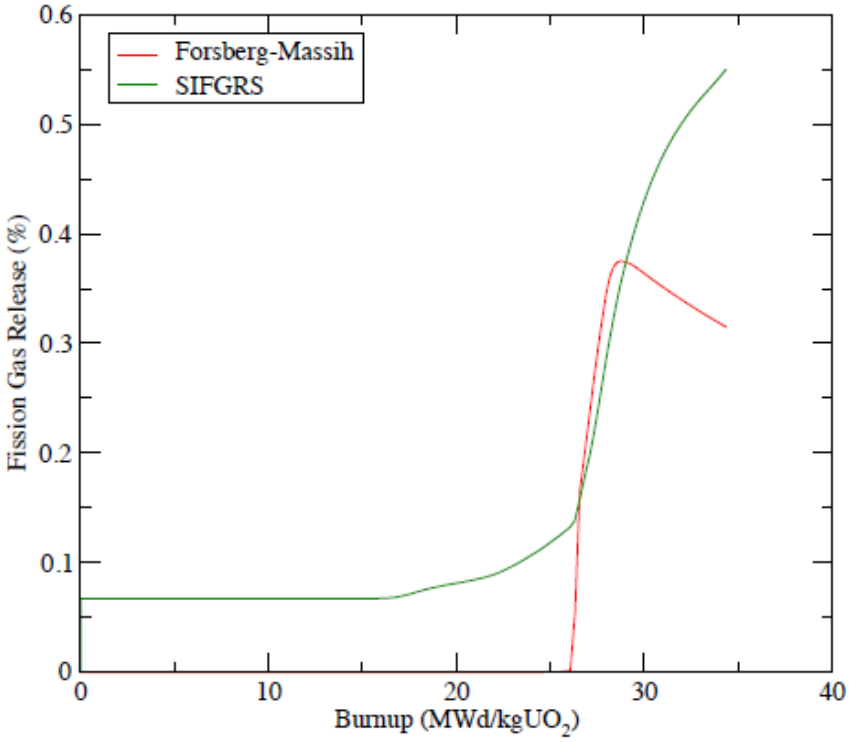

Figure 2-13. Fission gas release fraction calculated using different models in Bison for RISØ AN8 test rod in base irradiation

Table 2-5. Comparison of FGR between Falcon, Bison, and Measurements for RISØ AN2 and AN8 Test Rods at the End of Base Irradiation

	Calculated FGR (%)				Measured FGR (%)
	Falcon	Bison			
		Sifgrs	Sifgrs athermal	Forsberg-Massih	
AN2	0.01	1.0	0.07	0.6	0.2
AN8	NA	0.6	0.07	0.3	0.2

2.2.C.2 RISØ Rods – Power Ramp

Figure 2-14 and Figure 2-15 show the fission gas release fraction during the power ramp calculated using the Sifgrs model and the post-ramp measurement of fission gas release for RISØ AN2 and AN8 test rods respectively. Results for the Forsberg-Massih model are not included. The Forsberg-Massih model dose not have a fission gas release model for a power ramp, and it would not calculate any fission gas release over the short period of time.

It appears that the Sifgrs model can capture the large amount of fission gas release during the power ramp. However, code calculations underestimate the fission gas release; the error for AN2 is ~5% FGR and the error for AN8 is ~4% FGR. Falcon calculation was performed on AN2 and AN8, and the results of post-ramp FGR in comparison to Bison calculations and measurement are provided in Table 2-6.

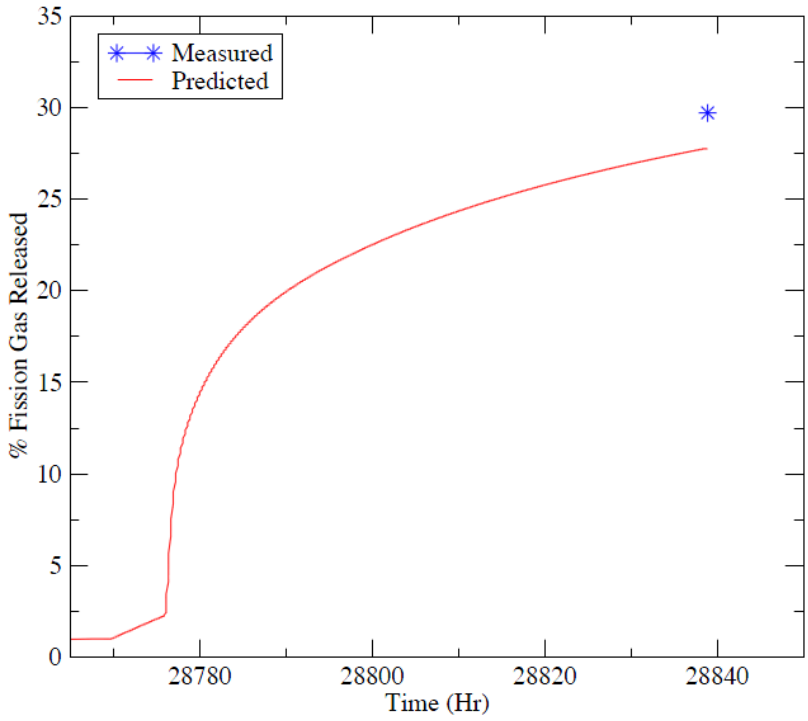

Figure 2-14. Fission gas release fraction for RISØ AN2 test rod during the power ramp calculated using the Sifgrs model and the post-ramp measurement for comparison

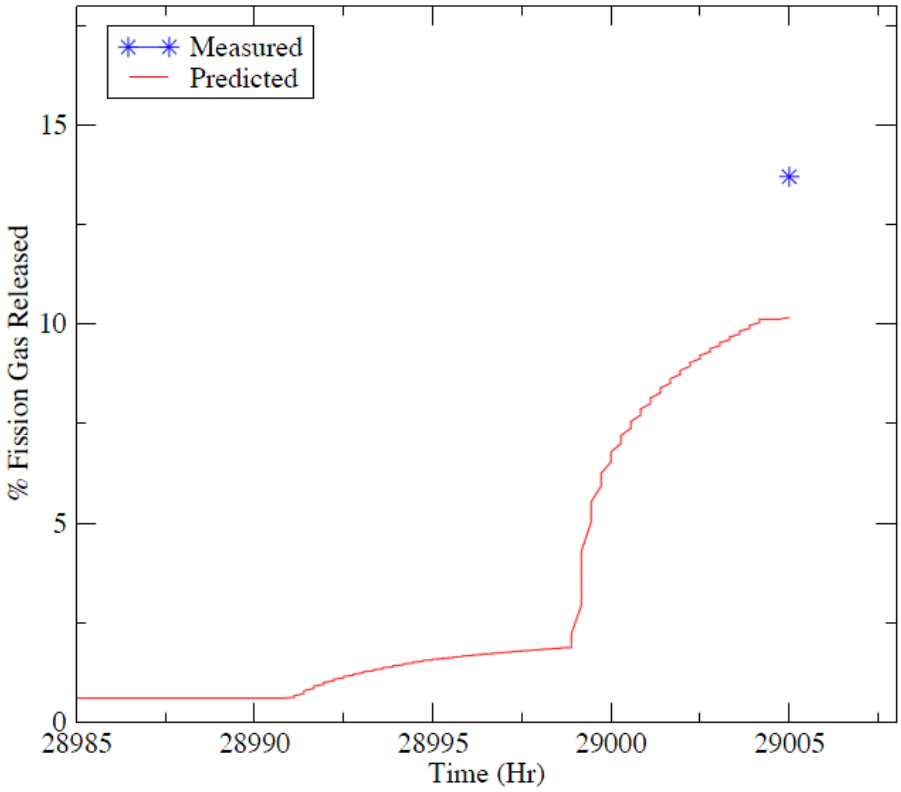

Figure 2-15. Fission gas release fraction for RISØ AN8 test rod during the power ramp calculated using the Sifgrs model and the post-ramp measurement for comparison

Table 2-6. Comparison of Post-ramp FGR between Falcon, Bison, and Measurements for RISØ AN2 and AN8 Test Rods

	Calculated FGR (%)		Measured FGR (%)
	Falcon	Bison	
AN2	29.4	25.1	29.7
AN8	NA	10.2	13.7

2.2.C.3 Super-Ramp Rods – Base Irradiation

Fission gas release during the base irradiation was calculated using the Sifgrs model and the Forsberg-Massih model in the Bison code for PK2 rods. Results for PK2-1, PK2-3, and PK2-S test rods are shown in Figure 2-16, Figure 2-17, and Figure 1-18 respectively.

For PK2 rods, both the Forsberg-Massih model and the Sifgrs model show an incubation period up to ~18-22 MWd/kgUO_2 before an apparent thermal release. The calculated fission gas release at the end of the base irradiation ranges from 1.2% to 2.3%. Similar to the results of RISØ AN2 and AN8, the Forsberg-Massih model appears to predict slightly lower fission gas release than the Sifgrs model, and the Forsberg-Massih model describes the intermittent release while the Sifgrs model computes a more smooth increase of fission gas release.

No measured fission gas release at the end of the base irradiation was available for the Super-Ramp test rods. Bison calculations were compared to Falcon calculations for PK2-1, PK2-3, and PK2-S test rods at the end of the base irradiation, and the results are shown in Table 2-7.

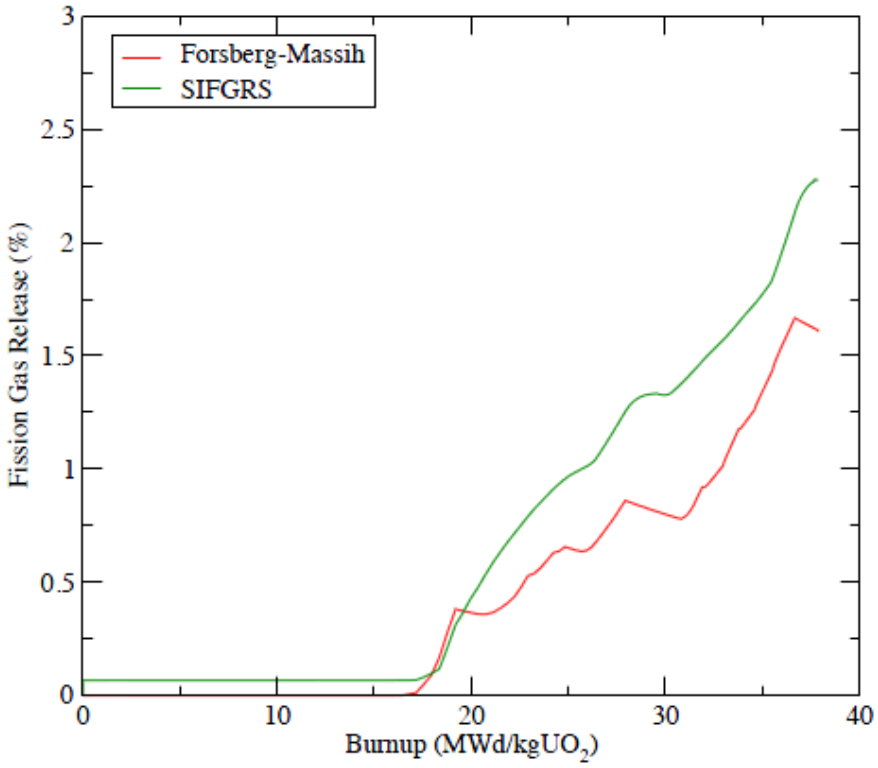

Figure 2-16. Fission gas release calculated using different models in Bison for Super-Ramp PK2-1 test rod in the base irradiation

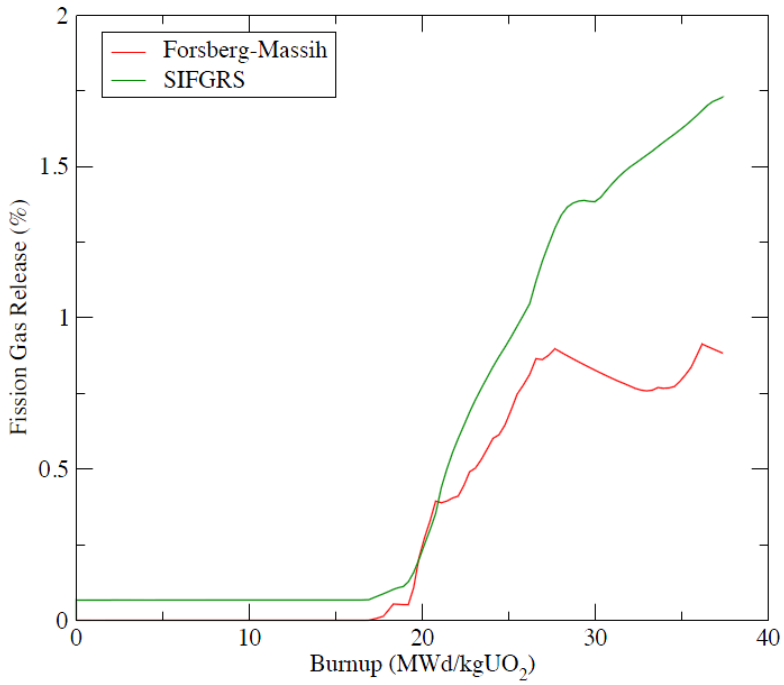

Figure 2-17. Fission gas release calculated using different models in Bison for Super-Ramp PK2-3 test rod in the base irradiation

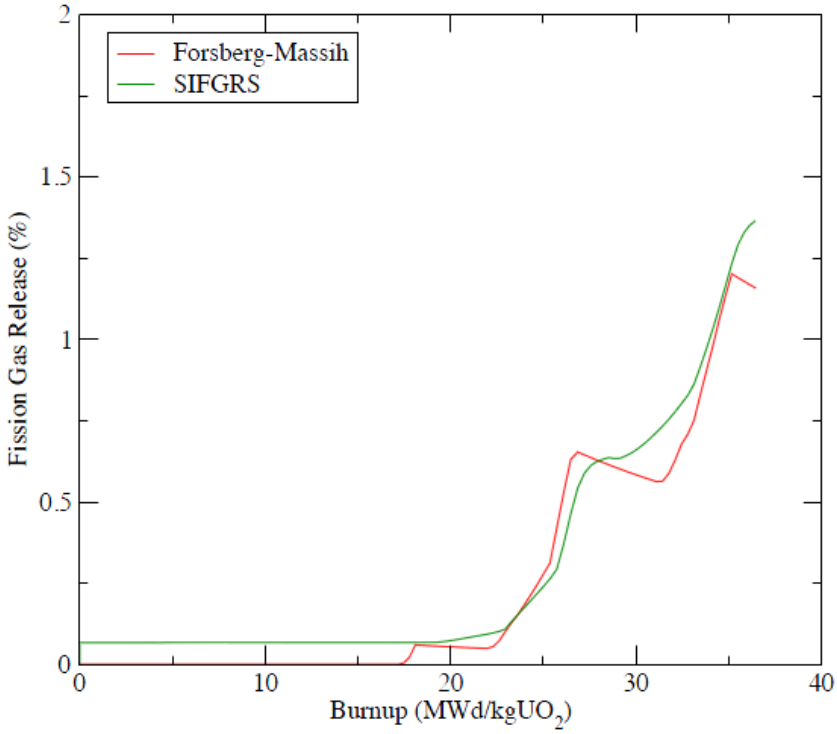

Figure 2-18. Fission gas release calculated using different models in Bison for Super-Ramp PK2-S test rod in the base irradiation

Table 2-7. Comparison of FGR between Falcon, Bison, and Measurements for Super-Ramp PK2-1, PK2-3, and PK2-S Test Rods at the End of Base Irradiation

	Calculated FGR (%)				Measured FGR (%)
	Falcon	Bison			
		Sifgrs	Sifgrs athermal	Forsberg-Massih	
PK2-1	0.020	2.28	0.07	1.61	-
PK2-3	0.019	1.73	0.07	0.88	-
PK2-S	0.018	1.37	0.07	1.16	-

2.2.C.4 Super-Ramp Rods – Power Ramp

Figure 2-19, Figure 2-20, and Figure 2-21 show the fission gas release fraction during the power ramp calculated using the Sifgrs model and the post-ramp measurement of fission gas release for PK2-1, PK2-3, and PK2-S respectively. The Forsberg-Massih model in the Bison code predicts no fission gas release during the power ramp, thus is not included in the results.

PK2 test rods have significant amount of fission gas release during the power ramp. Bison code calculations using the Sifgrs model can simulate the large amount of fission gas release with the difference between code calculation and the measurement being ~10% FGR.

Falcon calculation was performed on AN2 and AN8, and the results of post-ramp FGR in comparison to Bison calculations and measurement are provided in Table 2-8. It appears that the fission gas release fraction calculated using the Bison Sifgrs model is comparable to Falcon results, although the Falcon code calculated lower FGR than the Bison code. Both codes underestimate FGRs for PK2-1 and PK2-3 but overestimate the fission gas release for PK2-S. Note that the PK2-S has lower coolant temperature and lower cladding temperature than other PK2 rods, and this could be the reason for the relative lower FGR and lower cladding hoop strain than other rods.

A number of cases based on test rods data from a few international programs were prepared to run Bison code with different fission gas release models. Bison code calculations were compared to Falcon code calculations and the measured fission gas release, which was obtained either from test rods directly or from sibling rods.

The selection of test cases covers a rod average burnup level of 33 - 75 MWd/kgUO_2, and includes normal power operations and power ramp conditions. Measured fission gas release fraction for the test cases ranges from 0.2% to 45%. Table provides a summary of fission gas release fraction calculated using the Bison code compared to experimental data and Falcon code calculations.

Measured fission gas release fraction for the benchmark cases varies from 0.2% up to 2% for the low fission gas release regime which may include both thermal fission gas release and

athermal fission gas release. Fission gas release model in Bison can generally capture the low fission gas release, i.e., the code calculation is still in the regime of low fission gas release, although it is difficult to distinguish a small amount of thermal fission gas release from athermal fission gas release, which requires a more precise prediction of the incubation period of the thermal fission gas release. It could be an area of improvement. Analyses of a few high burnup rods (IFA 515 A1, 562.2 rod 15 and rod 16) show that improvement might also be needed to account for the effect of high burnup structure.

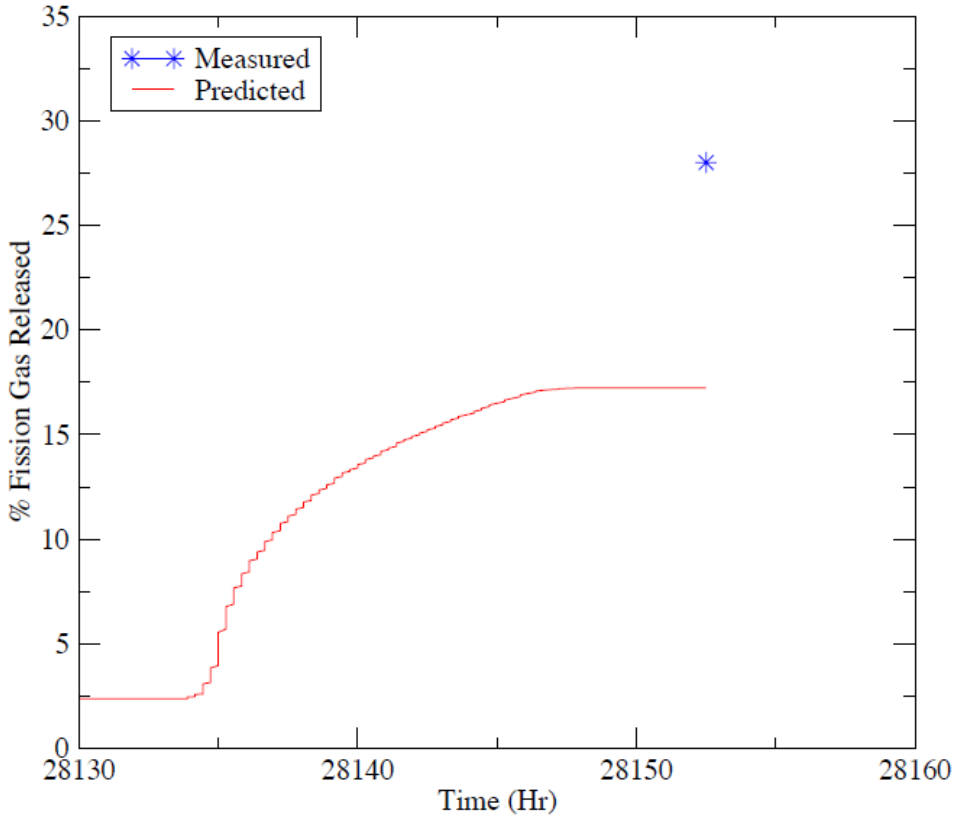

Figure 2-19. Fission gas release fraction for PK2-1 test rod during the power ramp calculated using Sifgrs model and the post-ramp measurement for comparison

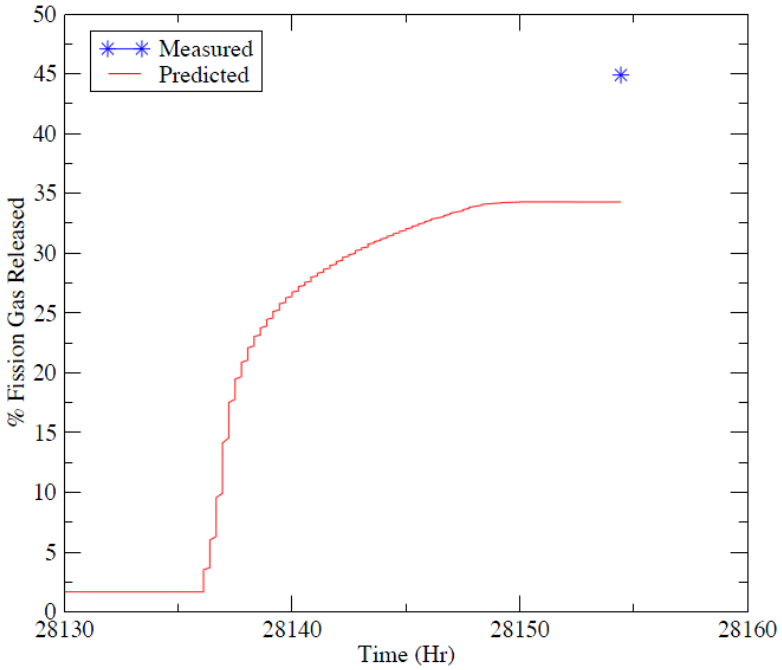

Figure 2-20. Fission gas release fraction for PK2-3 test rod during the power ramp calculated using Sifgrs model and the post-ramp measurement for comparison

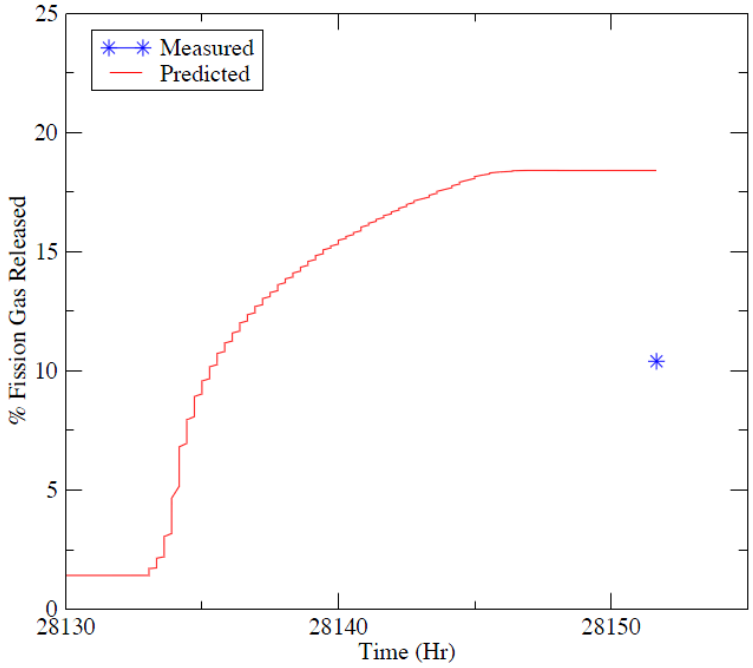

Figure 2-21. Fission gas release fraction for PK2-S test rod during the power ramp calculated using Sifgrs model and the post-ramp measurement for comparison

Table 2-8. Comparison of Post-ramp FGR between Falcon, Bison, and measurements for Super-Ramp PK2-1, PK2-3, and PK2-S test rods

	Calculated FGR (%)		Measured FGR (%)
	Falcon	Bison	
PK2-1	13.7	17.4	28.0
PK2-3	25.8	34.5	44.9
PK2-S	14.8	18.6	10.4

Table 2-9. Summary of Bison calculation of FGR compared to experimental data and Falcon calculations

Test Rod	Burnup MWd/kgUO_2	Measured (%)	Bison (%)	Falcon (%)
IFA-505.5 Rod 1	33	5-15	5-8	13
IFA-515 A1	75	<1	0.11	NA
IFA-562 Rod 15	50	1.1	0.103	NA
IFA-562 Rod 16	56	<2	0.103	NA
RISØ AN2 Base Irradiation	37	0.2	0.6-1.0	0.01
RISØ AN2 Post-ramp	37	29.7	25.1	29.4
RISØ AN8 Base Irradiation	37	0.2	0.3-0.6	0.01
RISØ AN8 Post-ramp	37	13.7	10.2	NA
SuperRamp PK2-1 Base Irradiation	39	-	1.6-2.3	0.02
SuperRamp PK2-1 Post-ramp	39	28	17.4	13.7
SuperRamp PK2-3 Base Irradiation	39	-	0.88-1.73	0.019
SuperRamp PK2-1 Post-ramp	39	44.9	34.5	25.8
SuperRamp PK2-S Base Irradiation	39	-	1.16-1.37	0.018
SuperRamp PK2-S Post-ramp	39	10.4	18.6	14.8

A comparison of fission gas release fraction between the experiment and code calculations for the power ramp condition is shown in Figure 22. The difference between the Bison code calculations using the Sifgrs model and measurements is ~10% FGR, which is comparable to the Falcon code prediction error, having shown the code's capability of computing high fission gas release.

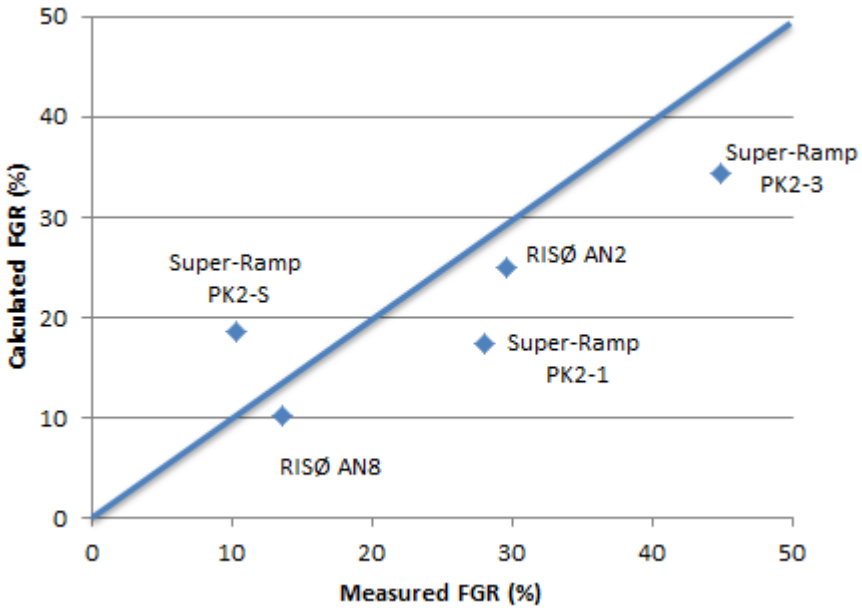

Figure 2-22. Comparison of fission gas release fraction between the measurement and Bison calculations

Overall, the preliminary benchmark results for the tests case covering a number of operating conditions have shown that Bison code has the general capability of modeling fission gas release. However, the modeling of fission gas release has been a challenging part in nuclear fuel performance codes; existing models in fuel performance codes generally do not provide a versatile capability of predicting fission gas release which could result from different fuel materials at various operating and accident conditions. It can be seen that the combination of several models is necessary to account for different mechanisms involved in the fission gas release process. Expansion of the validation database to include different operating regimes is necessary to further test the capabilities of the mechanistic models in the Bison code and to identify the missing mechanisms in current models to make improvements. For example, the current benchmark cases do not have cases with appreciable amount of fission gas release in steady state operations except for IFA 505.5 rod1. Such cases, however, could be of more relevant to the operating conditions of commercial reactor fuels. Further development of more

physics-based fission gas release models is also of interest to reduce the reliance on the empirical knowledge in current models and to develop/improve the predictability of fission gas release model.

Current model validation is largely based on the total amount of measured FGR at the end of life, which could have missed some important aspects of the fission gas release process such as the incubation period of thermal release, contribution of fission gas release from different fuel microstructures, fuel restructuring at high burnup, et. al. Detailed PIE data of relative fractions of isotopes and distribution of gaseous products in the fuel matrix are available in some experiments. They have not been used in the benchmark due to the limitation of current models and the processing capability of the Bison code. They provide valuable information regarding the fission gas release behavior; and it would be of interest to use such information to assist the development of advanced modeling capability.

2.3 Summary

Current updated thermal benchmarking has demonstrated that Bison is predicting fuel centerline temperature quite accurately, with the Falcon and Bison predictions falling within a ±50° band in comparison with the experimentally measured fuel centerline temperatures. In general, Falcon tends to over-predict fuel centerline temperature whereas Bison tends to under-predict the value. More detailed comparisons between Falcon and Bison indicate differences between the two for gap closure and gap conductance, which highlight the need to continue to refine and improve the physical fidelity of a number of key sub-models, including fission gas release, fuel creep and densification, gap conductance and the smeared crack and relocation models; all of which will impact the temperature distributions within the fuel.

Preliminary assessment of mechanical models and fission gas release models indicates that the Bison code could have similar capabilities compared to Falcon code. Reasonable agreement with experimental data can be achieved for most cases in terms of the calculation of cladding creep down, capturing the low fission gas release regime, and simulating the high fission gas release during a power transient. Areas of improvements involving complex interactions between multiple mechanisms are identified. Expansion of current V&V database is needed to further test current codes' capability and to assist the development towards a more physics-based model.

The results highlight the importance of several aspects of fuel rod behavior; particularly pellet cracking and relocation, and fission gas release. The advanced 3-D modeling capabilities of Bison will require a more mechanistic representation of these behavior in order to model the fundamentals of PCI.

Chapter 3: Idealized PCI/MPS

The objective of developing an advanced, 3-D fuel performance modeling capability to assess PCI is to: 1) reliably calculate the cladding failure potential related to PCI; 2) define the impact of manufacturing flaws along with the material properties on failure probability; and 3) to evaluate the role of plant operating strategies as well as specific fuel designs on the PCI failure potential. To meet these objectives, it is imperative to develop a high-fidelity, fully coupled computer code that incorporates important plant operating procedures, e.g. power ramp rate and axial power shapes related to fuel performance, as well as considering the inherently coupled intricacies that occur in irradiated fuel behavior during normal and transient operations. By developing and employing an advanced fully coupled multi-physics and multi-dimension fuel performance code and developing mechanistic or physics based material models, efforts can be taken to reduce the uncertainties surrounding existing PCI failure methods. The approach to address the current uncertainties in PCI failure probabilities will allow for improved fuel utilization and increase the plant operating flexibility.

The focus of this chapter is to assess the capability of Bison as a 3-D fuel performance code to represent the underlining mechanisms controlling the failure of the cladding as a result of PCI. As mentioned in Chapter 1, the processes leading to cladding crack initiation and propagation begins with the presence of localized stress and strains along with corrosive fission products. PCI fuel behavior modeling must be built upon a methodology that can reliably and consistently calculate the local stress conditions as a function of prior irradiation history, material properties, and local power conditions. This means capturing the effects of geometric irregularities (i.e. pellet cracks), permanent changes in dimensions of the pellet and cladding caused by fission product swelling and irradiation-induced cladding creep, as well as, thermal, mechanical, and chemical interactions between the pellet and cladding, i.e. frictional forces, heat transfer, and chemical bonding.

The assessment first focuses on the approach to model pellet cracks and MPS defects using a 2-D planar geometric representation (R-theta model) in order to capture the impact of these geometric irregularities on the localized cladding stress and temperature distribution. Other researchers, including those funded by EPRI [42,43], have used a 2-D approach to calculate pellet-cladding mechanical interaction as part of a PCI analysis methodology. Therefore, starting with a 2-D approach allows for both quantitative and qualitative comparisons to previous results, providing assurance that the capabilities in Bison are consistent with established methodologies. The 2-D modeling in Bison was used to investigate the impact of pellet crack radial length as well as pellet crack frequency on cladding stress localization. In the case of a MPS defects, the 2-D approach was used to quantify the influence of the MPS defect shape (width and depth) on the cladding stress and fuel temperature distribution. Concentrating on modeling PCMI using a 2-D planar approach also provides a learning process to be conducted where the influence of assumptions, finite element mesh restrictions, and other factors can be evaluated without incurring the difficulties of 3-D modeling approaches. These 2-D investigations will provide a foundational understanding that can be used to support the ultimate goal of 3-D modeling in Bison.

In addition to the 2-D investigations, a set of 3-D simulations were performed to: 1) support the 2-D modeling by evaluating out-of-plane stress conditions, 2) evaluate candidate approaches for representing discrete pellet cracks and MPS defects in three dimensions, and 3)

identify the areas of improvement needed in Bison or the MOOSE framework to reliably calculate localized PCMI that is as realistic as possible. The 3-D modeling activities were limited to a single pellet or short stack of pellets (3-5 pellets) to conserve computational resources and simplify the complexities of modeling full-length fuel rods in three dimensions.

3.1 Modeling Approach

A key goal in developing Bison is to model a fully coupled, 3-D pellet containing radial cracks and/or MPS defect, calculate stresses in the cladding, and ultimately incorporate a mechanistic stress corrosion cracking (SCC) model to determine the potential for cladding fracture. Achieving this goal requires developing a foundation from a 2-D planar approach and working towards 3-D geometric representation. Here, I first describe sensitivity studies conducted using 2-D R-Theta planar geometries of the pellet and cladding to understand the effect of the depth and frequency of discrete fuel pellet cracks on the localized cladding hoop stress. These studies evaluate different approaches to representing the stochastic nature of fuel cracks. The use of a 2-D geometric representation in the R-Theta plane circumvents the difficulties of solution convergence associated with 3-D contact of cracked bodies and allows for a large number of simulations under different conditions to improve understanding of the impact of geometric flaws on the localized stress and temperature distributions.

The R-Theta geometric models are based on an AP-1000 fuel rod design, for which a 70% reduction in the as fabricated gap size was used to simulate the pellet swelling and cladding creep down at a local burnup of about 20 GWd/tU. Furthermore, an initial fast fluence of 5e25 n/m^2 is applied to the cladding to account for the material property changes at this exposure. To evaluate the impact of discrete radial pellet cracks on the local clad hoop stress, we have used a quarter-symmetry, or 90 degree, model containing 2, 3, or 4 radial cracks with a crack length of 50% of the pellet radius, as shown in Figure 3-1 (a). A similar method was used to assess the role of the crack length on the maximum cladding hoop stress. The cracks in Figure 3-1 (a) are considered to be free surfaces. Treating them this way allows crack opening to occur during an increase in thermal gradient, or to relax while at constant power. This provides the basis for the cracks to impose shear stresses on the cladding during a power change. In order to evaluate the role of MPS defects on cladding failure during power operation, analysis of the MPS size and its impact on the clad hoop stress has been performed using a 180°, or one half symmetry, 2-D R-Theta model, which contains three discrete radial cracks and an MPS defect, as shown in Figure 3-1 (b).

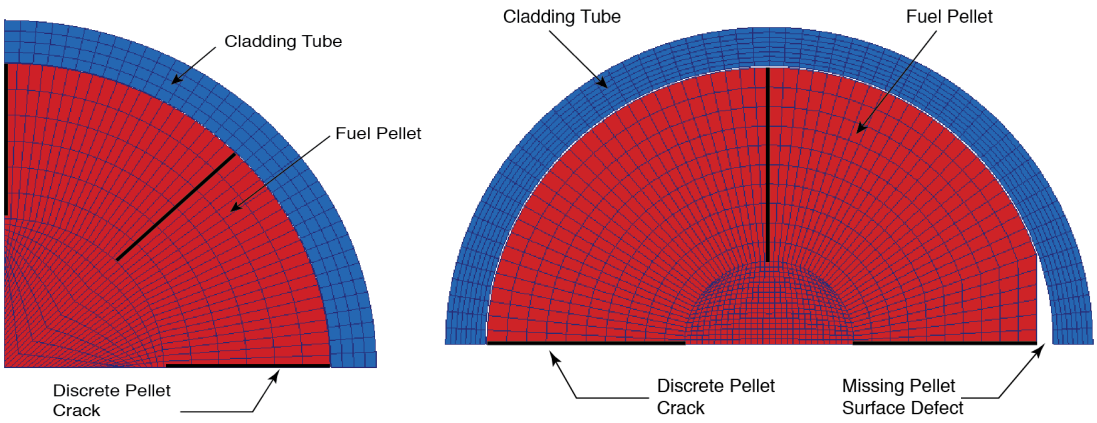

Figure 3-1. (a) 2-D, R-Theta model showing a representative three crack geometry (at 0, 45 and 90°, respectively) of radially orientation in the fuel pellet, and (b) geometric representation of an MPS defect in 2-D R-Theta space.

The 2-D simulations (in R-Theta) provide results needed to mechanistically model the geometric effects of pellet cracks and MPS defects. However, the 2-D simulations are only able to capture the planar affects of localized pellet defects, and are unable to capture the inherently 3-D aspects of MPS defects or pellet cracks. Such axial effects involve axial power variations as well as the hour glassing of the fuel pellet that cannot be captured in a 2-D R-Theta model. A similar methodology is used to evaluate classical PCI and the impact of an MPS defect on the clad hoop stress, with the exception that the MPS geometry is now a function of width and length, and the pellet cracks are assumed to run through the length of the pellet. Figure 3-2 (a) shows a $1/8^{th}$ 3-D geometric model for a single pellet containing three radial cracks surrounded by a concentric cylindrical cladding tube, and Figure 3-2 (b) shows a one-half (180º) 3-D geometric model of a five-pellet rodlet in which the center pellet contains an MPS defect. Furthermore, there are 2 radial cracks in the five-pellet model, which run along the symmetry plane.

The treatment of contact is a significant challenge. The Bison results presented here are primarily based on glued contact between the pellet and clad for both the 2-D and 3-D simulations. This simplification leads to higher than expected hoop stresses as a result of neglecting any slippage between the fuel pellet and cladding, which is discussed later in comparison to frictional contact modeling with various friction coefficients. Also for the 3-D MPS model, it is assumed that the five pellets are merged to prevent any asymmetric shifting of a pellet, which adds further complexities to the problem.

Figure 3-3 shows the power histories used within the calculations to evaluate the cladding hoop stress. The power histories are idealized cases similar to PWR ramp tests. Both power histories contain an initial ramp up to 25 kW/m over the course of 2.8 hours, with a 24-hour hold period. This is followed by a final, linear ramp up to full power over one hour, again followed by a 24-hour hold period. The final linear power for the low burnup rod is 40 kW/m, whereas for the higher burnup rod it is 32.8 kW/m.

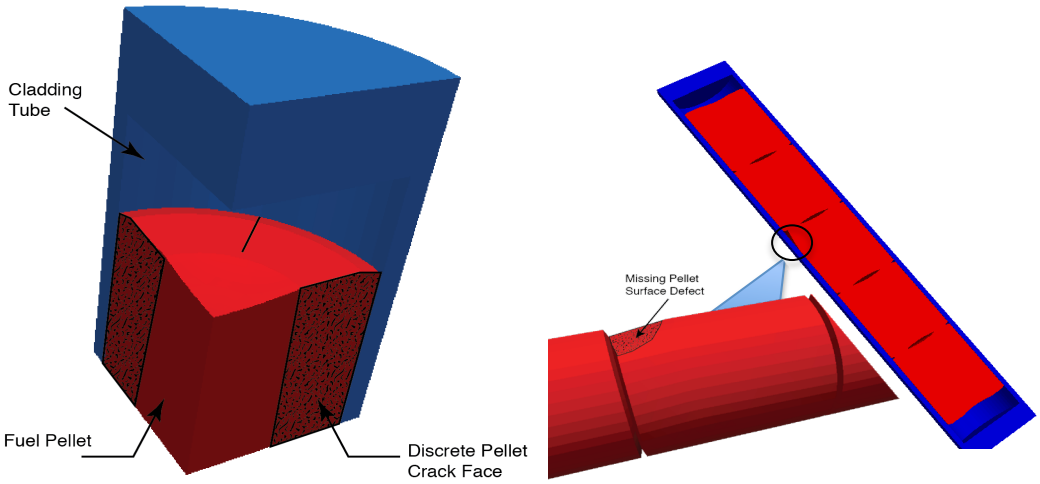

Figure 3-2. (a) 3-D geometric representation of a cracked pellet, and (b) 3-D geometric representation of a 5-pellet rodlet with the center pellet having an MPS defect.

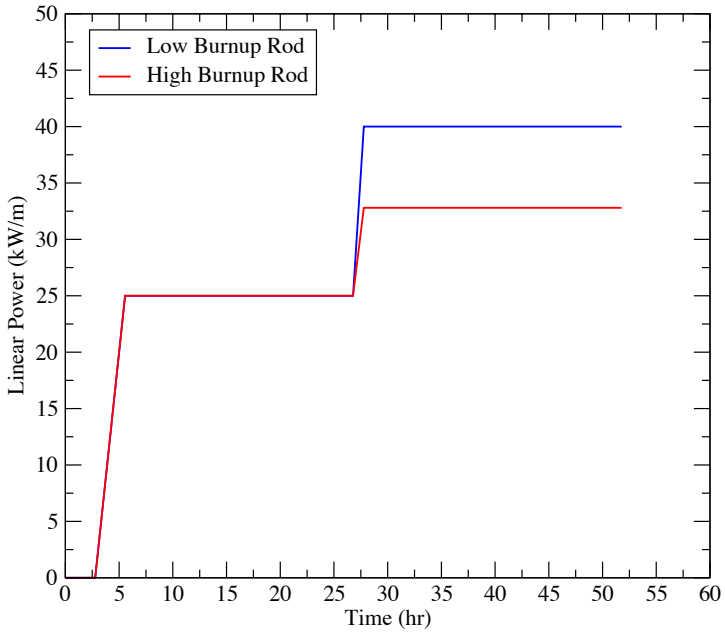

Figure 3-3. Power histories used to simulate the impact of discrete cracks and MPS on the local cladding hoop stress.

3.2 Bison Predictions of Idealized PCI Conditions

The assessment of the PCI capabilities consists of four major areas of investigation; 2-D modeling of fuel pellet cracks, 2-D modeling of MPS defects, 3-D modeling of fuel pellet cracks, and finally, 3-D modeling of MPS defects. The primary purpose of these activities is to establish the relationship between the different methods used to model the pellet and cladding geometry and the resulting localized cladding stress distribution and magnitude.

The important factors that were evaluated include the length and frequency of discrete pellet cracks, the dimensions (width, depth, and length) of the MPS defect, the modeling approach to pellet – clad contact and the friction coefficient between the pellet and cladding, and the role of the out-of-plane mechanical loading for the 2-D R-theta models. Each of these parameters is varied separately (and some cases together) to determine the impact on the maximum cladding stress, the stress distribution, and the local temperature perturbations. Appropriately representing these conditions as a function of irradiation effects and power history are fundamental to any methodology that will be used for PCI assessments. The use of more mechanistic material damage models will require, as a starting point, the local stress and temperature distributions in order to calculate material flow, chemical reactions, and fracture behavior.

3.2.1 2-D R-Theta Modeling of PCI Effects

The purpose of the 2-D geometric modeling is to evaluate the local cladding stress concentration under various idealized geometry conditions as a means to parameterize the influence of different modeling approaches. In contrast to 2-D axisymmetric R-Z models used to represent a full-length fuel rod, the 2-D planar models represent a small slice of a fuel rod. Symmetry in the R-Theta plane is imposed by using reflective boundary conditions. The out-of-plane conditions result in approximations to address the mechanical constraints in the axial direction and also leads to infinitely long geometric configurations. These approximations will influence the calculated deformations and temperatures and part of the assessment below will highlight these effects and indicate potential approaches to minimize their impact on PCI assessments.

3.2.1.A Fuel Crack Effects on Cladding Hoop Stress

Sensitivity studies have been performed to characterize the relationship between the size and angular spacing of discrete radial pellet cracks with the finite element mesh on the localized cladding stress distribution, using the 2-D R-Theta model shown in Figure 3-1 (a). First, the angular spacing of the pellet cracks was investigated. The 90° model was configured to have cracks at 0° and 90° (2 cracks); 0°, 45°, and 90° (3 cracks); and 0°, 30°, 60°, and 90° (4 cracks). In all three cases, the cracks extended to 50% of the pellet radius. Second, a R-theta model

containing three cracks (0°, 45° and 90°) was modified to evaluate crack lengths ranging from 20% to 70% of the pellet radius.

The simulations were performed using the low burnup power history shown in Figure 3-3 with a fast neutron fluence of $5x10^{25}$ n/m^2 on the cladding and a residual pellet-cladding gap of 25 microns. The maximum cladding hoop stress calculated as a function of the angular spacing between the cracks is shown in Figure 3-4. While the magnitude of the stress differs rather significantly, it can be argued that there is a trend towards saturating maximum cladding hoop stress with decreasing number of cracks in the clad (increased crack spacing).

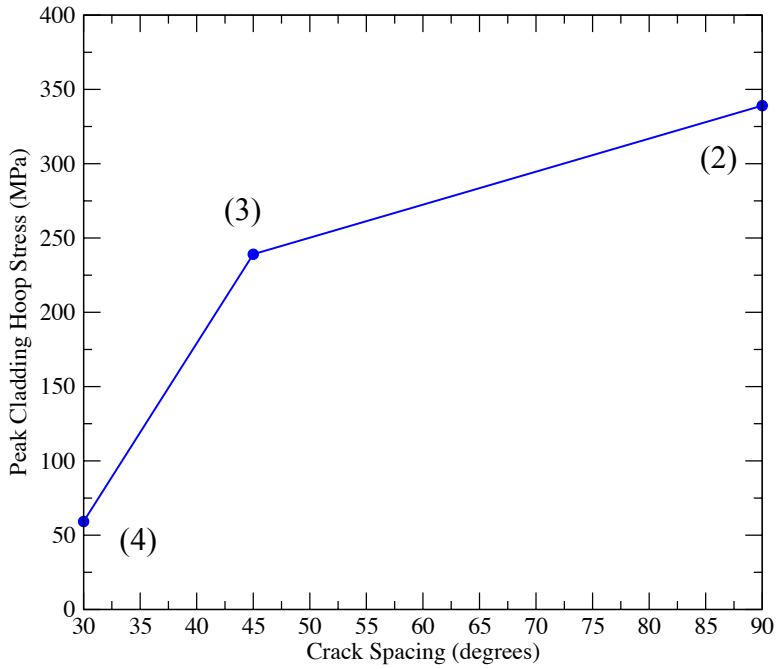

Figure 3-4. The maximum clad hoop stress calculated in a 2-D (R-Theta), 90 degree model as a function of the number of radial cracks. Values obtained by the Bison code. The number of explicit cracks in the model is shown in parenthesis.

The results of Figure 3-4 demonstrate that as the angular spacing between the cracks decreases, the maximum cladding hoop stress decreases as well. This trend is consistent with changes in the driving force responsible for the stress localization, i.e. the pellet crack opening displacements caused by thermal expansion. The high number of radial cracks present in the pellet reduces the crack opening displacement experienced by a single crack for a given amount of pellet thermal expansion, thus causing smaller shear forces at the pellet-cladding interface [44]. Due to the simulated geometry, the cases analyzed with Bison represent 4, 8, or 12 radial cracks per pellet. Typical cracking patterns observed in post-irradiation examinations of commercial LWR fuel find between 6 and 10 radial cracks per pellet, discussed by Oguma et al. [45]. Based on such post-irradiation examination (PIE) observations, the remainder of the Bison

evaluations presented in this chapter will focus on the 3-crack 90° model (equivalent to 8 radial cracks). Furthermore, this geometry of 3 cracks had the best quantitative agreement with the Falcon results of maximum clad stress.

Figure 3-5 displays the results of varying the radial crack length on the maximum cladding hoop stress distribution as well comparing the treatment of fuel – clad contact by using glued or frictional contact with a coefficient of friction of 0.5, as calculated in the 2-D (R-Theta), 90° model containing 3 cracks. The crack length was adjusted from 20% of the pellet radius to 70%. The results show that the maximum clad stress increases with increasing crack length, but trends towards saturation for crack lengths greater than 50% of the pellet radius. Increasing the crack length causes a decrease in the compliance of the fuel pellet, which allows the crack to open more during a power increase. With a larger crack opening displacement, there is a corresponding increase in the shear force transferred to the clad inner surface, thereby producing a larger clad hoop stress with increasing fuel crack length. Furthermore the use of glued contact between the fuel and the cladding prevents fuel slippage and, correspondingly results in predictions of increased cladding hoop stress. Both the glued and frictional contact implementations show very similar behavior in terms of the dependence of peak clad stress on crack length, just with an approximately 40-50% increase in stress magnitude for the glued contact.

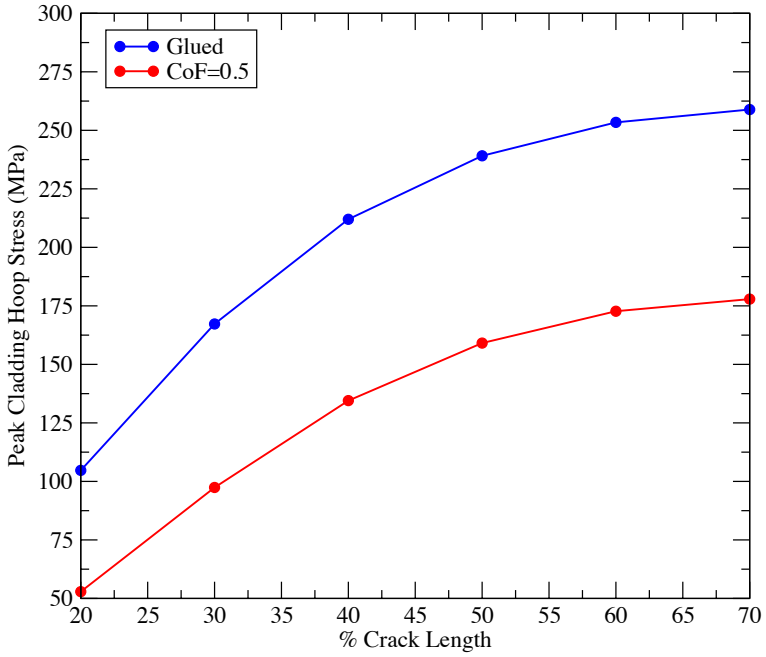

Figure 3-5. 2-D Bison R-Theta calculations of a 90-degree pellet containing 3 radial cracks showing the influence of crack length on the maximum clad hoop stress as well as frictional contact. The blue curve assumes glued contact and the red curve assumes frictional contact with a coefficient of friction (CoF) of 0.5.

The hoop stress contours within the cladding at the time of the maximum cladding stress (~30 hrs into the power history diagram shown in Figure 3-3) for the 30%, 50%, and 70% crack lengths are shown in Figure 3-6(a-c). These contours clearly indicate that the maximum hoop stress occurs at the position where the pellet crack impinges on the cladding. The magnitude of the stress intensity associated with the crack (e.g., maximum/minimum clad hoop stress) on the cladding inner surface displays a dependence on the crack length, varying from 2.2 in the case of the 30% crack to 2.7 in the case of the 70% crack.

The cladding hoop stress distributions and stress intensity are consistent with those calculated by Falcon and ALYCONE, which exhibit values ranging from 1.5 to 2.5 [5, 6-8]. Figure 3-6 shows the cladding stress concentration factor at the inner clad surface as a function of angular distance from the pellet crack location for the 70% crack length, as calculated by Bison and compared to Falcon calculation results reported by Lyon, et.al. [47]. The stress values have been normalized to the far-field stress to allow for a direct comparison between the results from Bison and Falcon. Excellent agreement is seen between the distributions. Again, it is possible that the more refined finite element mesh density used in these Bison calculations contributes to the higher values seen at the crack tip location.

High tensile hoop stresses are observed at the pellet crack tip for both the 30% and 50% cases. These results indicate that the cracks would most likely extend deeper into the pellet for the pellet stress conditions calculated, if the model were able to extend the crack length mesh. Correspondingly, a key observation from this assessment is that a 70% long radial crack appears appropriate for use in modeling discrete crack behavior using the 2-D modeling approach, this is seen from an increase in the crack tip hoop stress for the short crack lengths.

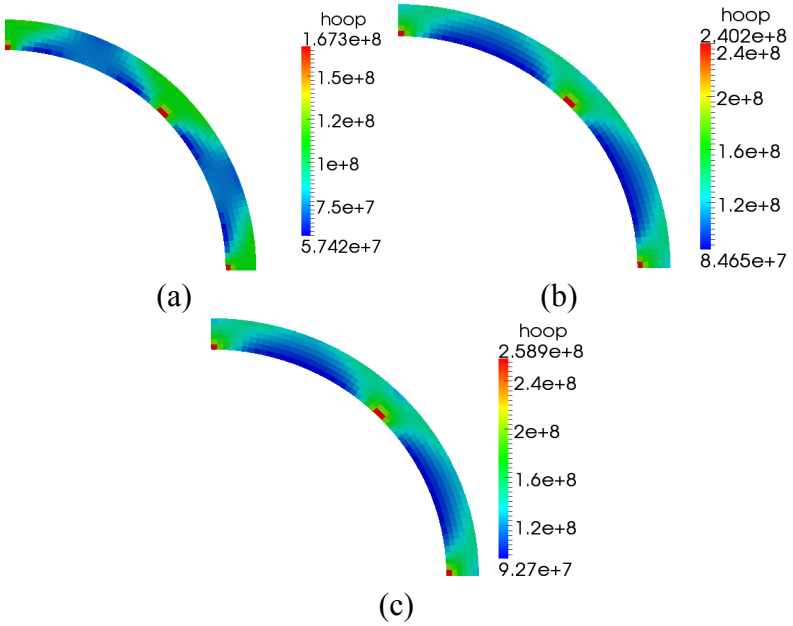

Figure 3-6. Hoop stress contour plot for; (a) 30% radial crack model, (b) 50% radial crack model, and (c) 70% radial crack model.

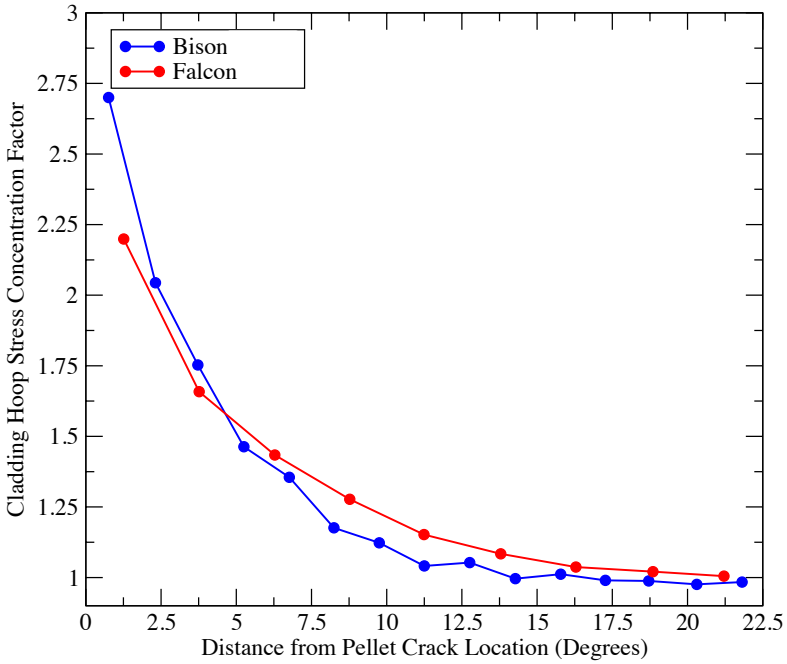

Figure 3-7. Clad hoop stress concentration factor as a function of the angular position from the fuel pellet crack location for a 70% long radial crack in a 2-D, R-Theta geometry. The results from Bison are shown in blue, whereas values calculated for Falcon are shown in red. The stress concentration factor is defined as the ratio of the local stress to the minimum value of the stress far away from the crack. The Falcon results have been reproduced from Ref. [47].

3.2.1.B MPS Defect Effects on Cladding Hoop Stress

The mechanisms driving the increase in cladding failure potential are similar for an MPS, but the path to cause failure is significantly different. As discussed above, pellet cracks open during a power increase and induce a shear stress in the cladding, which can lead to failure in classical PCI. However, with an MPS defect, the local cladding region adjacent to the MPS defect does not come into contact with the fuel pellet. Thus a maximum in the tensile hoop stress results from bending stresses in the regions surrounding the MPS defect. Further, local temperature perturbations due to reduced heat transfer across the larger gap volume impact both the maximum cladding hoop stress (higher fuel temperatures leading to greater thermal expansion) and the stress relaxation behavior (lower cladding temperatures).

Figure 3-1 shows a schematic of the 2-D planar R-Theta model used in Bison to calculate the complex thermal and mechanical conditions associated with the presence of an MPS defect. A 2-D, planar R-Theta model with 180° symmetry is used to represent the geometry of a pellet containing an MPS defect. Symmetry is imposed at the 0º and 180º positions and 3 pellet cracks are included at 0º, 90º and 180º positions and are represented by mechanically free surfaces extending 70% of the pellet radius.

Two different MPS defect geometries were included in this assessment: a flat-faced defect and a concave defect. PIE observations of MPS defects have found both types present in LWR fuel. The width of the MPS defect was varied from a small size of 45 mils (1.1 mm) to a large size of 150 mils (3.8 mm). These values span the range from below an acceptable MPS defect to the size observed to cause cladding failure.

Because of the 2-D representation, the length of the MPS defect is infinitely long (in the out-of-plane direction), which produces an exaggerated effect on the temperature and stress condition. The impact of a finite length MPS defect requires a 3-D model, as will be discussed later.

The MPS defect width or angle subtended by the missing circumferential surface affects the length of the unsupported cladding tube once contact occurs elsewhere along the interface. Both the width and the curvature also influence the distance between the pellet surface within the MPS defect and the cladding inner surface. This distance or gap has an important impact on the heat transfer from the pellet to the cladding, and results in a hotter region in the pellet adjacent to the MPS defect and a cooler cladding region. Examples of representative non-uniform temperature distributions are shown in Figure 3-8 (a) and (b) for the 45-mil and 150-mil flat MPS defect cases, respectively. In both of these simulations, the temperature distributions are shown at the time of the peak cladding stress, which occurred at a power level of 40 kW/m in Figure 3-8 (a) and 40 kW/m in Figure 3-8 (b).

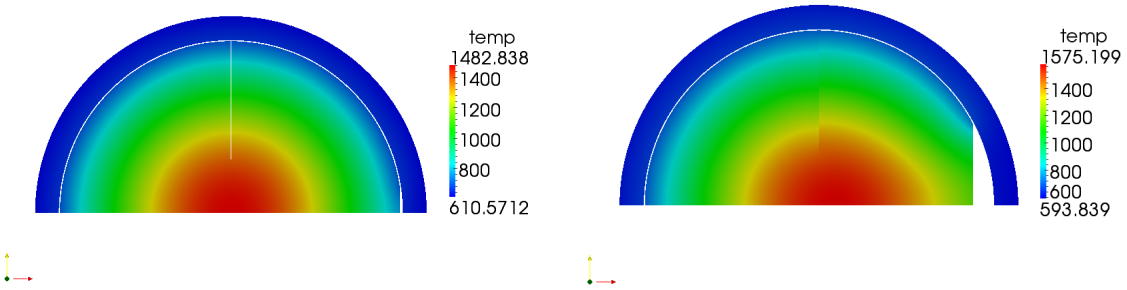

(a) (b)

Figure 3-8. Temperature Contour at Peak Cladding Stress Time for; (a) 45-mil Flat MPS Defect, and (b) 150-mil Flat MPS Defect.

The maximum cladding hoop stress and maximum fuel centerline temperature are shown in Figure 3-9 as a function of MPS width (represented by the subtended angle). The maximum cladding hoop stress increases as the width of the MPS defect increases. These results are consistent with the increase in the bending moment experienced in the cladding as the unsupported cladding length increases for larger MPS defects. An apparent saturation in this stress level is observed as the MPS size increases towards 50°. Several factors may be responsible for the saturation of the cladding hoop stress with large MPS defects, including

thermal creep within the fuel pellet and geometric effects associated with the unsupported cladding region.

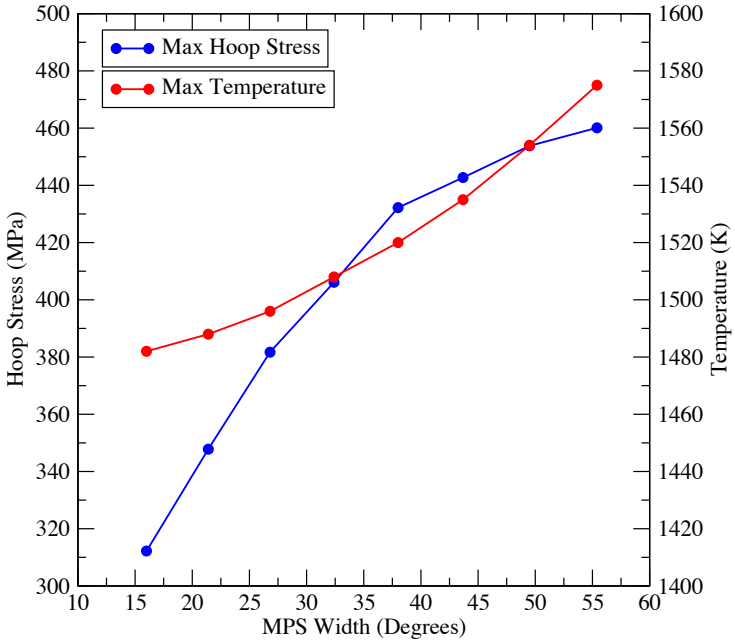

Figure 3-9. 2-D Bison calculations of a 180 degree pellet containing 3 radial cracks of 70% length, and a MPS, which shows the affect of increasing the MPS width on the maximum clad hoop stress (blue curve) and maximum fuel centerline temperature (red curve).

Montgomery and co-workers previously used Falcon to calculate the stress concentration in the cladding due to MPS defects [50]. In that work, the stress concentration factor was defined to be the ratio of the maximum cladding hoop stress for a given MPS defect divided by the maximum cladding hoop stress calculated for the same conditions of geometry, gap thickness and power history without an MPS defect. The Falcon results were provided to CASL for comparison to the results from Bison [50].

Following that approach, we have also calculated the 2-D MPS stress concentration factors using Bison for a flat MPS defect geometry, containing 3, 70% long pellet cracks in a 2D, R-Theta 180° geometry. Figure 13 shows a comparison of the Bison and Falcon 2-D stress concentration factors as a function of MPS defect size. The trend is consistent between the two codes, that is, as the MPS defect size increases, the stress concentration factor also increases. The most notable difference is the fact that for large MPS defects, the Bison results display a much stronger saturation behavior. Possible causes of this behavior could be the treatment of the out-of-plane (axial) mechanical boundary conditions, differences in the UO_2 thermal creep behavior, as well as differences between the geometric representation of the MPS used, Bison assumed a flat MPS where as Falcon assumed a concaved shape of the MPS. However, overall,

the results of the comparison of the calculated MPS stress concentration factor in 2D are quite consistent between the Bison and Falcon calculations.

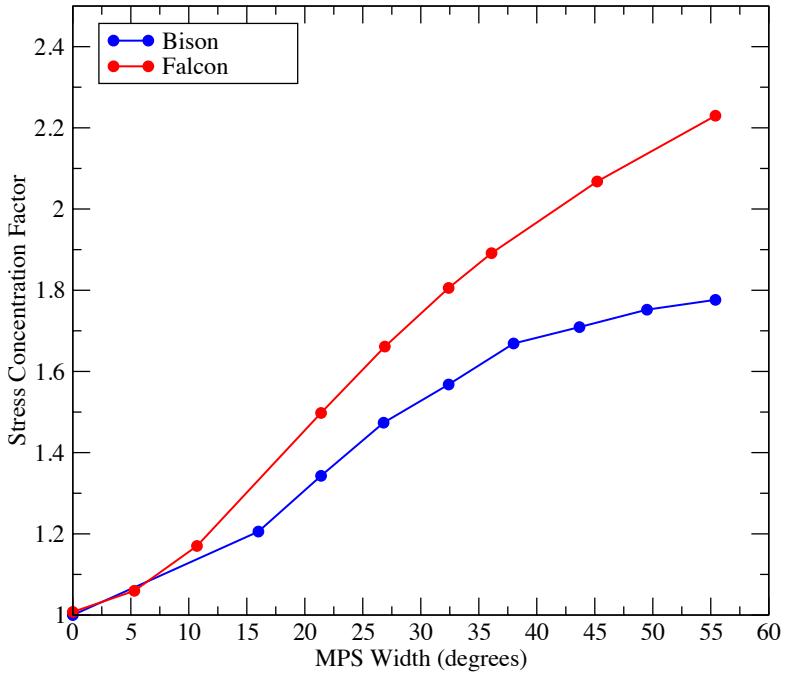

Figure 3-10. 2-D Stress concentration factor, as a function of MPS defect width compared to values from the literature [50].

However, there are quantitative differences between the calculated stress concentration factor using Falcon and Bison, as shown in Figure 3-10. A significant difference is the shape of the MPS simulated in the two models. As mentioned previously, Falcon assumed a concave-shaped MPS, while the Bison model used a flat MPS. A more significant factor is the use of a 22.5 deg. R-Theta model used to obtain Falcon results, which is no longer recommended by EPRI [43] The mechanical boundary conditions on the edge away from the MPS begin to influence results as the MSP size is increased. This issue is eliminated with a 90 deg. R-Theta MPS model. Figure 3-11 summarizes the results of Bison calculations that compare the impact of flat and concave MPS defects, as a function of MPS width. From Figure 3-11 (a), it can be seen that as the MPS defect width increases, the maximum cladding hoop stress increases, and corresponds to the increase in the maximum fuel temperature, as shown in Figure 3-11 (b). Both the bending moment due to the unsupported cladding tube and the large thermal expansion of the pellet are responsible for the increase in maximum hoop stress with increasing MPS size. The fuel temperature is also increased by the concave MPS defect geometry. These results clearly indicate that a curved MPS with concave geometry will produce both higher fuel centerline temperatures and larger maximum hoop stresses, for a fixed MPS size. This is consistent with the lower calculated stress concentration factor using Bison as compared to Falcon in Figure 1-10.

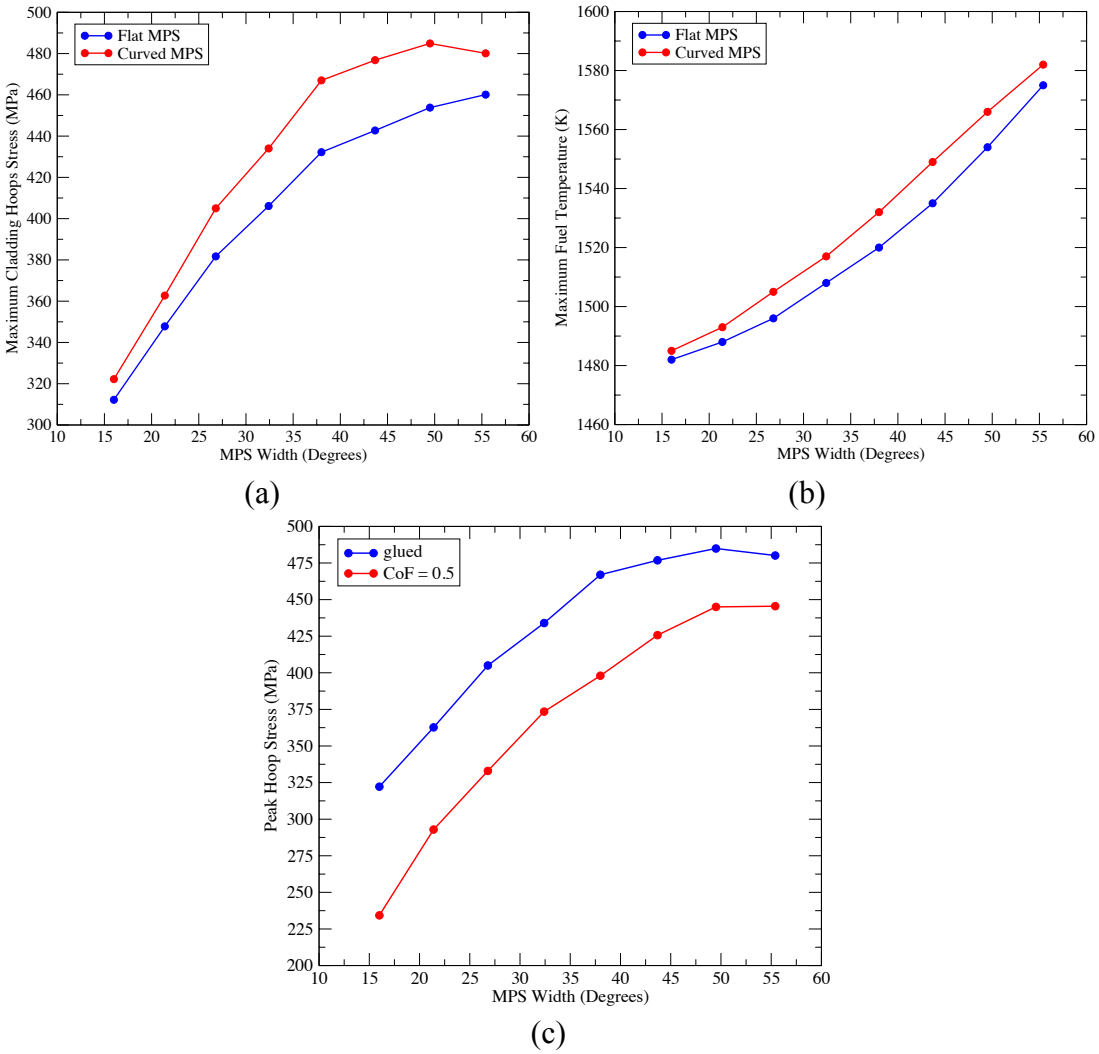

Figure 3-11. (a) Cladding Stresses Calculated by Bison for Various Size MPS Defects, (b) The Corresponding Maximum Temperature in the Fuel Pellet, and (c) Cladding Stresses Calculated by Bison for Various Size MPS Defects with glued and frictional contact.

The more realistic, concave geometry of the MPS and the use of frictional contact, as indicated in Figure 3-11 (a), (b), and (c) should improve the comparison of the Bison calculated results to those of Falcon, but that was not the only difference between the Bison and Falcon results shown in Figure 3-10. The geometric model used in the Falcon analysis considered a 22.5 degree model containing crack lengths of 50% of the fuel radius as well as frictional contact using a coefficient of friction of 0.5. Figure 3-12 summarizes a Bison comparison assuming a 90 degree model containing a concave MPS with two radial cracks of length 50% of the fuel radius, and switching to frictional contact with a coefficient of friction of 0.5. The comparison between Bison and Falcon is astoundingly good up to MPS widths of about 40%, however the assumptions used to obtain Falcon results introduce conservative inaccuracies. Within a 90

degree model, the symmetry dictates the presence of two MPS within the fuel pellet. This assumption of two MPS defects causes an increase in the maximum fuel temperature, which in turn increases the thermal expansion of the pellet, which gives rise to higher induced shear stresses in the cladding. Furthermore, Falcon assumes the crack lengths is 50% of the fuel radius. The Bison analysis indicates that for these conditions, the hoop stress at the crack tip is higher than the fracture stress of UO_2. This stress state should lead to elongation of the radial cracks. Correspondingly, longer cracks are needed to more accurately model the phenomenon of PCMI. However to get an accurate comparison to Falcon, Bison used a 90 degree model containing radial cracks 50% in length and a concaved MPS. The results of this one to one comparison can be seen in Figure 3-12. Bison and Falcon agree very well with each other but diverge when the MPS becomes significantly large. It is unclear what causes this divergence, but again the conditions assumed inherent in this 90° model are not entirely physical.

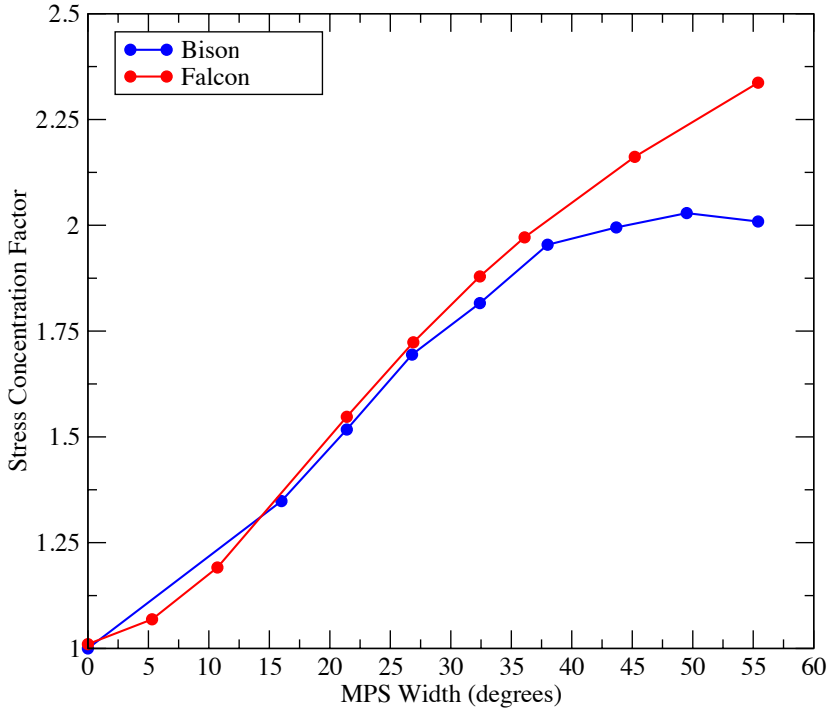

Figure 3-12. 2-D Stress concentration factor using the same geometric models, e.g. crack length, MPS shape, and 90 degree model, as a function of MPS defect width compared to values from the literature [51].

Another study was conducted to simulate a higher burnup rod. In this analysis, we have further reduced the pellet-clad gap for both the MPS models as well as the 70% pellet crack model, and lowered the power, corresponding to the high burnup power history seen in Figure 3-3. The gap was reduced from 25 microns to 20 microns, and the fluence was adjusted from 5e25 n/m^2 to 1e26 n/m^2 to account for the fluence acquired by a third cycle rod. Reducing the size of

the gap between the fuel pellet and clad, and lowering the peak linear power is consistent with the operating conditions of a third cycle rod. The purpose of this study is to analyze how these changes effect the stress values that in turn would change the 2-D stress concentration factor. The same methodology was used to determine the 2-D MPS stress concentration factors. Figure 3-13 shows the comparison between the lower burnup rod and the higher burnup rod. By running the same analysis, it is clear that the stress concentration is unaffected by these changes. This result points to a scaling relationship between the PCI stresses and the stresses induced by MPS. More simply stated, for the same gap size and power history, both a classical PCI and MPS simulation will provide a resultant stress concentration factor that is comparable.

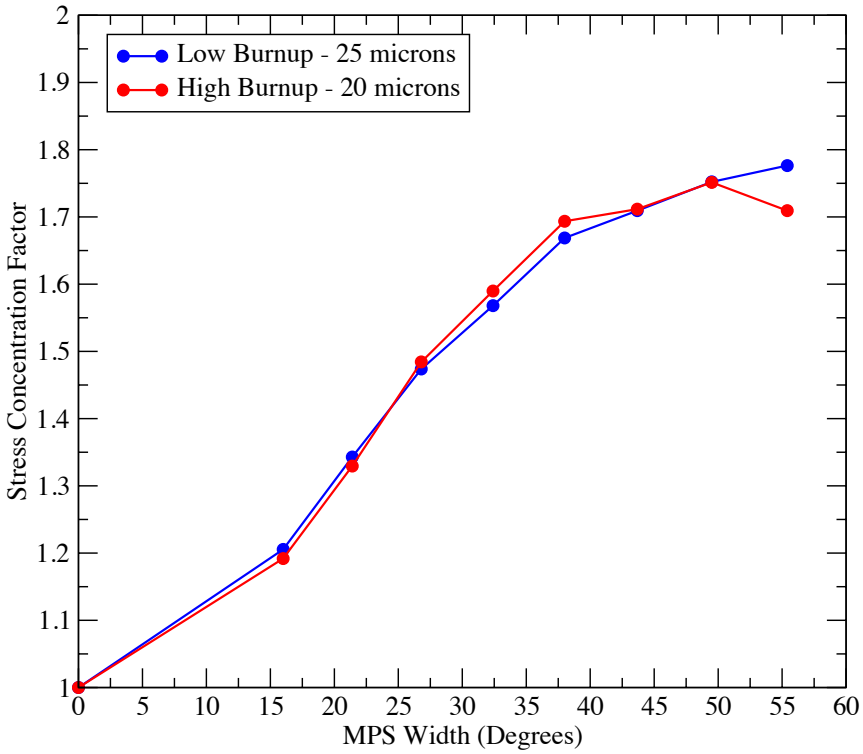

Figure 3-13. Comparison of 2-D Stress concentration factor for a low burnup rod and a high burnup rod, as a function of MPS defect width

3.2.2 3-D Five Pellet Model with MPS Defect

Modeling the geometric conditions of a MPS defect in 3-D requires multiple pellets to appropriately represent the mechanical boundary conditions. A finite element mesh was generated containing a stack of five (5) pellets within a cladding tube, where the central pellet contained an MPS defect extending partway down the length of the pellet, as shown in Figure 3-2. The model consisted of a 180° representation, with the symmetry plane passing through the

mid-line of the MPS defect. The symmetry planes were also configured to include a pellet crack that is 50% of the pellet radius (at 0° and 180° positions). Difficulties in the contact algorithm prevented the inclusion of pellet cracks at other locations (45°, 90°, or 135°) in this analysis. The model shown in Figure 3-2 contains a 105-mil wide by 105-mil long flat MPS defect. Table 3-1 lists the MPS defect sizes used in the assessment. A total of five MPS defects with flat surfaces of equal width and length dimensions (W/L = 1) were analyzed.

Figure 3-14 contains a comparison of the inner surface cladding hoop stress as a function of time for the 2-D and 3-D models containing an MPS defect with a width of 105 mils. The data from the 3-D location was taken from the location at the half-length and half-width of the MPS. The 2-D results, shown in blue, exhibit a higher clad stress as compared to the 3-D results. The largest contribution to the difference between the 2-D and 3-D results is the fact that the 2-D model represents the MPS defect as infinitely long with a finite width, whereas the 3-D model explicitly includes the MPS defect with a finite length and width. The finite length of the MPS reduces the bending forces by providing additional support in the axial direction that is not included in the 2-D model.

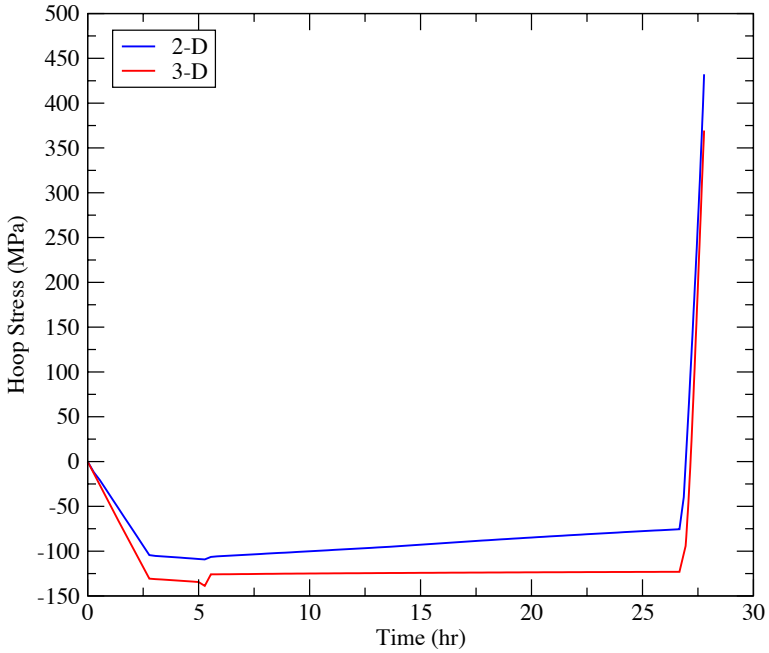

Figure 3-14. Comparison of the hoop stress calculations a 2-D R-Theta 180 degree model MPS with a width of 105 mil (blue line) to a 3-D 180-degree model containing a MPS of width 105 mils and length of 105 mils (red line).

Figure 3-15 (a-c) displays the temperature distribution in the fuel pellet, the temperature distribution in the cladding and the inner cladding surface hoop stress contour, respectively, for the 5-pellet 3-D model containing a 105 x 105 square-mil MPS defect at a time corresponding to

the maximum hoop stress. These results illustrate the complex effects caused by the MPS defect, such as cold spots in the cladding, hoop stress concentrations and hot spots in the fuel. The pellet-pellet interface and the MPS defect location are easily discernable from the contour plots.

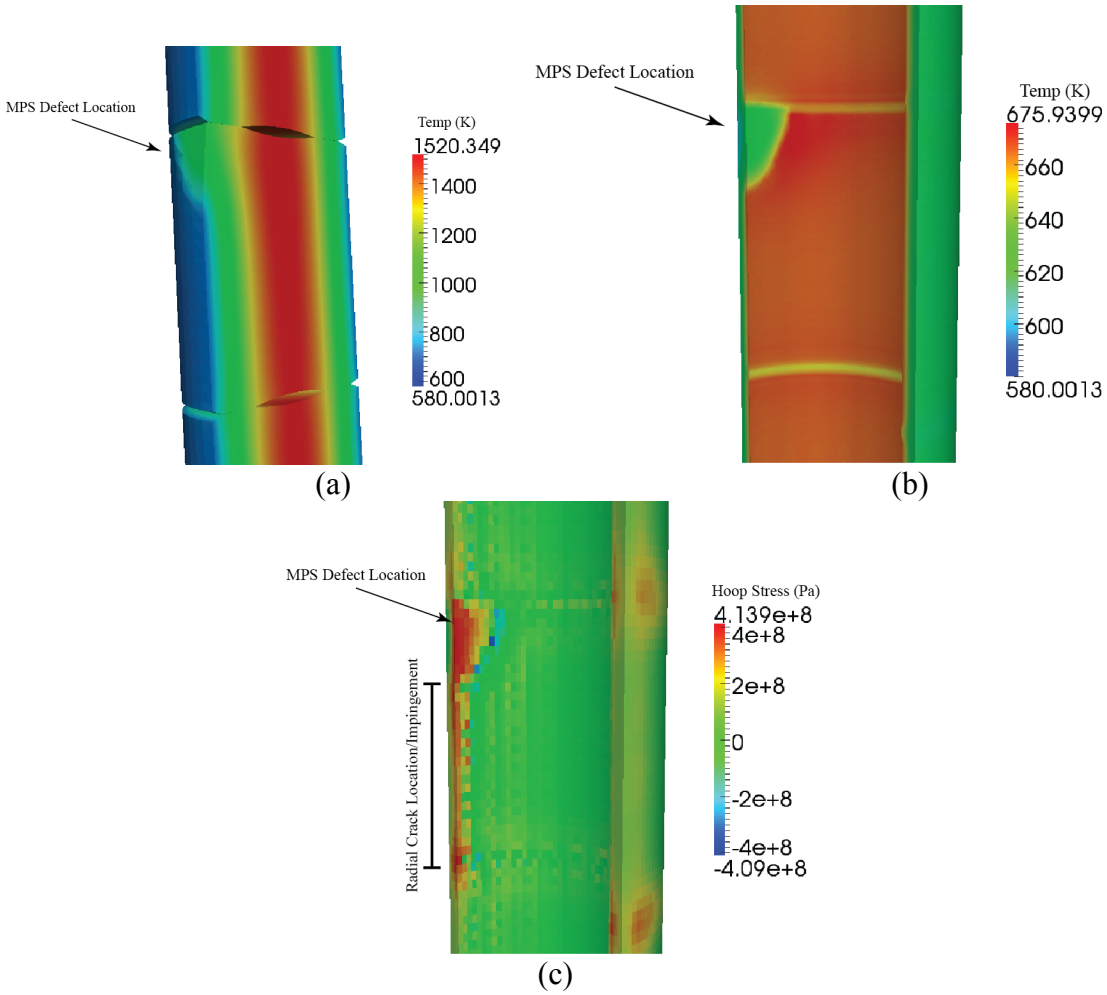

Figure 3-15. (a) Pellet temperature distribution in the vicinity of the MPS defect, (b) Inner cladding surface temperature distribution in the vicinity of the MPS defect, and (c) Inner cladding surface hoop stress distribution in the vicinity of the MPS defect.

Previous experience with structural analysis assessments [9,11] have shown that the hoop stress should increase as a function of the MPS volume increases. Table 1 lists the maximum cladding hoop stress calculated for different MPS defect sizes, all of which were modeled with a width to length ratio (W/L) equal to unity. The maximum cladding hoop stress calculated by Bison increases with larger MPS defects, similar to that observed from the 2-D MPS defect stress results. Furthermore, the cladding stresses calculated with the 3-D model are 7-16% lower than those from the 2-D model, which again presumably result from the finite axial length. This is

shown by the ratio of 3-D to 2-D maximum stress values in Table 1. The comparison of the 3-D and 2-D stress calculations highlights the inherent 3-D effects of an MPS defect on the cladding stress state. The results obtained by Montgomery and co-workers [50] using the ABAQUS general-purpose structural analysis code are shown in Table 3-1 for comparison. Excellent agreement is found for the geometric effect on the maximum cladding hoop stress for a finite length MPS defect between Bison and ABAQUS.

Table 3-1. 3-D Bison maximum hoop stress calculations as a function of MPS defect width, with a W/L = 1, and ratio of the maximum 3-D hoop stress to the maximum 2-D hoop stress.

MPS Defect Width (mils)	Max Hoop Stress (MPa)	Bison $\sigma_{3\text{-}D}/\sigma_{2\text{-}D}$	EPRI/ABAQUS $\sigma_{3\text{-}D}/\sigma_{2\text{-}D}$
45	311	1	0.94
60	348	1	0.92
75	357	0.93	0.89
90	362	0.89	0.88
105	369	0.85	0.86
120	375	0.84	0.84
135	387	0.85	N/A
150	406	0.88	N/A

Calculating stresses induced by a finite dimension MPS defects is an important step in developing a methodology to model cladding failure using fuel behavior modeling. One approach is to use 2-D fuel performance codes like Falcon or RODEX-4 and then apply stress intensification factors determined from a structural mechanics analysis. This approach has been used by EPRI and AREVA to estimate the maximum cladding stress using classical PCI stress analysis methods and then applying MPS defect stress concentration factors as a function of MPS defect size [50, 52]. Figure 3-16 compares the 3-D stress concentration factors from the Falcon/ABAQUS calculations performed by EPRI and the ANSYS calculations performed by AREVA with those obtained from this Bison analysis using the 3-D 5-pellet model. This comparison demonstrates good consistency in capturing the MPS defect size effect on the stress concentration factor. Noticeable differences are seen between the absolute values of the stress concentration factors, however. These differences are most likely related to the approaches used in the stress analysis of fuel pellet cracks, which form the basis for the classical PCI methods used in Falcon and RODEX-4.

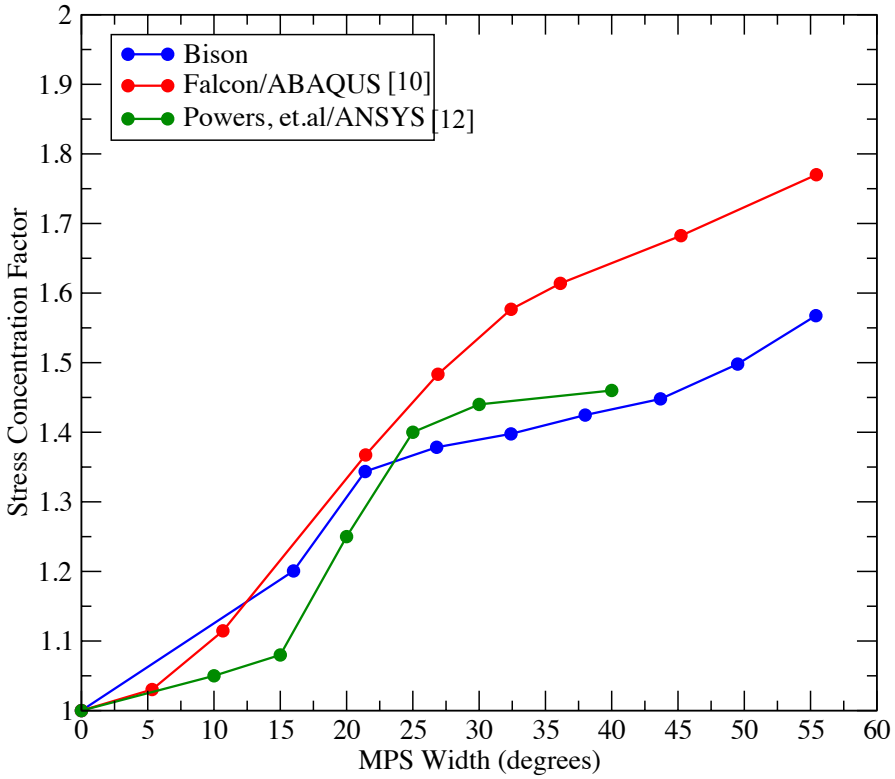

Figure 3-16. 3-D Bison stress concentration factor, as a function of MPS defect width, compared to values from literature [51,53].

3.3 Summary and Conclusions

The results of this assessment have demonstrated that the pellet cladding mechanical interaction (PCMI) 2-D and 3-D modeling capabilities in Bison are consistent with PCI modeling approaches used by EPRI in the Falcon fuel behavior code [43, 44] and CEA with the ALCYONE code [54]. By representing idealized cracked or defected pellet geometries using 2-D and 3-D finite element meshes, Bison is able to calculate the local stress distributions at the clad inner surface that are important for determining the initiation and propagation of stress corrosion cracks. This preliminary work on modeling fuel cracks and MPS in a full 3-D representation finds that 3-D geometric effects should be considered for mechanistic evaluations of PCI failure with MPS defects.

The Bison and Falcon 2-D stress concentration factors as a function of MPS defect size were compared and the trend is consistent between the two codes; namely, that as the MPS defect size increases, the stress concentration factor also increases. The most notable difference between the two codes is for large MPS defects, in which the Bison results display a much stronger saturation behavior. Possible causes of this behavior could be the treatment of out-of-plane (axial for 2-D R-Theta) mechanical boundary conditions and differences in the UO_2 thermal creep models. However, the consistency in the behavior of the 2-D results between

Bison and Falcon demonstrates that the CASL development efforts are progressing in the right direction.

The comparison of the 3-D cladding stress calculations with those obtained by others show excellent agreement for the geometric effect on the maximum cladding hoop stress for a finite length MPS defect. Stress reduction factors of 7 to 16% for finite length MPS defect were calculated by Bison using a 5-pellet model, which agreed closely with those calculated by EPRI using ABAQUS. When applying these factors to the 2-D stress calculations, the Bison results correlate closely with those published by AREVA and are lower than those reported by EPRI.

Chapter 4: PCI Failure Analysis

The objective of developing an advanced, 3-D fuel performance modeling capability to assess PCI is to: 1) reliably calculate the cladding failure potential related to PCI; 2) define the impact of manufacturing flaws along with the material properties on failure probability; and 3) to evaluate the role of plant operating strategies as well as specific fuel designs on the PCI failure potential. To meet these objectives, it is imperative to develop a high-fidelity, fully coupled computer code that incorporates important plant operating procedures, e.g. power ramp rate and axial power shapes related to fuel performance, as well as considering the inherently coupled intricacies that occur in irradiated fuel behavior during normal and transient operations. By developing and employing a advanced fully coupled multi-physics and multi-dimension fuel performance code and developing mechanistic or physics based material models, efforts can be taken to reduce the uncertainties surrounding existing PCI failure methods. The approach to address the current uncertainties in PCI failure probabilities will allow for improved fuel utilization and increase the plant operating flexibility.

The focus of this chapter is to assess the capability of BISON as a 3-D fuel performance code to represent the underlining mechanisms controlling the failure of the cladding as a result of PCI, and in particular PCI driven by MPS, as compared to actual commercial nuclear power plant data. As mentioned in Chapter 1, the processes leading to cladding crack initiation and propagation begins with the presence of localized stress and strains in concert with available corrosive fission products. PCI fuel behavior modeling must be built upon a methodology that can reliably and consistently calculate the local stress conditions as a function of prior irradiation history, material properties, and local power conditions. This means capturing the effects of geometric irregularities (i.e. pellet cracks), permanent changes in dimensions of the pellet and cladding caused by fission product swelling and irradiation-induced cladding creep, as well as, thermal, mechanical, and chemical interactions between the pellet and cladding, i.e. frictional forces, heat transfer, and chemical bonding.

In the late 1970s PCI related failures caused the implementation of startup ramp restrictions. These ramp restrictions where intended to reduce the stresses caused by pellet cladding contact[64,74]. These ramp restrictions had a significant impact on Westinghouse fueled PWRs, reducing PCI related failure until 2003. The recent failed fuel rods were integral fuel burnable absorber (IFBA) fuel rods using Zirlo cladding[64]. Following an investigation into the power distribution it was determined the failed rods where subject to significant local power increases. The conclusion pointed to PCI related failure, however many other non-failed rods experienced similar local power changes[74]. Reviewing the 1970s ramp rate restrictions, it was determined the imposed ramp rate restrictions where sufficient to prevent PCI related failure. Following the root cause analysis many of the fuel rods where take to hot cells for further inspections. Figure 4-1(a-b) shows detail images from the hotcell inspections.

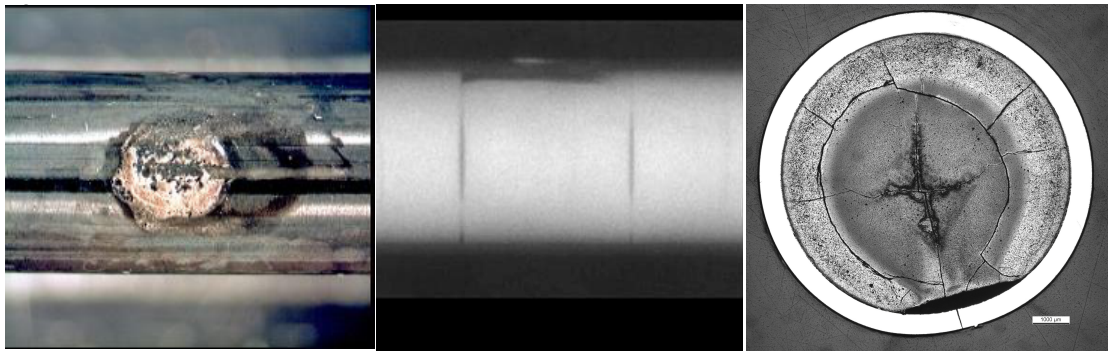

(a) (b) (c)

Figure 4-1.(a) External view of cladding failure, (b) Neutron radiograph showing the presence of a MPS, and (c) Cross-sectional image show the MPS is the root cause of the failure of rod M16S_O05 [74]

The objective of this dissertation is to develop a methodology to determine rod failure, and then to utilize the resulting failure criteria to evaluate specific historical MPS and PCI failures, shown in Figure 4-1, a sensitivity study to better understand the safety margins against PCI failure for various reactor power operations and MPS geometries. There are a variety of experimental and analytical methods that have been used over the years to predict cladding failures during power maneuvers in commercial power plants. The proliferation of these methods has been fueled by the need to assess fuel-rod design limitations or new plant operational procedures to limit or eliminate PCI fuel rod failures induced by SCC of the cladding. Early methods, mostly empirically based, proposed to avoid PCI failures by imposing power maneuver restrictions combined with fuel rod conditioning procedures. Those approaches later proved to be unreliable. This is because the approach had an inadequate technical basis, which has resulted in imposing overly restrictive constraints on plant operation in some cases. There are two primary approaches for assessing and limiting the potential of cladding failure by PCI. The first is to develop a correlation for a threshold stress that should not be exceeded during a power maneuver, and the second is to utilize a more mechanistic approach in which detailed analysis of local effects that contribute to PCI induced stresses is combined with an SCC based cumulative damage failure model.

The assessment we perform within this chapter is summarized in Figure 4-2. The fuel rod analysis effort consists of four main steps that together are used to identify the effect of power operation on the PCI behavior of irradiated fuel. The first step consist of a steady state R-Z depletion analysis of the highest duty fuel, or the limiting rod, one with a known failure, is performed to establish the fuel rod conditions, e.g. pellet-cladding gap, plenum pressure, and released fission gas, following the first cycle of operation. The results of the steady state R-Z analysis provides the initial fuel rod conditions used in the third and fourth steps, which consist of analyzing the startup power ramp or a mid cycle power maneuver. The second step of the analysis consists of a full length R-Z analysis of the startup ramp. The purpose is to locate the region in the cladding were the maximum hoop stress is identified, using the R-Z power ramp analysis. Also the maximum hoop stress is generally located where the residual pellet-cladding

gap is the smallest, e.g. gap at zero power.

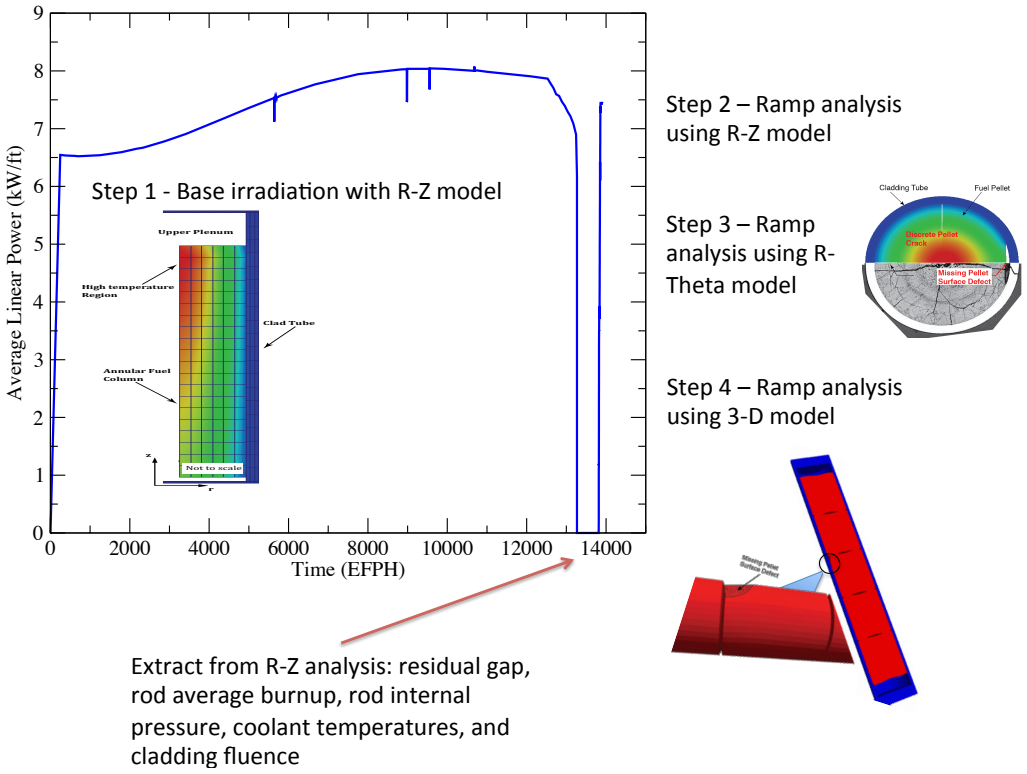

Figure 4-2. Workflow used in the assessment of PCI failures for a commercial nuclear power plant, as well as assessing failure criteria by comparing to test reactor power ramp data.

In the third step, the local cladding stresses and PCI damage index response are calculated using the R-θ local effects model at the peak stress location. This will be a specific PCI scenario and will be treated similar to the ramp test validation cases. However, these rod failures where contributed to PCI failure from a MPS. In the EPRI report [54] that analyzed PCI failures contributed to PCI, they assumed a single MPS size and did not consider the various sizes of MPS, as will be done here. Extending their analysis, we will investigate the impact of various MPS widths in addition to performing an evaluation of the impact of 3-D, length and width dependent MPS geometry. Similar to the third step, step four will evaluate the 3-D geometric effects on the local stress concentration, PCI damage index response, as well as critical strain energy density, and evaluate the failure potential for each rod in the assembly.

The purpose of the 3-D analysis will be to determine what the critical length and width of MPS will lead to a through wall failure. Along with studying the varying width and length effects of the MPS, an evaluation will be performed to assess the impact of ramp time on the three failure criteria. The purpose of this study will determine how the time it takes to reach full power affects the stress in the cladding along with how conditioning of the rod will assist in

reducing the stress contributed to PCI.

4.1 Bison Modeling of Ramp Failure Tests

4.1.A Approach

The objective of the current effort has been to develop a fuel performance modeling methodology to calculate, using commercial data, when and where a fuel rod failure will occur. However, before this goal can be achieved, we must first develop some confidence in an appropriate metric for failure analysis based on comparisons to ramp test data performed in test reactors. The test rods chosen for this assessment were obtained from a number of experimental ramp test programs that utilized irradiated commercial PWR rods to conduct rod failure experiments following a significant power maneuver. These included the Studsvik Over Ramp, Super Ramp, and Trans Ramp IV programs [55-57], as well as, rods from a CEA/OSIRIS ramp test program [58]. The data for these tests were extracted from the IFPE, the OECD/NEA International Fuel Performance Experiments database [55-57,59]. Detailed information on these test programs is available in the project reports that are also contained in the IFPE [55-57,59]. The goal of this work is to demonstrate the methodology for 3-D PCI analysis, as discussed above, and determine the differentiation between failed and non-failed rods, the test inventory included rods that failed during ramp testing as well as those that survived. A list of all the experimental ramp test rods used in the current assessment is shown in Table 4-2.

Table 4-1. PCI Ramp Test Rod Database for Failed and Non-Failed Fuel Rods [66-68].

Ramp Test Experiment	Burnup (MWd/tU)	Failed Rods	Non-Failed Rods	P_{cond} (kW/m)	P_{max} (kW/m)
RISO FGP3	42-43	0	2	25-29	39-40
SuperRamp	35-45	5	10	25	35-49
TransRamp II	31	3	3	20	42-60
TransRamp IV	23-29	5	2	25	43-45
OverRamp	16-23	7	8	30	37-45
Osiris	23-25	0	2	21-24	39-43

P_{con} – Ramp Conditioning Power
P_{max} – Ramp Terminal Power

The ramp tests conducted for each of these cases followed a similar approach. After base irradiation in a commercial PWR, the rods were examined to measure cladding diametral deformation and then refabricated for use in the ramp tests. The ramp tests were conducted in

test reactors by first conditioning the rods at a moderate power level (20 to 30 kW/m) for hold periods of typically 24 hours. A power ramp was then initiated at a prescribed ramp rate to a final P_{max}. The power was then held at the peak ramp power level for a period of time or until rod failure was detected, depending upon the goal of the particular test. Post-ramp PIE of the rods typically included rod length, profilometry, and fission gas release measurements, as well as visual inspections and neutron radiography. Destructive examinations were also often conducted to provide detailed information on the nature and location of the fuel rod failures experienced in the tests. However, the majority of the ramp test do not contribute rod failure to MPS but do contribute it to classical PCI. Data from these examinations are available in the IFPE [55-57,59]. Figure 4-3 illustrates the typical ramp test power history used in the majority of these tests.

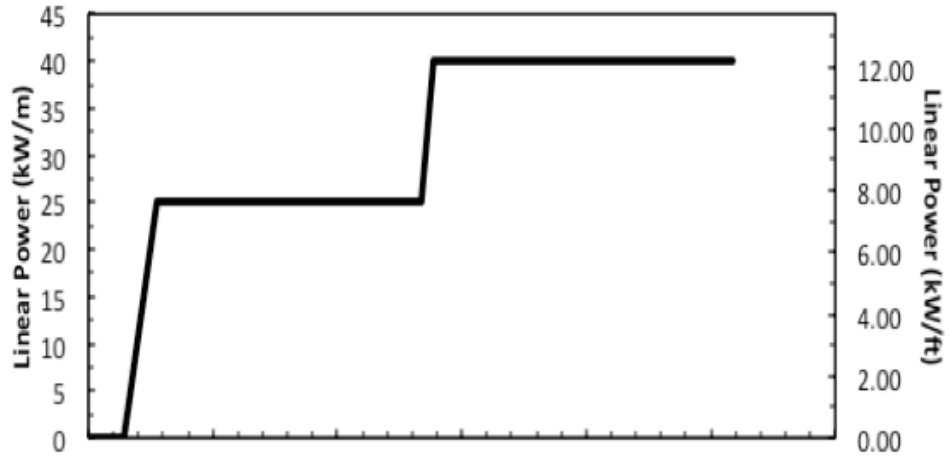

Figure 4-3. Typical ramp test power history, beginning with a conditioning power (P_{con}) and ending with a ramp to terminal power (P_{max}).

4.1.B Results

Each of the experiments listed in Table 1 contain a number of rods for analysis. However, due to time constraints, only a few select fuel rods have been analyzed to date. The rods that were chosen came from the OverRamp experiment [56]. The results of these simulations were compiled and compared to previously reported results available in the literature [59-60], where applicable. For example, comparisons were made to available cladding creep down post-irradiated examination (PIE) data.

Comparisons to available PIE data provided a metric to establish the accuracy of the BISON calculations for the base irradiation. Key to performing the PCI analyses is the proper determination of the fuel-cladding gap prior to the ramp test. The accuracy of this parameter is an indicator of the accuracy of the base irradiation modeling and is required to properly set the initial conditions used during the subsequent modeling of the power ramp to accurately reflect the conditions in the experiment. The two parameters that determine fuel-cladding gap are fuel

radial expansion and cladding creep down. Unfortunately, there are no measured values for fuel-cladding gap or fuel radial expansion, but there are experimental determinations of cladding creep down available.

Table 4-2 shows four different methods used to apply plenum and coolant pressure to the surface of the cladding. The table then compares the resultant cladding creep down values to the experimentally measure values. This sensitivity study shows the current capabilities in BISON-CASL. It was important to understand how applying the pressure boundary conditions would affect the resultant cladding creep down. Currently, BISON does not have the capability to model a plenum spring. The purpose of the plenum spring is to minimize the mobility of the fuel, but also exerts an axial force on the cladding as well. This axial force opposes the pressure seen from the coolant, more or less canceling it out. For this reason method 2 seemed the most appropriate pressure boundary condition. Method 2 assumes the plenum pressure and plenum spring cancel out the coolant pressure on the top and bottom of the cladding. This assumption results in the plenum pressure being applied to the inner tube surface of the cladding, and the coolant pressure being applied to the outer tube surface of the cladding.

Table 4-2. Pressure boundary condition sensitivity study, comparing different plenum and coolant pressure boundary conditions to the experimentally measured cladding creep down values.

	W4-1	W4-2	W5-4	W5-5	W5-6
Experiment	16.5	18	21.5	28.5	28
Method 1	13.19	13.45	17.01	19.62	27.05
Method 2	20.43	21.78	23.3	26.69	27.56
Method 3	17.74	23.02	24	27.91	28.26
Method 4	12.14	16.42	18.33	21.2	21.2

Method 1 – Applied coolant pressure to top, outer surface, and bottom of clad. Applied plenum pressure to inner surface of the clad.

Method 2– Applied coolant pressure to outer surface of clad. Applied plenum pressure to inner surface of clad. No pressures where applied to the top and bottom of the clad.

Method 3 - Applied coolant pressure to outer surface of clad. Applied plenum pressure to top, inner, and bottom surface of the clad.

Method 4 - Applied coolant pressure to top, outer surface, and bottom of clad. Applied plenum pressure to top, inner, and bottom surface of the clad.

Other sensitivity studies were conducted, such as relocation activation energies, relocation stop parameter, fuel creep, and fuel densification parameter. The relocation activation energy determines the linear power for fuel relocation to occur, and relocation stop determines

the rod average burnup at which fuel relocation is no longer allowed to occur. BISON is currently implementing a smeared cracking model, which allows the fuel to crack and expand when stresses are high enough. Without a smeared cracking model, stresses in the fuel will increase until fuel creep occurs. As the fuel creep occurs it softens the compliance of the fuel as well as reduces the fuel's radial expansion. By reducing the fuels ability to radially expand, this causes the residual gap to be much larger than expected. Based on those results, it was determined that fuel creep should not be included in the modeling. However with fuel creep turned off, BISON then over-predicts the fuel radial expansion. This contributed to the fuel densification parameter being too low. The fuel used during the OverRamp experiment was an older fuel design and was considerably less stable than modern fuels. The stability is a contributing factor to how much irradiation-induced densification can occur. With the OverRamp fuel being older fuel, it was determined that 1% fuel densification is a reasonable amount of irradiation-induced densification. Below is a brief summary of the boundary conditions, models, and parameters used, and Table 4-3 summarizes the final results following the base irradiation.

R-Z Problem Set Up

- Coolant and Plenum Pressures
  - Pressures are only applied to cladding inner and outer tube surfaces
- ESCORE Relocation Model
  - Activation = 5 kW/ft
  - Stop = Rod average burnup at the end of the base irradiation
- Fuel Creep
  - Turned off, Bison does not currently have reliable smeared crack model
- Fuel Densification
  - 1%, Ramp test used older fuel which is unstable allowing for more densification to occur

Before a PCI ramp analysis can be done to assess the appropriate fuel rod failure criteria, a sensitivity study of the mechanical contact between the fuel and clad needed to be conducted. This study looked at how changing the coefficient of friction (CoF) between the fuel and clad would affect hoop stress on the inner surface of the cladding. Once the gap closes and a power transient occurs the fuel's radial cracks begin to open and slide across the claddings inner surface. The fuel resistance to sliding causes a concentration of tangential stresses to build on the claddings inner surface. The CoF allows for the fuel to gain more traction on the claddings surface, which results in an increase in the hoop stress. Figure 4-4 shows the relationship between cladding hoop stress and CoF. As seen in Figure 4-4, an increase in the CoF produces a corresponding significant increase in the peak hoop stress. Furthermore, the expectation is as the CoF extends past a value of 1 to infinity (shown on the plot as CoF=2), the peak hoop stress will begin to converge toward the value obtained when modeling the contact as glued, which is shown as a red circle in Figure 4-4.

Table 4-3. Dimensional Changes Following the R-Z Base Irradiation.

	W4-1 (F)	W4-2 (NF)	W5-4 (NF)	W5-5 (NF)	W5-6 (F)
Rod Avg Burnup (MWd/tU)	19.02	19.07	15.25	20.7	20.7
Exp Clad Creep Down (microns)	16.5	18	21.5	28.5	28
Sim Clad Creep Down (microns)	20.43	21.78	23.3	26.69	27.56
Fuel Radial Disp (microns)	33.45	33.42	23.11	35.64	35.44
Gap Thickness (microns)	28.62	27.78	36.09	19.88	19.5
Fast Fluence*e25 (n/m^2)	1.85	1.97	1.67	2.07	2.11
Plenum Pressure (MPa)	3.17	3.25	1.73	1.78	1.61

F – Rod that failed

NF – Rod that did not fail

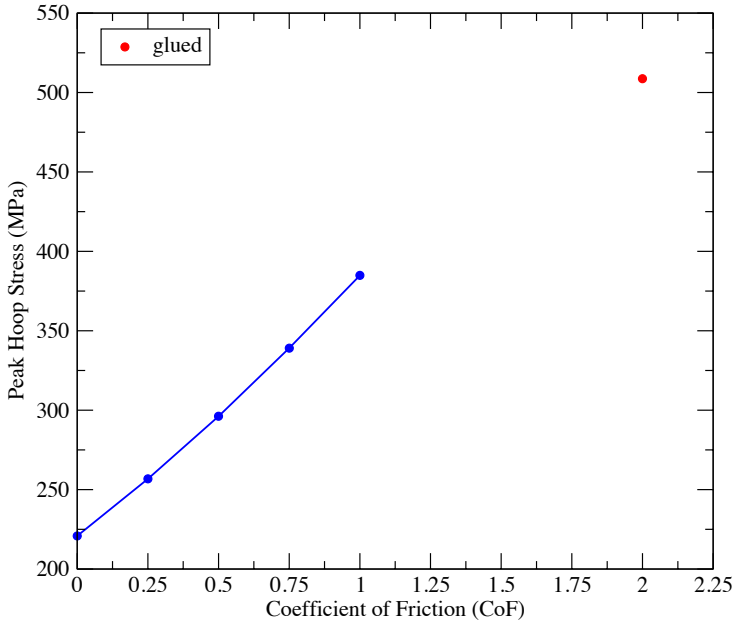

Figure 4-4. The relationship between peak hoop stress (y-axis) and the coefficient of friction (CoF) (x-axis) for 2-D R-Theta models, in which glued contact is considered to be CoF = infinity.

Choosing a CoF to use for the PCI analysis is a difficult task. At lower burnups, the outer fuel surface is considered to be smoother as is the inner clad surface, which has had less time for internal corrosion. Both of these will allow more slippage in the fuel, resulting in a lower CoF. However, higher burnup fuel has a rougher surface and the cladding will have fission product corrosion creating a stickier surface, resulting in a higher CoF. The OverRamp rods are lower in burnup, therefore a CoF of 0.75 was chosen for the 2-D R-Theta modeling assessment. Contact in 3- D is significantly more complicated. To simplify contact for the 3-D simulations, we have assumed glued contact in the 3D BISON ramp test modeling. The peak cladding hoop stress and strain energy density (SED) results from the OverRamp rod analyses are summarized in Table 4-4 for the non-failed and failed rods, respectively.

Table 4-4. Peak hoop stress and strain energy density (SED) values calculated using Bison in 2D (R-Z, R-Theta) and 3-D.

	W4-1 (F)	W4-2 (NF)	W5-4 (NF)	W5-5 (NF)	W5-6 (F)
Burnup (MWd/tU)	19.02	19.02	15.25	20.7	20.7
2-D R-Z (MPa)	93	75.2	30.3	112	140
2D R-Theta (MPa)	437	330	301	525	529
2D R-Theta (SED in MJ)	1.45	.862	.74	2.03	2.09
3D R-Theta (MPa)	548	391	232	554	639
3D R-Theta (SED in MJ)	2.2	1.52	.683	2.58	2.83
Falcon 2-D R-Theta (MPa)	N/A	N/A	291.8	453.2	474.2

F – Rod that failed

NF – Rod that did not fail

Based on the results summarized in Table 4-4, a comparison of rods with similar burnup (e.g. W4-1 compared to W4-2 and W5-5 compared to W5-6), indicates that the failed rods have higher calculated stresses and strain energy density (SED) than do non-failed rods. This is true for both the 2D (R-Z and R-Theta) and 3-D simulations performed with BISON. When comparing calculated hoop stresses in the R-Z simulations to the PCI simulations, the hoop stress is expected to be significantly higher in the PCI simulations. This is because the existence of radial cracks causes significant stress concentration in the fuel clad [61,62]. During the transient increase in power, radial cracks open and the coupled opening of the cracks plus the closure of the pellet-clad gap produces an increase in both the hoop stresses and the SED in the cladding. For classical PCI simulations, there should be no significant difference between the stress levels

calculated by a 3-D versus a 2-D model, however there may be some potential differences between the calculated SED. This stems from the 3-D model accounting for axial expansion, and SED is calculated using the tri-axial stress state. The fuel tends to expand more axial than the cladding, and this difference in axial expansion can cause increased axial stresses in the cladding. When comparing the 2-D stress and SED values to the 3-D values it is clear there is a difference between the two models. Furthermore, the comparison between the 3-D and 2-D results points to a need for 3-D pellet defect modeling.

To develop a failure threshold limit, whether stress, SED, or CDI, every rod needs to be compared equally and not separately. Figure 4-5, 4-6, and 4-7 summarizes the failed and non-failed rods stresses and SED as a function of burnup and compares peak hoop stresses as a function of gap thickness. Both Figures 4-5 and 4-6 assume elastic properties in the clad and Figure 4-6 accounts for instantaneous plasticity. Figure 4-5a and 4-5b shows the data are scattered and that there is not a true failure threshold stress or SED. SED appears to have a little more separation between failed and non-failed rods, but as previous studies have shown, the more data that populates the graph, the more this distinction in failure threshold is blurred [61,62]. The 3-D stress and SED values seem to give a little more separation between both stress and SED values, and shows that the axial height of the pellet plays a role in the calculation of the peak stress. However, there is still not enough separation in the data to determine a failure value. There is a clear trend that emerges in Figure 4-5c and 4-6c. As the size of the gap decreases the peak stress increases. Figure 4-6 asses a physically more accurate picture and include instantaneous plasticity. Figure 4-6a clearly shows when considering plasticity the peak hoop stresses are significantly decreased. Furthermore, with the yielding stress of irradiated Zr4 being ~600MPa many of the data point fall between 550-600 MPa. This evaluation clearly shows that to do a stress based failure threshold probability plasticity must not be considered and the cladding must be considered to be elastic only.

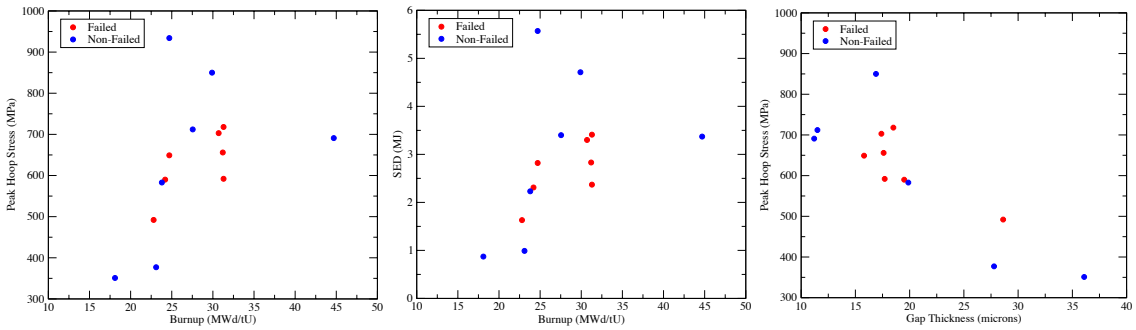

(a) (b) (c)

Figure 4-5. 2-D modeling results using elastic cladding properties of ramp tests assessing the appropriateness of a failure probability based on a) peak hoop stress or b) strain energy density, as a function of burnup, and c) peak hoop stress as a function of gap thickness

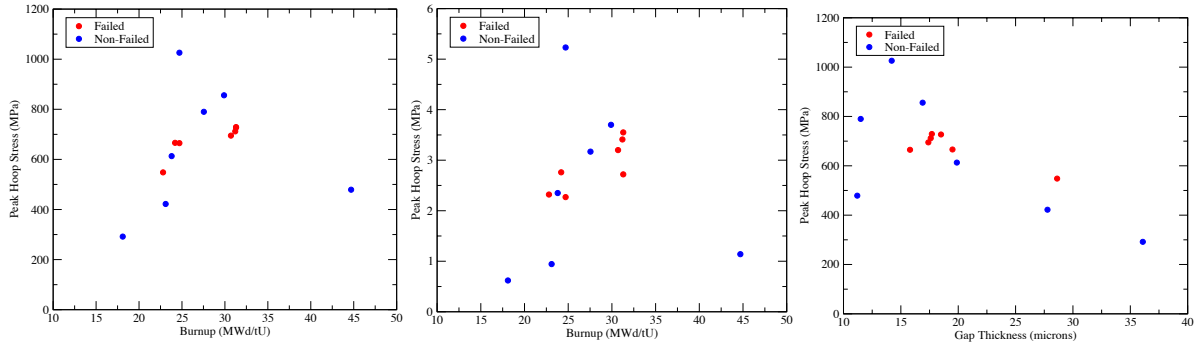

(a) (b) (c)

Figure 4-6. 3-D modeling results using elastic cladding properties of ramp tests assessing the appropriateness of a failure probability based on a) peak hoop stress or b) strain energy density, as a function of burnup and c) peak hoop stress as a function of gap thickness

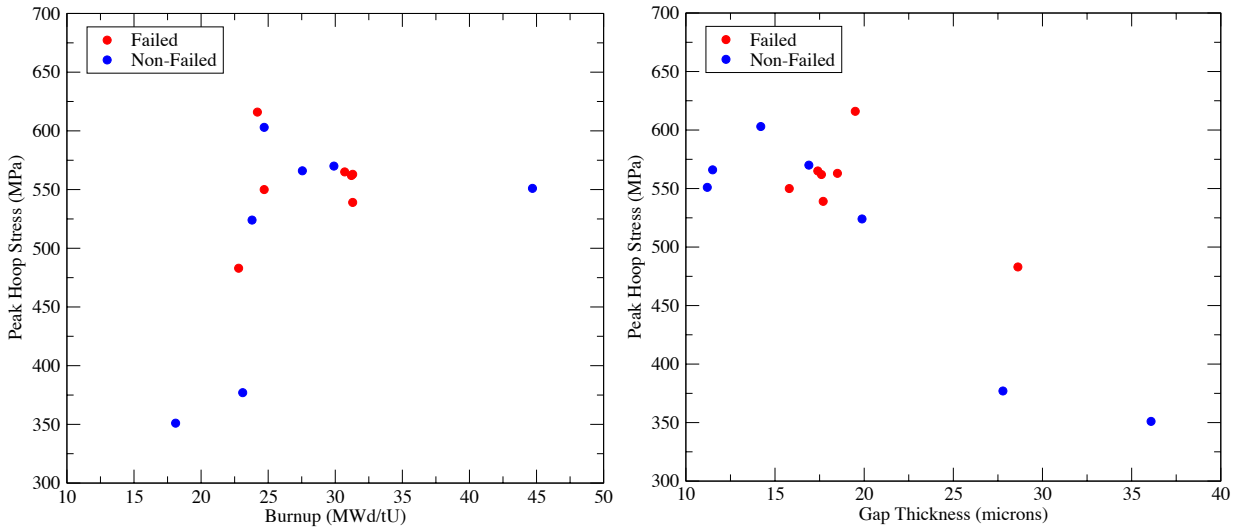

(a) (b)

Figure 4-7. 2-D modeling results including instantaneous plasticity cladding properties of ramp tests assessing the appropriateness of a failure probability based on a) peak hoop stress, as a function of burnup and b) peak hoop stress, as a function of gap thickness

4.1.C Assessing the issues for modeling CDI

Cladding failures related to SCC are considered to fail at stresses lower than the yield stress of irradiated zircaloy, which is typically around the 600MPa. Figures 4-5 and 4-6 show many of the calculated stresses are much higher than 600MPa, which will cause problems when using CDI failure based model. CDI is calculated in bison using the calculated yield stress of zicaloy as well as the applied hoop stress. As stress is applied, the cladding will accumulate more damage. The damage model assumes, once the CDI value reaches 1 then failure has occurred. However, Falcon results show the CDI model will calculate higher values and needs to be calibrated [67]. Figure 4-8 shows a power and a calculated stress history plots of the TransRamp-IV Q11-3 experiment. The calculated hoop stress exceeds zicaloys yield stress by a significant amount. It is important to understand why bison is calculating such high cladding hoop stresses.

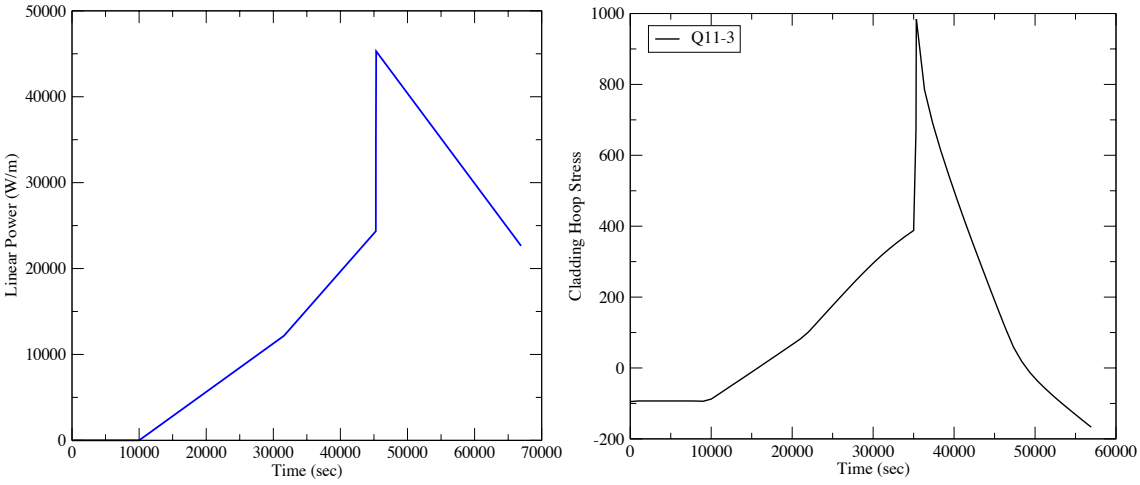

Figure 4-8. a) Average linear power history for the TransRamp-IV Q11-3 experiment and b) is a R-Theta bison stress history calculation for the power history shown in a).

Figure 4-8 shows that extreme stress values result from a lack of material properties in the R-Theta simulations. The results in Figure 4-8 b) do not account for thermal densification know as hot pressing or fuel creep, and Figure 4-8 a) and b) introduce hot pressing and creep to the R-Theta simulation in order to evaluate there affect on the results. As shown in Figure 4-8 a), hot pressing clearly reduces the radial displacement in the fuel. Hot pressing models sintering of the pellet. As the fuel temperature raises, the pellets will density further resulting in a larger pellet-cladding gap. However, fuel creep only softens the fuel after reaching peak power. These results conclude, missing material models are the culprit to the extreme stress. However, the R-Theta simulations are initiated from R-Z simulation results, and if the R-Z results are incomplete then the R-Theta results will suffer. Therefore, it is more important to understand and finish the implementation of material models for the R-Z simulations before improved results from the R-

Theta simulations can be expected.

The R-Z results are impacted by a number of material models. The first of these is smeared cracking, which is not considered in this analysis. Smeared cracking accounts for fuel fracture that occurs as a result of thermal stresses. This fracture leads to radial expansion and a decrease in the fuel compliance. Furthermore, with smeared cracking not being modeled, fuel creep has been turned off because fuel stresses are to high and causes a significant reduction in the fuel radial expansion. Secondly, Bison uses the Matpro UO_2 swelling model, which has a much faster swelling rate than other fuel performance codes. Lastly, at high enough temperatures UO_2 is susceptible to plastic flow and will affect the compliance of the fuel as well as the fuel-cladding gap. Future efforts should be prioritized to investigate smeared cracking, hot pressing, plastic flow, fuel creep, and fuel swelling.

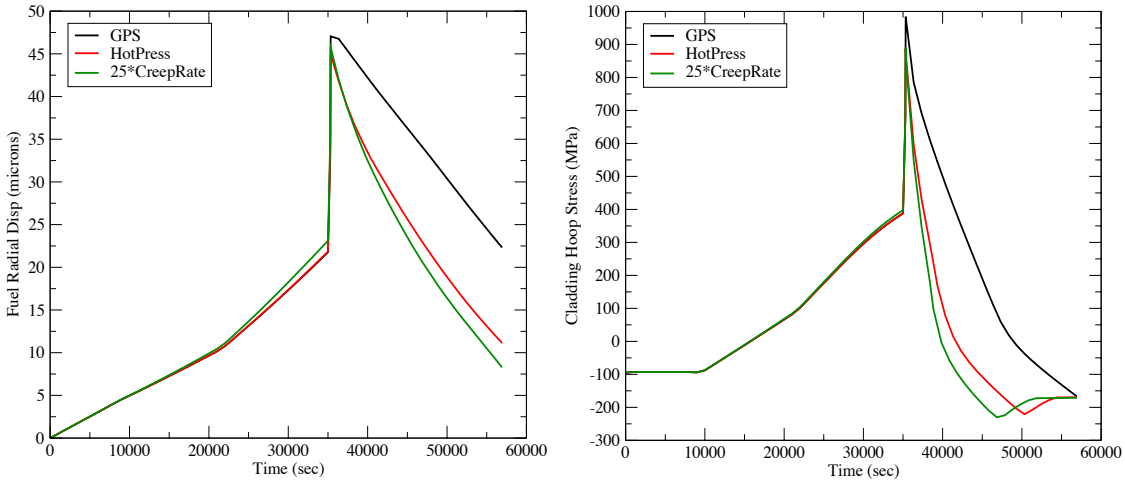

(a) (b)

Figure 4-9 a) Compairs the fuel radial displacement between a generalized plane strain (GPS) simulation (black), a GPS with hot pressing and creep (red), and a GPS simulation with hot pressing and factor of 25 times the normal creep rate and b) Evalutes the stress history between the three simulations.

4.2 Bison Modeling Assessment of Failed and Non-Failed Fuel Rods in a Commercial Power Reactor

4.2.A Approach

Westinghouse provided data required to construct a full-length model (R-Z geometry) used to analyze the selected commercial reactor fuel rods with BISON using the steady state, startup power histories, and axial power profile [63-68]. The full-length R-Z model analyses will be used to identify the axial location with the highest cladding hoop stress, and also to determine the fuel-cladding gap condition, following the stead state cycle, for the more detailed local PCI analysis with the R-θ slice model and a more detailed 3-D 5 pellet model. The principal fuel rod

design parameters used in the analysis are shown in Table 4-5.

Models for a Westinghouse 17x17 IFBA fuel rod were constructed with detailed fuel design data supplied by Westinghouse. In addition to the geometric mechanical model, a detailed power history which captures sufficient spatial and temporal power resolution to model both global and local conditions must be developed for a reliable PCI analysis. Exelon and Westinghouse have provided a detailed steady-state and power ramp data which has been used to construct the necessary power histories for the BISON analyses, which is shown in Figure 4-10. The rod average power history, Figure 4-10a, maintains a relatively constant linear power of 4 kW/ft and increases linearly to a final power of 5.25 kW/ft followed by a power down at the end of cycle 10. However, the power at the location of peak power begins by a rapid increase to 5.5 kW/ft, then remaining relatively constant with a few instances of increasing in power until reaching 6-6.5 kW/ft. Following the end of cycle 10 is the startup of cycle 11, as detailed in Figure 4-10b. Rod failure was observed for this commercial reactor during the cycle 11 startup, for which the peak power location reaches a significantly higher power than the rod average. The peak power position causes the pellet-cladding gap to close faster, leading to a smaller gap upon the startup of cycle 11. This is the axial location where a PCI related failure would most like occur.

The fuel rods described in Table 4-5 use a ZIRLO^{TM} cladding. CASL does not have material property data and models for ZIRLO. However, data previously supplied by Westinghouse and analyzed in the literature [65,69] indicates that the creep and irradiation growth of ZIRLO can be effectively modeled by reducing the corresponding models of Zircaloy-4 by 20% [70-72], as has been done in this analysis.

The failed fuel rods from the commercial reactor contained a unique burnable absorber, ZrB_2, which is placed as a thin coating on the fuel pellet outer circumferential surface, and referred to as an integral fuel burnable absorber, IFBA pellets [64]. The neutron capture by B-10 produces He and Li atoms, which are initially entrapped in the ZrB_2 layer. The helium will ultimately escape to the fuel rod void volume, thus changing the fill gas quantity and rod internal pressure. A special model for the helium release from the ZrB_2 coated pellets will need to be developed for BISON based on information of the release rate, provided by Westinghouse. The information for this model was not received in time, so for the purposes of this report BISON assumed there was not an IFBA layer. This will result in lower plenum pressure and more cladding creep down.

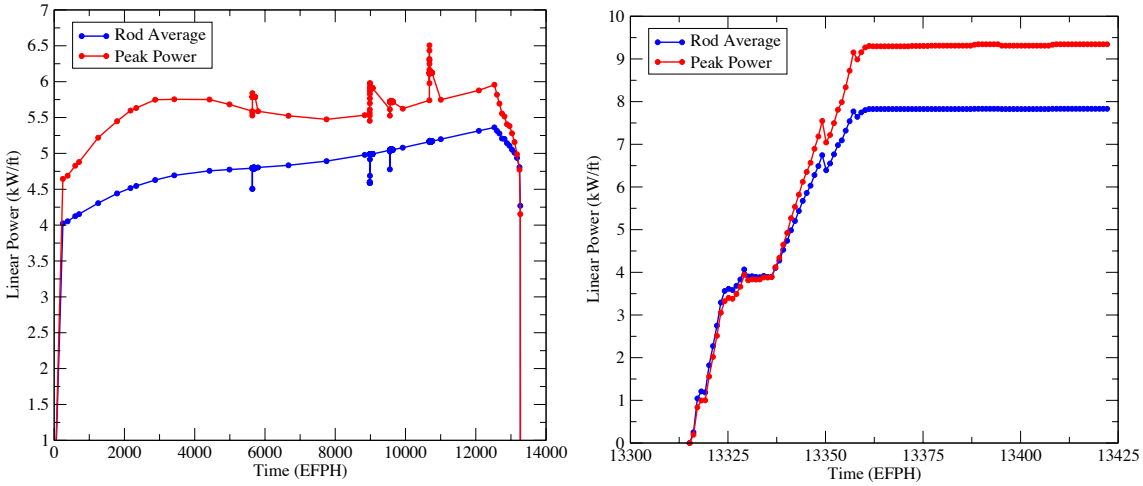

Figure 4-10. Average power history (blue) and the linear power at the axial location corresponding to peak power (red) for fuel rod M16S O05 a) during cycle 10 operation at a commercial power plant and b) during the cycle 11 startup, as obtained from [64].

Table 4-5. Westinghouse 17OFA fuel rod parameters needed for commercial PWR analysis, as obtained from Ref [73].

Rod Description	Value
Cladding outer diameter (inch)	0.360
Cladding inner diameter (inch)	0.3375
Cladding Material	ZIRLO^{TM}
Cladding surface roughness (micro-inch)	16
Pellet outer diameter (inch)	0.3088
Pellet surface roughness (micro-inch)	80
Radial gap (mils)	28.7
Enrichment (%)	4.6-4.95
Fuel density [% of T.D.]	95
Internal gas pressure [He] (psig)	275
Dished pellet	Yes
Fuel stack length (inch)	144.0

4.2.B Results

In order to identify the maximum cladding hoop stress location during the startup of cycle 11 in a commercial power reactor, a full-length BISON R-Z analysis was performed for the selected fuel rods using the cycle 10 and cycle 11 power histories, which were obtained from Exelon and Westinghouse [75]. With this approach, the magnitude and axial location of peak cladding stress were identified during cycle 11 startup. The R-Z analysis results from cycle 10 were then used as initial conditions to model the local effects of PCI in 3D during the cycle 11 startup.

Based on the failure assessment sensitivity work described in section 3.2, the same methodology was used to evaluate both the cycle 10 and cycle 11 startup. The conditions for the R-Z simulations are listed below, with the only change being the densification parameter. This change from the previous ramp test analysis was made based on the fact that the Westinghouse fuel used in the commercial reactor was more stable than early fuel forms used during ramp test program, and this would result in less densification occurring.

R-Z Problem Set Up

- Coolant and Plenum Pressures
  - Pressures are only applied to cladding inner and outer tube surfaces
- ESCORE Relocation Model
  - Activation = 5 kW/ft
  - Stop = Rod average burnup at the end of the base irradiation
- Fuel Creep
  - Turned off, Bison does not currently have reliable smeared crack model
- Fuel Densification
  - .05%, Ramp test used older fuel which is unstable allowing for more densification to occur

Many of the cycle 10 rods experienced higher nodal power during the cycle 10 base irradiation when compared to non-failed rods from cycle 9. The specific power history for cycle 10 and the startup of cycle 11 are shown in Figure 4-11, for both failed (a and b) and non-failed (c and d) rods. Assembly M36S contains the most aggressively operated rods, for which the fuel rod M36S_D13 reached a peak nodal power of 10 kW/ft during cycle 10. Correspondingly, these rods accumulated higher rod average and nodal burnup. However, several rods, including those designated as M19S_I02, M12S_B06, and M36S_M14 experienced comparatively smaller power changes during the cycle 11 startup than the failed rod, which was M16S_O05.

Fuel rod M16S_O05 has a much lower rod average burnup compared to the other non-failed rods, but it experienced the largest change in power between the cycle 10 coast down power and the cycle 11 startup. As the M19S_I02, M12S_B06 and M36S_M14 rods have experienced higher nodal power during the Cycle 10 base irradiation, the pellet-cladding gaps for

these rods closes after about 350 EFPDs, within their first cycle, in the reactor. Comparisons between BISON and Falcon fuel performance assessments of fuel – clad gap and displacements for rod M12S_B06 are shown in Figure 4-12, and again provide confidence that BISON is predicting similar quantitative results to Falcon.

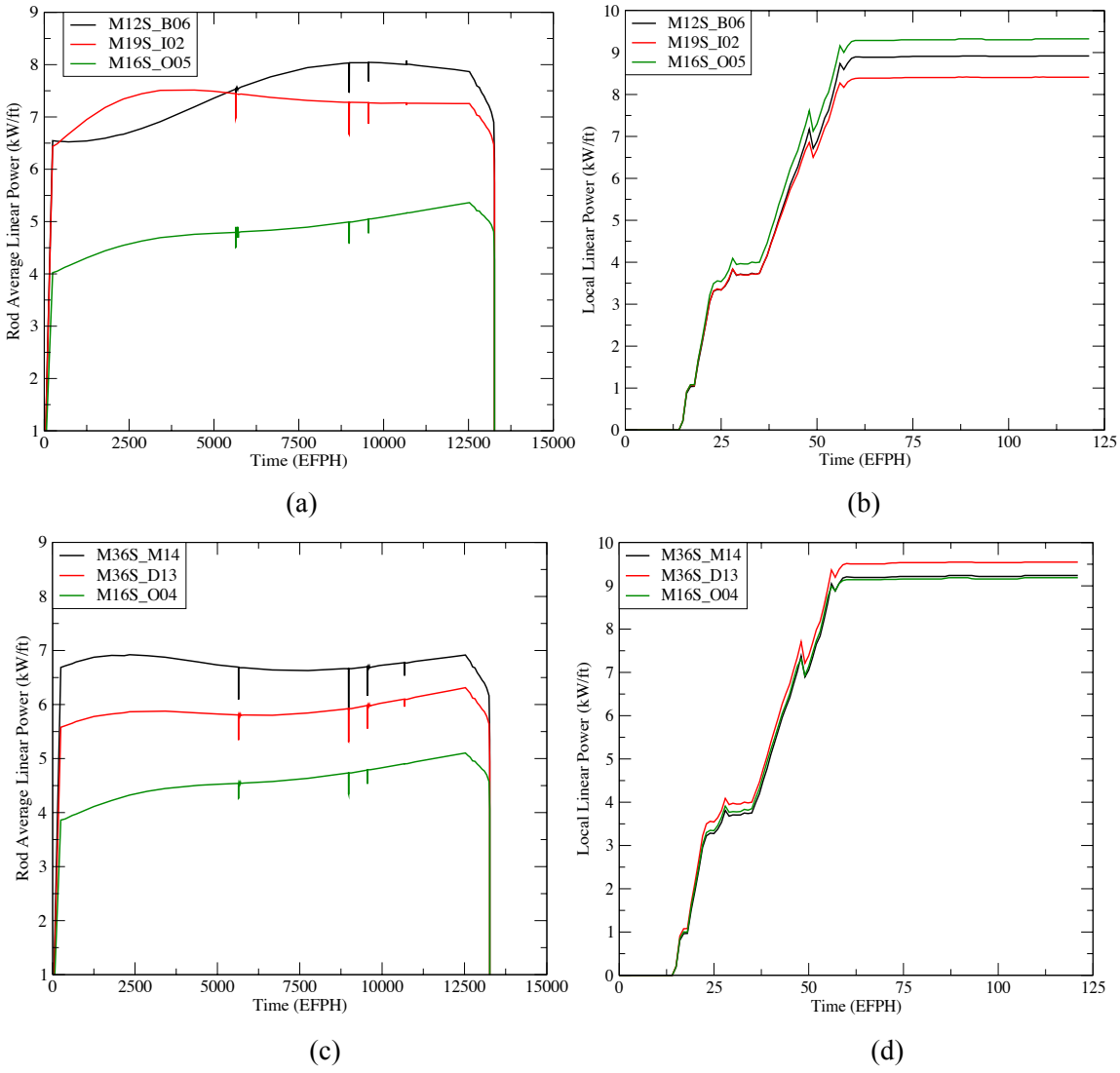

Figure 4-11. Power histories for failed and non-failed fuel rods within a commercial nuclear power plant during cycle 10 and the startup of cycle 11. a) cycle 10 power history for three rods which subsequently failed, b) local linear power at the axial location of peak stress during cycle 11 startup. c) cycle 10 power history for three rods which did not fail, and d) local linear power at the axial location of peak stress for the three non- failed rods during cycle 11 startup of a commercial nuclear power plant.

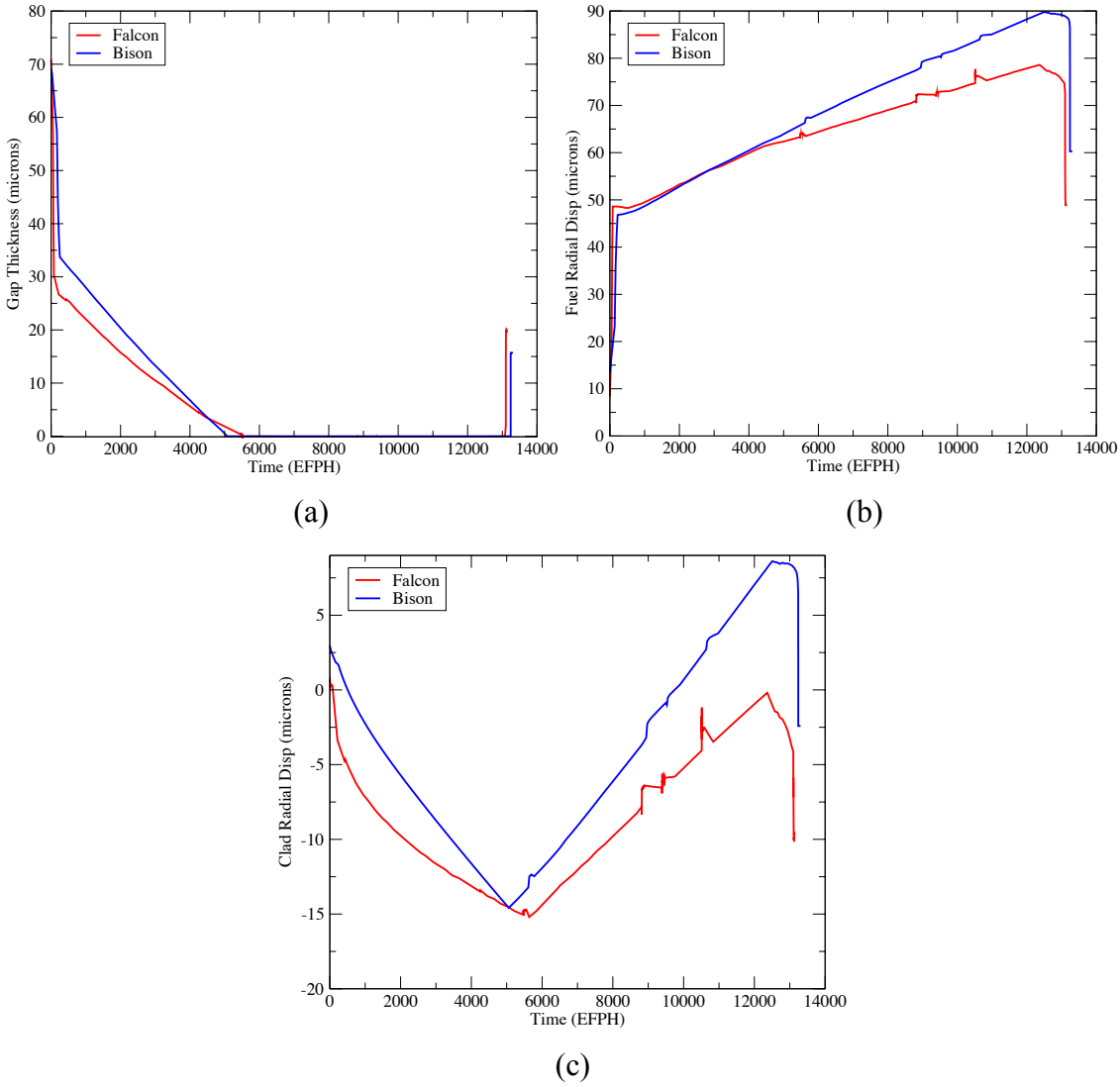

Figure 4-12. Comparison of BISON and FALCON fuel performance simulations during cycle 10 and the startup of cycle 11 of the commercial reactor. (a) gap thickness as a function of effective full power hours, (b) fuel radial expansion as a function of effective full power hours, and (c) cladding radial displacement as a function of effective full power hours.

As shown in Figure 4-12a), BISON under predicts relative to Falcon the pellet-cladding gap for the length of the simulations. There are a number of differences between the two codes that affect the results. The first being simulation boundary conditions. As stated earlier, BISON does not assume any pressure acting on the top or bottom of the cladding, where as Falcon assumes a plenum spring, plenum pressure, and coolant pressure to be acting on the cladding. With Falcon modeling the force of the spring it would be expected for Falcon to have less initial radial expansion than BISON. As the power begins to increase Falcon calculates a smaller gap when compared to BISON, seen in Figure 4-12b). This is contributed to smeared cracking as well as hot pressing. BISON does not include smeared cracking, with the reason being that fuel

creep is turned off, where as Falcon does. Smeared cracking allows for more fuel expansion based internal stresses causing the fuel to crack. Hot pressing is the act of sintering or thermal densification. The fuel gets hot enough to allow for thermal densification to occur. Another difference between Falcon and BISON is the fission product swelling model. BISON uses a MATPRO model, which assumes a faster swelling rate than the Falcon model. Lastly, the BISON simulation does not have an IFBA model to account for He release during irradiation. IFBA rods contain a burnable absorber, ZrB_2, as a coating on the outer fuel surface to absorb thermal neutrons. Following neutron absorption, boron undergoes alpha decay, thereby producing helium, which over time will contribute to an increase in the plenum pressure. The increase in plenum pressure will affect the expansion in the cladding creating a slightly larger pellet- cladding gap.

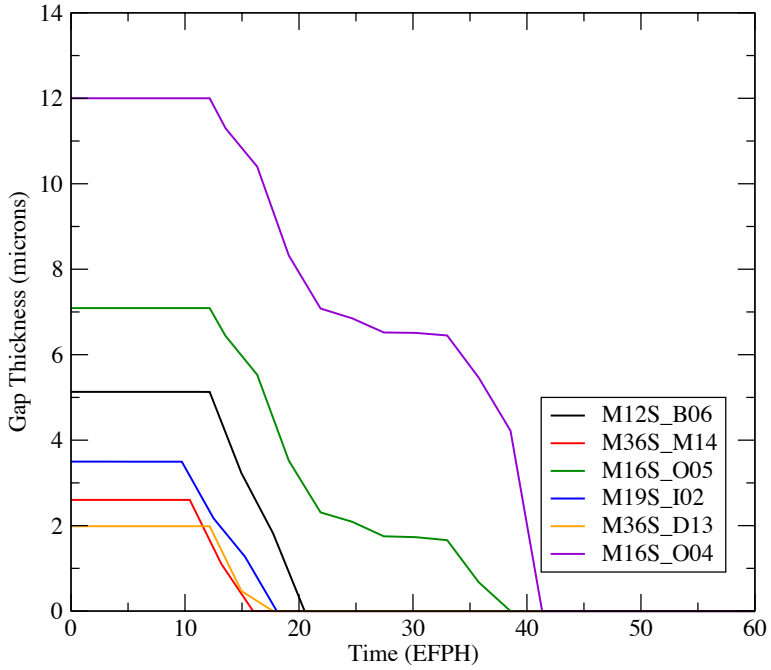

Figure 4-13. Gap thickness for both the failed and non-failed fuel rods during the commercial reactor cycle 11 startup, as predicted by a 2D R-Z BISON model.

Figure 4-13 compares the hot zero power gap along with the response to an increase in power. Figure 4-13 clearly indicates that the rods that experienced the highest nodal burnup have the smallest fuel- clad gaps. As the nodal burnup increases, the fuel expands more and the cladding creeps down more, resulting in a smaller gap. For the two rods within a single assembly, M16S_O04 and M16S_O05, the pellet-cladding gap remained open for the duration of cycle 10. However during the cycle 11 startup, all rods closed the gap. The results from Figure 4-13 further provide confidence in our R-Z simulations and correspondingly, provide the initial conditions need for a more detailed failure assessment in 3D. Table 4-6 provides a summary

from the 2-D PCI analysis, including for rod M16S_O04 which contained a MPS of varying size. Also cladding plasticity was not include in the Table 4-6. It was determined for a stress failure threshold to be determined the cladding needed to be treated as an elastic material and not account for instantaneous plasticity.

Table 4-6. Summary of the 2-D PCI and MPS peak stress and SED analysis.

	Rod Avg Burnup (MWd/tU)	PCI Peak Stress	PCI SED	60mil Peak Stress	60mil SED	125mil Peak Stress	125mil SED
M16S_O05 (F)	20.7	335	.894	537	1.67	685	4.76
M16S_O04 (NF)	19.6	274	.613	459	1.22		
M12S_B06 (F)	33.24	421	1.36	629	2.29		
M19S_I02 (F)	31.6	414	1.32	622	2.24		
M36S_D13 (NF)	25.5	463	1.63	687	2.72		
M36S_M14 (NF)	29.3	458	1.6	668	2.59		

F – Rod that failed

NF – Rod that did not fail

Table 4-6 further validates the results shown in Figure 4-13. In all cases, the 2D R-Z model results presented in Table 4-6 indicate that the fuel rods with higher rod average burnup generally have higher maximum clad hoop stress values. However, the highest hoop stresses are predicted for the M36S rods, which do not have the highest rod average burnup and that did not experience fuel failures. The fuel rods in the M36S assembly were operated with an aggressive axial profile, meaning that the axial burnup values varied substantially. With the peak stress being located at a nodal location exposed to higher powers for long periods of times, it would have accumulated a much higher burnup as compared to the rest of the rod resulting in a smaller local gap.

Conducting the same PCI analysis as performed in section 3.2, yields a similar result for the R-Z analysis. The presence of radial crack(s) increases the hoop stress on the inner surface of the cladding. When referring back to Figure 4-4 of section 3.2, fuel rods began to fail around stresses of ~450 MPa and a SED of ~1.5 MJ, which are comparable to the values obtained in the

analysis performed by Lyon and co-workers [59,60]. However, when using these values as a potential threshold failure value for the commercial fuel rods shown in Table 4-6, it is not possible to explain why rods M19S_I02, M16S_O05, and M12S_B06 failed. The stress and SED values for the M16S_O05 fuel rod clearly fall below the failure threshold values, and therefore, this 2D analysis rules out classical PCI as a failure mechanism. M19S_I02 and M12S_B06 both have peak stresses and SEDs comparable to those seen in failed rods in Figure 4-4, and thus it is possible that classical PCI could have been the responsible failure mechanism in these two rods. Again, however, the M36S rods have higher stress levels and higher SEDs than rods M12S_B06 and M19S_I02, which provides some evidence against classical PCI as the failure mechanism. Correspondingly, we have analyzed several of these rods with MPS defects to assess whether an MPS is the cause of fuel cladding failure.

Table 4-6 also documents the calculated stress and strain energy density when MPS, with a dimension of 60 mils is present in the fuel rods. As anticipated, the presence of a MPS significantly increased the calculated cladding hoop stresses. When comparing the two fuel rods, M16S_O04 and M16S_O05, which had similar burnups and gap thickness due to being companion rods in the assembly, the failed rod M16S_O05 has consistently higher stresses than the non-failed rod M16S_O04. The clad hoop stress history is plotted in Figure 4-14 for these two rods for the various analysis assumptions summarized in Table 4-6. This 2D MPS analysis appears to confirm the conclusion that the presence of a MPS is needed for rod M16S_O05 to reach sufficiently high hoop stress to initiate failure, and lends credence to the assumption that a MPS potential could have been present in the failed rods M12S_B06 and M19S_I02. The PIE examination of rod M16S_O05 [74] clearly identified the presence of a large MPS, which had a width of ~125mil and a length of ~3/4 pellet length at the failure location [74]. By incorporating a 125mil MPS in the 2D BISON simulation, the maximum hoop stress in the clad is increased to 685 MPa, also shown in Figure 4-14. This validates the conclusion that MPS was the cause of failure in rod M16S_O05.

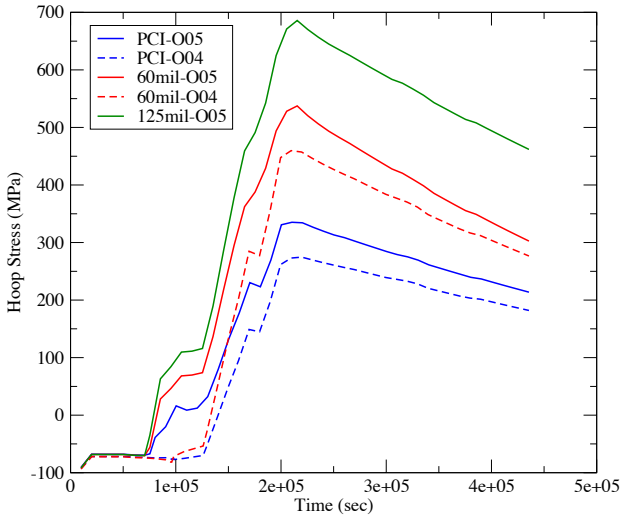

Figure 4-14. Predicted maximum hoop stress in the clad for fuel rods M16S_O05 and M16S_O04 during cycle 11 startup for various analysis assumptions.

Table 4-7 summarizes similar analysis data as that of Table 4-6, however, the results in Table 4-7 come from a full 3D modeling analysis for PCI and MPS defects. The same general trends hold for the 3D analysis as the 2D results, however. The results of Table 4-7 should also be considered with respect to the 3D modeling of the ramp test results presented in Figure 4-5 of section 3.2. That analysis indicated that appropriate failure probabilities should be considered as a critical value of ~437 MPa for stresses and 1.45 MJ for SED. A comparison to the results presented in Table 4-7 again indicate that classical PCI can not be the cause of failure in rod M16S_O05, but potentially could have been the underlying cause of failure in rods M19S_I02 and M12S_B06. Further evaluation of the presence of the MPS defect reinforces the conclusion that the MPS is the root cause for the cladding failures.

Table 4-7. Summary of the 3-D PCI and MPS peak stress and SED analysis for the commercial reactor fuel rods.

	Burnup (MWd/tU)	PCI Peak Stress	PCI SED	60mil Peak Stress	60mil SED	125mil Peak Stress	125mil SED
M16S_O05 (F)	20.7	451	1.48	594	2.19	772	3.51
M16S_O04 (NF)	19.6	374	1.06	566	2		
M12S_B06 (F)	33.24	533	2.01	699	2.86		
M19S_I02 (F)	31.6	528	2	699	2.88		
M36S_D13 (NF)	25.5	N/A	N/A	746	3.24		
M36S_M14 (NF)	29.3	533	2.16	736	3.16		

F – Rod that failed

NF – Rod that did not fail

As previously reported, the results presented in Table 4-6 and 4-7 did not account for the IFBA's He contribution to the plenum pressure. A fundamental model was developed based on simple reaction kinetics to determine the potential amount of He that could be released in the plenum, see the equation below:

$$R = \left(\frac{\rho\sigma\phi SAt}{m}\right)P$$

Where ρ is the density of ZrB_2, σ is the thermal absorption cross-section for boron-10, SA is the IFBA surface area, t is the thickness, m is the mass of ZrB_2, and P is fraction of He released into the plenum. This equation defines the neutron absorption rate for ZrB_2. A simple percentage is multiplied by R to determine the amount of He that is released into the plenum. This is a simple model and is expected to give an over estimate of He released into the plenum. A more in-depth model would need to account for B-11 decay rates, burnup, and more in formed He released rates. However this model gives us a simple understanding of the physics and how they will affect the results.

The addition of the IFBA model is a cumulative affect, e.g. as more IFBA is consumed the more He will be released. As the He is released into the plenum the plenum pressure is expected to increase. Cladding creep down is controlled by two main mechanisms. First is irradiation creep, and the second is contributed to the coolant pressure on the exterior of the cladding and the plenum pressure on the interior of the cladding. The coolant pressure remains relatively constant, however the plenum pressure does not. As the rod is brought to hot zero power the plenum pressure will increase ~3 times the original amount. Over time the gap will close, fission products will be released into the plenum, and in this case He will be released as well. This can cause a significant increases in the plenum pressure, and begin to push back on the coolant pressure, essentially resisting cladding creep down. Table 4-8 illustrates the changes in the cladding creep down, gap thickness, and plenum pressure when comparing between simulations that do not model IFBA and simulations that do model IFBA. Looking at Figure 4-15 shows it is evident that modeling IFBA does have an affect on the results, as also summarized in Table 4-8. As noted previously, the IFBA model implemented would over estimate the amount of He produced and released into the plenum. However, it clearly show that as He is released into the plenum the cladding will creep down less resulting in a larger gap, and this is contributed to the increase in the plenum pressure.

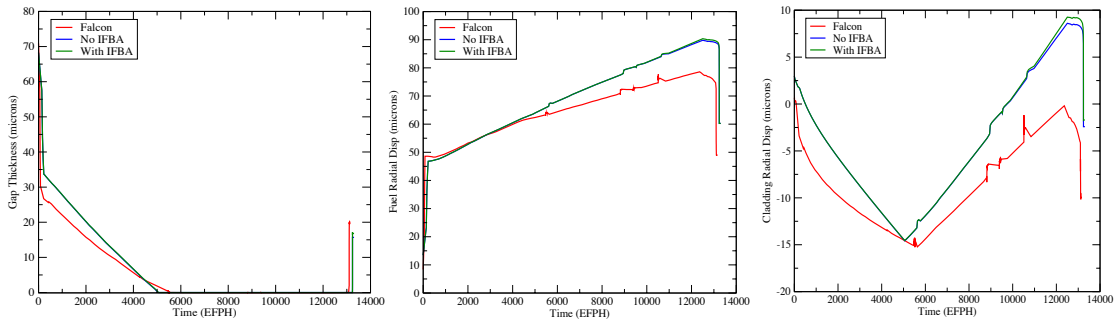

(a) (b) (c)

Figure 4-15. Comparison of BISON and FALCON fuel performance simulations during cycle 10 and the startup of cycle 11 of the commercial reactor with and without an IFBA model. (a) gap thickness as a function of effective full power hours, (b) fuel radial expansion as a function of effective full power hours, and (c) cladding radial displacement as a function of effective full power hours.

Table 4-8. Comparison between simulations modeling IFBA and simulations that did not model IFBA.

		Modeled without IFBA			Modeled with IFBA		
Properties	Burnup	Clad Creep	Gap Thickness	Plenum Pressure	Clad Creep	Gap Thickness	Plenum Pressure
Units	(MWd/tU)	microns	Microns	MPa	microns	Microns	MPa
M16S_O05 (F)	20.7	-32.9	13.2	3.4	-25.8	16.4	4.38
M16S_O04 (NF)	19.6	-31.8	16.4	3.3	-20	19.88	4.24
M12S_B06 (F)	32.4	-2.7	15.7	3.4	-1.7	16.7	4.48
M19S_I02 (F)	31.6	-11.2	8.1	3.78	-3.18	16.2	4.5
M36S_D13 (NF)	25.5	-26.1	6.7	3.6	-20	12.6	4.5
M36S_M14 (NF)	29.3	-16.8	7.3	3.65	-10.46	13.8	4.55

F – Rod that failed

NF – Rod that did not fail

Following the R-Z simulation a PCI and MPS failure analysis was conducted to develop a better understanding as to why the rods failed. The results of both the 2-D and 3-D analysis are presented in Table 4-9 and 4-10. The peak stress values are lower than the simulations that did not contain IFBA. This is a result of having a larger gap and higher plenum pressures. Having a larger gap would delay gap closure until higher power is reached which would reduce the hoop stress on the inner surface of the cladding. The plenum pressure would act in a similar manner. A higher plenum pressure would reduced cladding elastic strain causing the gap to remain open. When comparing results from Table 9 and 10 to Table 6 and 7 the peak stresses are reduced. The conclusion drawn from Table 6 and 7 was that rod M16S_O05 must have contained a MPS for the rod to fail, and rods M12S_B06 and M19S_I02 could have failed by either PCI or MPS induced failure. The conclusion from Table 9 and 10 seem to point to failure by MPS being the leading cause of failure in M12S_B06 and M19S_I02. Using the current IFBA model it is impossible to be certain whether a pellet crack or a MPS caused the failure. However, including a IFBA model showed a larger pellet-cladding gap and higher plenum pressures both of which reduced the contact force between fuel and the cladding. Reducing the contact force would resist PCI related failures, and would point to a conclusion that a MPS was required to case M12S_B06 and M19S_I02 to fail.

Table 4-9. Summary of the 2-D PCI and MPS peak stress and SED analysis for the commercial reactor fuel rods accounting for He release from IFBA.

	PCI			60mil MPS			125mil MPS	
	Peak Stress	SED	CDI	Peak Stress	SED	CDI	Peak Stress	SED
M16S_O05 (F)	324	.72	2.9	502	1	350	650	6
M16S_O04 (NF)	248	.44	.66	404	.99	109		
M12S_B06 (F)	362	.88	1.7	577	1.7	450		
M19S_I02 (F)	235	.409	1.8	472	1.13	222		
M36S_D13 (NF)	431	1.23	1.23	668	2.27	1230		
M36S_M14 (NF)	415	1.14	1.14	605	2.15	2450		

F – Rod that failed

NF – Rod that did not fail

Table 4-10. Summary of the 3-D PCI and MPS peak stress and SED analysis for the commercial reactor fuel rods accounting for He release from IFBA.

	PCI			60mil MPS			125mil MPS	
	Peak Stress	SED	CDI	Peak Stress	SED	CDI	Peak Stress	SED
M16S_O05 (F)	362	.85	.18	550	1.93	2.19	685	2.75
M16S_O04 (NF)	316	.63	.04	540	1.56	2		
M12S_B06 (F)	414	.85	.85	543	2.06	2.86		
M19S_I02 (F)	385	1.12	1.13	643	2.16	2.88		
M36S_D13 (NF)	N/A	N/A	N/A	736	3.16	3.24		
M36S_M14 (NF)	443	1.29	1.2	730	2.81	3.16		

F – Rod that failed

NF – Rod that did not fail

The results presented in Table 4-9 and 4-10 have shown a MPS is needed for rod M16S_O05 to fail. This was further conformed form the hotcell examination of M16S_O05 performed by Y. Aleshin and co-workers [74]. However, the root cause of failure was never confirmed for rods M12_B06 and M19S_I02. Tables 4-9 and 4-10, both rods M12S_B06 and M19S_I02 had a lower calculated PCI stress when compared to the M36S rods and the majority of the rods in Figure 4-5 and 4-6. The stress levels of these two rods did not reach comparable stress levels to the failed rods until a MPS was considered to cause the failure. Theses findings prove rods M12S_B06 and M19S_I02 where not capable of failure under PCI related conditions, therefor a MPS had to have been present for these rods to have failed.

4.2.B.1 Evaluating Power Ramp Rate Restrictions

It is commonly believed that reducing cladding failure resulting from PCI to 0% can not be accomplished by assuring manufacturing quality alone. The analysis of fuel failures in a commercial reactor performed in this study is a clear example. Westinghouse uses a fuel quality assurance that does not allow a MPS of 60mils wide and 60mils in length to be loaded into a PWR [75]. This is an example where it is possible that the quality assurance broke down since the resulting MPS dimensions determined by post-irradiation examination clearly indicated an MPS length of 125 mils. Another possible approach to limiting PCI fuel failures is to limit the power ramp levels.

Figure 4-16 and Table 4-11 illustrate the results of our BISON modeling assessment of utilizing reduced ramp rates to reach peak linear power to reduce clad stress levels. The first method attempts to slow the ramp to full power by one-half, one-third and one-fourth of the original power ramp rate. For the power ramp and hold times in the current analysis, there is almost no affect seen by increasing the amount of time to reach full power. By continuing to increase the power, the fuel is constantly expanding radially and not allowing sufficient time for the cladding stresses to relax. However, the implementation of a constant power hold time during the power ramp can significantly reduce the cladding stresses. Figure 4-16a demonstrates the hold time at a power level of 80% of the maximum value. Figure 4-16b indicates that during this step power ramp, the clad hoop stress is able to significantly decrease, and that the resulting peak stress upon finally reaching full power is also substantially less than during a continual power increase. While this is a relatively simple test case to evaluate power ramp rate effects on the maximum clad stress, it does indicate that there are operational approaches to minimize the potential for cladding failure.

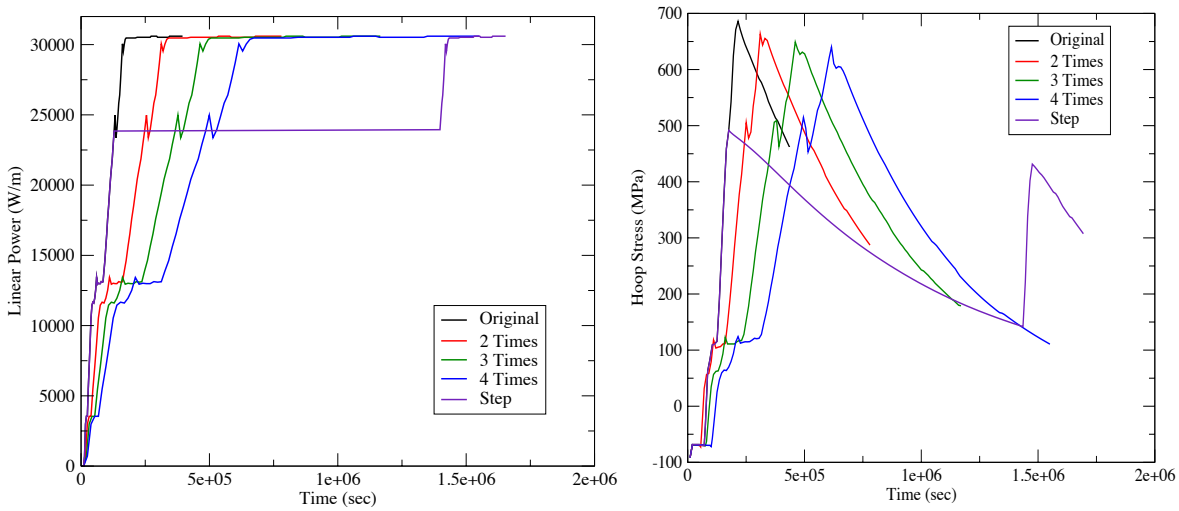

(a) (b)

Figure 4-16. a) Modified power histories and b) corresponding peak clad stresses during power ramp startup of cycle 11 for the fuel rod M16S_O05.

Table 4-11. Peak stress and SED values from the ramp study, shown in Figure 4-16a.

	Peak Stress (MPa)	Peak SED (MJ)
Classical PCI	251	4.76
Original Power History	685	6.85
2 Times Original	655	2.45
3 Times Original	648	2.4
4 Times Original	640	2.3
Step Added	491	1.36

4.2.B.2 Evaluating Uncertainty in Power Profiles

Power histories, material properties, as well as experimental cladding and fuel displacements have inherent uncertainties. It has been shown that rod average power histories can have anywhere from 3-5% and as much as 10% uncertainty associated with the measured power [76]. To evaluate the impact that uncertainties in the measured power may have on predicted clad stress and failure probability, we have performed an initial statistical evaluation of the impact on variations in the power history. Figure 4-17 evaluates the statistical uncertainties present in the measured power history, by reducing the power by 3-5% for rod M16S_O05 (failed) as well as by increasing the power by 3-5% for rod M16S_O04 (non-failed). Again, these rods were in the same assembly and operated under similar power conditions. The biggest difference between these two rods was M16S_O05 failed, due to the presence of a MPS.

Figure 4-17 indicates that there is a relatively small change in the hoop stress when the power is adjusted from 3-5%. But, when comparing the stress produced in rod O05 versus O04 by a 5% decrease or increase, respectively to the power history, this results in a ~25 MPa change in cladding hoop stress. This change in cladding stress is verified when comparing various pellet defects, e.g classical PCI and MPS, as shown in Figure 4-17. The analysis performed for Figure 4-18 uses the M16S_O05 geometry, and compares peak stresses produced by radial cracks and two different MPS widths. For each change (reduction in power history), there is a slight decrease in the peak cladding hoop stress. Figure 4-18 shows that a 5% change in power, either increase or decrease, can be expected to have an ~20MPa impact on the peak cladding hoop stress. Using a peak stress failure criteria model, this increase or decrease in cladding stress would be insignificant. However, more advanced crack evolution models may not consider this an insignificant increase in stress. Assuming a traditional mode 1 fracture toughness model, a full fracture mechanics analysis would indicate a stress concentration effect of about a factor of three times the applied stress near a crack tip. That means that an applied hoop stress increase of 20 MPa could result in a local stress at the crack tip which is higher by 60 MPa. It is unclear how this increase will affect the failure potential however, the results show how uncertainties in the power history can increase the cladding failure potential.

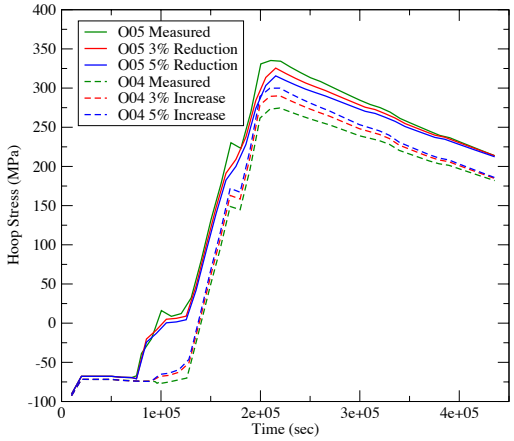

Figure 4-17. Predictions of the clad hoop stress for fuel rods M16S_O04 and M16S_O05, based on 3-5% variations in the power history during cycle 11 startup.

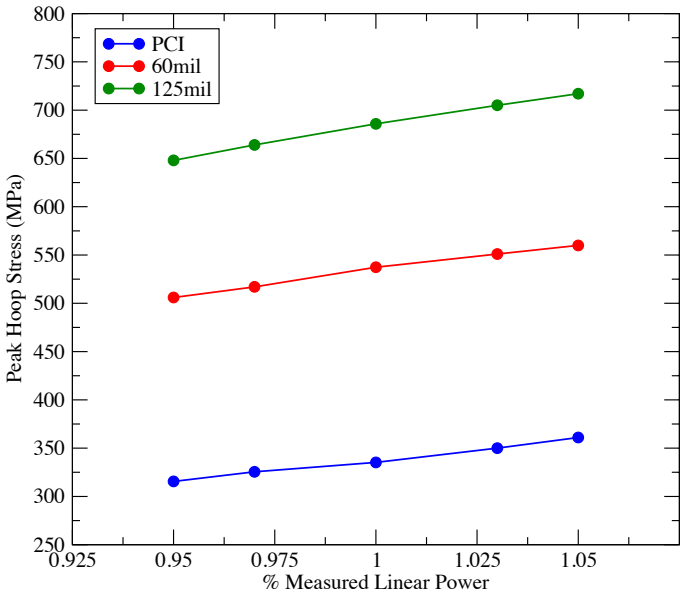

Figure 4-18. Evaluation of the peak clad stress in fuel rod M16S_O05 during cycle 11 startup, with variations in the linear power between ±5% based on analysis assumptions including a 60 mil or 125 mil MPS defect.

4.3 Conclusion and Future Work

This chapter used the BISON fuel performance code to evaluate a methodology for fuel failure assessment and to assess the modeling predictions against actual commercial power reactor fuel failure experience. Data from a set of PWR ramp test rods taken from the IFPE database were used to evaluate both the maximum hoop stress in the fuel clad, as well as the cladding SED, as possible failure assessment methodologies applicable to the PCI/MPS fuel failure mechanism. Secondly, this paper summarizes the BISON modeling results for fuel failures observed in a commercial nuclear power plant during the power ramp increase associated with startup during cycle 11 of that reactor's operation. The objectives of these analysis were to 1) evaluate the cladding hoop stress conditions at the suspected time of cladding failure to assess the potential role of PCI in the failure process, 2) provide a PCI fuel failure assessment to determine if the presence of a MPS was required for cladding failure to occur, and 3) demonstrate a reactor startup recommendations to minimize the potential for PCI related cladding failure.

The results of the BISON fuel performance modeling in 2D (R-Z or R-θ) are broadly consistent with current industry code capabilities, and the 3D modeling capability clearly provides a unique capability to industry. As with other assessments performed previously [59,60,64,74], the evaluation of fuel failure data from test reactor ramp tests indicates that the maximum hoop stress and SED based criteria will not adequately isolate failed rods from non-failed rods. Further, these methods are quite statistically sensitive to the assumptions used in the hoop stress and SED calculations. It appears that as a metric, neither the peak cladding hoop stress nor the SED alone, is sufficient to define rod failure. As a result, implementation of the failure probability thresholds defined by stress or SED could over conservatively restrict reactor

operation.

The fuel history from several fuel rods from a commercial reactor during operation in cycle 10 and startup to cycle 11 were used to evaluate the overall fidelity of the BISON fuel performance modeling. The BISON analysis demonstrated that both cladding hoop stress and SED increased significantly during the startup ramp between cycle 10 and the startup to cycle 11. The increase in these two possible failure indicators was caused by pellet-cladding mechanical interaction as a result of the fast startup ramp rate and the axial flux change. The BISON analysis in both 2D and 3D clearly indicated that the presence of a MPS was the cause for fuel rod M16S_O05 to have failed. Rods M19S_I02 and M12S_B06 both showed significantly lower PCI stress values when compared to other failed rods, and proves a MPS was the root cause for failure of these rods. Lastly, a demonstration of reactor startup power ramps has shown one possible power hold and ramp combination that has the ability to significantly reduce the maximum clad hoop stress and presumably minimize the potential for PCI related cladding failure. The potential for classical PCI based failures for higher burnup fuel than the rods analyzed in the current study remains for future consideration.

CDI was also considered in this analysis, but has been shown that bison is not robust enough to include all necessary material models for a R-Z simulation, e.g. smeared cracking, hot pressing, fuel plasticity, and fuel creep. However, bison has shown the capability to model CDI in the Braidwood cases, and once bison has improved its capabilities, a CDI failure threshold can be developed.

Finally, establishing the fuel rod conditions prior to a power maneuver remains a critical element to modeling the potential for PCI failure. Further work on BISON will focus on integrating micro-scale models under development in CASL-FMC that describe the irradiation creep and growth of zirconium alloys, the fracture, relocation, and mechanical compliance of the fuel pellet, and the release of fission products important for SCC (volatile and noble gases). The incorporation of these models into BISON, either directly or using improved semi-empirical relationships, will require expanding the validation activities of BISON to include more integral fuel rod irradiations, hot-cell examination data from commercial reactor fuel rods, and separate effects experiments.

Chapter 5: Summary

The basic mechanisms of PCI leading to SCC of nuclear fuel rods can be categorized into two main processes. The first category are those mechanisms that establish the equilibrium or initial fuel rod conditions prior to a transient condition, such as fuel pellet cracking induced by thermal gradients in the fuel, reduction of the pellet-cladding gap by fuel swelling and fuel fragment relocation, fission product induced swelling of the fuel, and irradiation creep of the cladding, and fission gas release into the pellet-cladding gap. The second category are those mechanisms that occur during and shortly following an increase in power, such as rapid pellet thermal expansion leading to high contract pressures with the cladding, localized cladding hoop stresses adjacent to a pellet crack due to induced shear forces, the release of volatile fission products, such as iodine, cadmium and cesium, swelling due to bubbles containing gaseous fission products in the fuel, and fuel and cladding stress relaxation due to thermal creep and pellet fragment accommodation. The goal of this dissertation using the Bison code is to contribute to the development of a high fidelity 3-D thermal and mechanical representation of the pellet and cladding behavior coupled with a more physics-based representation of the underlying mechanisms that lead to cladding failure. These mechanisms include the role of fission product transport, chemical reactions with the cladding, and irradiation effects on the mechanical behavior of the fuel pellet and cladding materials.

Overall, the objective of developing an advanced, 3-D fuel performance modeling capability to assess PCI is to: 1) reliably calculate the cladding failure potential related to PCI; 2) define the impact of, and tolerance for, manufacturing flaws along with the material properties on failure probability; and 3) evaluate the role of plant operating strategies as well as specific fuel designs on the PCI failure potential. To meet these objectives, it is imperative to develop a high-fidelity, fully coupled computer code that incorporates important plant operating procedures, e.g. power ramp rate and axial power shapes related to fuel performance, as well as considering the inherently coupled intricacies that occur in irradiated fuel behavior during normal and transient operations. By developing and employing an advanced fully coupled multi-physics and multi-dimension fuel performance code and developing mechanistic or physics based material models, efforts can be taken to reduce the uncertainties surrounding existing PCI failure methods. The approach to address the current uncertainties in PCI failure probabilities will allow for improved fuel utilization and increase the plant operating flexibility.

In this dissertation, I have utilized the Bison code to evaluate its potential as a next-generation, 3D fuel performance modeling code with predictive capability. This evaluation first involved a series of benchmarks and validation exercises, which indicated that Bison appears to be reliably calculating reasonable fuel centerline temperatures compared to Falcon and the experimental measurements. However, there remain several fuel and materials related models and phenomena that Bison must incorporate. These include correctly accounting for the partitioning of nuclear fission energy and distribution of the volumetric heat generation rate, improvements in the gap closure and gap thermal conductivity models, as well as continued optimization of the penalty model for pellet – clad contact. Furthermore, gap thickness in IFA fuel is primarily driven by fuel thermal expansion, and it seems apparent that the differences between Bison and Falcon at relatively low burnups are associated with predicting gap thickness

and fuel – clad gap closure could be related to differences in the models of fuel thermal expansion at temperatures between 300 K- 700 K. It is also evident that Bison predicts much lower fuel temperatures than the Falcon code, and the results presented in Figure 2-2 show that the fission gas release and swelling model implemented in Bison requires further work, which is also expected to influence the code predictions of clad deformation. More detailed comparisons between Falcon and Bison have indicated differences between the two for gap closure and gap conductance, which highlight the need to continue to refine and improve the physical fidelity of a number of key sub-models, including fission gas release, fuel creep and densification, gap conductance and the smeared crack and relocation models; all of which will impact the temperature distributions within the fuel.

Preliminary assessment of mechanical models and fission gas release models indicates that the Bison code has similar capabilities compared to the Falcon code. Reasonable agreement with experimental data can be achieved for most cases in terms of the calculation of cladding creep down, capturing the low fission gas release regime, and simulating the high fission gas release during a power transient. Areas of improvements involving complex interactions between multiple mechanisms are identified. Expansion of the current V&V database is needed to further test current codes' capability and to assist the development towards a more physics-based model. The results highlight the importance of several aspects of fuel rod behavior; particularly pellet cracking and relocation, and fission gas release. The advanced 3-D modeling capabilities of Bison will require a more mechanistic representation of these behavior in order to model the fundamentals of PCI.

The results of an assessment of idealized conditions of PCI have demonstrated that the pellet cladding mechanical interaction (PCMI) 2-D and 3-D modeling capabilities in Bison are consistent with PCI modeling approaches used by EPRI in the Falcon fuel behavior code [43, 44] and CEA with the ALCYONE code [54]. By representing idealized cracked or defected pellet geometries using 2-D and 3-D finite element meshes, Bison is able to calculate the local stress distributions at the clad inner surface that are important for determining the initiation and propagation of stress corrosion cracks. This preliminary work on modeling fuel cracks and MPS in a full 3-D representation finds that 3-D geometric effects should be considered for mechanistic evaluations of PCI failure with MPS defect.

The results of the BISON fuel performance modeling in 2D (R-Z or R-**θ**) are broadly consistent with current industry code capabilities, and the 3D modeling capability clearly provides a unique capability to industry. As with other assessments performed previously in the literature [59,60,64,74], the evaluation of fuel failure data from test reactor ramp tests indicates that the maximum hoop stress and SED based criteria will not adequately isolate failed rods from non-failed fuel rods. The comparison of the 3-D cladding stress calculations with those obtained by others show excellent agreement for the geometric effect on the maximum cladding hoop stress for a finite length MPS defect. Stress reduction factors of 7 to 16% for finite length MPS defect were calculated by Bison using a 5-pellet model, which agrees well with the values previously calculated by EPRI using ABAQUS. When applying these factors to the 2-D stress calculations, the Bison results correlate closely with those published by AREVA and are lower than those reported by EPRI. Further, these methods are quite statistically sensitive to the assumptions used in the hoop stress and SED calculations. It appears that as a metric, neither the

peak cladding hoop stress nor the SED alone, is sufficient to define rod failure. As a result, implementation of the failure probability thresholds defined by stress or SED could over conservatively restrict reactor operation.

The fuel history from several fuel rods from a commercial reactor during operation in cycle 10 and startup to cycle 11, for which multiple fuel failures were observed to occur, and these fuel operating histories were used to evaluate the overall fidelity of the BISON fuel performance modeling. The BISON analysis demonstrated that both cladding hoop stress and SED increased significantly during the startup ramp between cycle 10 and the startup to cycle 11. The increase in these two possible failure indicators was caused by pellet-cladding mechanical interaction as a result of the fast startup ramp rate and the axial flux change. The BISON analysis in both 2D and 3D clearly indicated that the presence of a MPS was the cause for fuel rod M16S_O05 to have failed. Further, two other failed fuel rods, namely, M19S_I02 and M12S_B06 both showed significantly lower PCI stress values when compared to other failed rods, and this analysis therefore strongly indicates that MPS, or another fuel flaw, was the root cause for the failure of these rods. Lastly, a demonstration of reactor startup power ramps has shown one possible power hold and ramp combination that has the ability to significantly reduce the maximum clad hoop stress and presumably minimize the potential for PCI related cladding failure. The potential for classical PCI based failures for higher burnup fuel than the rods analyzed in the current study remains for future consideration.

Finally, establishing the fuel rod conditions prior to a power maneuver remains a critical element to modeling the potential for PCI failure. Further work on BISON will focus on integrating micro-scale models under development in CASL-FMC that describe the irradiation creep and growth of zirconium alloys, the fracture, relocation, and mechanical compliance of the fuel pellet, and the release of fission products important for SCC (volatile and noble gases). The incorporation of these models into BISON, either directly or using improved semi-empirical relationships, will require expanding the validation activities of BISON to include more integral fuel rod irradiations, hot-cell examination data from commercial reactor fuel rods, and separate effects experiments.

List of References

1.B. Cox, Pellet Cladding Interaction (PCI) Failures of Zirconium Alloy Fuel Cladding – A Review, Journal of Nuclear Materials, 172 (1990) 249-292
2.M. F. Lyons, D. H. Coplin and C. G. Jones, GE Quarterly Progress Reports, GEAP - 3771-10 to -12 (1963/64)
3.J.T.A. Roberts and F.E. Gelhaus, "Zircaloy Performance in Light Water Reactors," Zirconium in the Nuclear Industry (Fourth Conference), ASTM STP 681, ASTM, 1979, pp. 19-39
4.F. Garzarolli, R. von Jan, H. Stehle, The Main Causes of Fuel Element Failure in Water-Cooled Power Reactors, Atomic Energy Review, **17**, 1 (1979)
5.Roberts, J.T.A., "Structural materials in nuclear power systems," Plenum Press, 1981, pp. 53-60.
6.M. Billaux and H. Moon, Pellet-Cladding Mechanical Interaction in Boiling Water Reactor, Proceedings of the International Seminar on Pellet Cladding Mechanical Interaction, OECD/NEA, 9-11 March 2004, Aix-en-Provence.
7.F. Bentejac and N. Hourdequin, TOUTATIS, An Application Of The Cast3M Finite Element Code For PCI Three-Dimensional Modelling, Proceedings of the International Seminar on Pellet Cladding Mechanical Interaction, OECD/NEA, 9-11 March 2004, Aix-en-Provence.
8.C. Powers, et.al., "Hot Cell Examination Results of Non-Classical PCI Failures at La Salle," Paper No. 1141, Proceedings of the 2005 Water Reactor Fuel Performance Meeting, October 2-6, 2005, Kyoto, Japan.
9.F. Groeschel, G. Bart, R. Montgomery, S. K. Yagnik, "Failure Root Cause of a PCI Suspect Liner Fuel Rod", IAEA Technical Meeting on Fuel Failure, Bratislava, Slovakia, 17-21 June 2002.
10. M. Billone, R. Montgomery, Y.R. Rashid, and J. Head, "Advancements in the behavioral modeling of fuel elements and related structures," Nucl. Engrg. Des. 134, (1992), 23-36.
11. Y. R. Rashid, "Mathematical Modeling and Analysis of Fuel Rods," Nucl. Engrg. Des, 29 (1974), 22-32.
12. K. Lassmann, "The structure of fuel element codes," Nucl. Engrg. Des. 57 (1980) 17-39.
13. J. H. Gittus, "Theoretical Analysis of the Strains Produced in Nuclear Fuel Cladding Tubes by the Expansion of Cracked Cylindrical Fuel Pellets," Nucl. Engrg. Des. 18 (1972) 69-82.
14. B. Julien, et.al., 'Performance of Advanced Fuel Product Under PCI Conditions," Proceedings of the 2004 International Meeting on LWR Fuel Performance Orlando, Florida, September 19-22, 2004, Paper 1073.
15. M. Billaux, "Modeling Pellet-Cladding Mechanical Interaction and Application to BWR Maneuvering," Proceedings of the 2004 International Meeting on LWR Fuel Performance Orlando, Florida, September 19-22, 2004, Paper 1047.
16. Y. Farawila and M. Billaux, "XEDOR – Reduced Order Stress Model for Online Maneuvering of Boiling Water Reactors," Proceedings of the 2007 International LWR Fuel Performance Meeting, San Francisco, California, September 30 – October 3, 2007, Paper 1059.
17. W. Lyon, R. Montgomery, Y. Rashid, "PCI Analysis and Fuel Rod Failure Prediction using FALCON," Proc. TOP FUEL '09, Paris, France, 2009.

18. S. Nesbit, M. Kennard, S. Yagnik, “Use of Core Analyses in Assessments of Fuel Failure Risk due to Pellet-Cladding Interaction,” Proc. ANS 2009, Topical Meeting ANFM 2009, p. 1-20.
19. D.D. Baron, L. Hallstadius, 2.19 - Fuel Performance of Light Water Reactors (Uranium Oxide and MOX), In: Editor-in-Chief: Rudy J.M. Konings, Editor(s)-in-Chief, Comprehensive Nuclear Materials, Elsevier, Oxford, 2012, Pages 481-514, ISBN 9780080560335, http://dx.doi.org/10.1016/B978-0-08-056033-5.00040-9.
20. Analysis of and Start-up Profile Recommendations for Exelon PWRs: FALCON Analysis of Failures in Braidwood 1 Cycle 11 Start-up and Braidwood 2 Cycle 10, and Recommendations for the Byron 2 Cycle 13 Start-up. EPRI, Palo Alto, CA: 2006. 1012915.
21. Y. Aleshin, C. Beard, G. Mangham D. Mitchell, E. Malek, M. Young, “The Effect of Pellet and Local Power Variations on PCI Margin,” Paper 41, Proceedings of Top Fuel 2010, Orlando, September 2010.
22. General Electric Advanced Technology Manual Chapter 4.4 Pre-Conditioning Interim Operating Management Guidelines, Rev 1210, NRC ADAMS, ML11263A326.
23. R. von Jan, W. Hering, “Experience and plans with PCI protection in KWU LWR plants, Nucl. Engrg. Des., 65, (1981) 313-318.
24. R. von Jan, “Strategy And Experience of PCI Protection and Load Following Operation In KWU LWR Plants,” Power Ramping, Cycling And Load Following Behaviour of Water Reactor,” Fuel Proceedings of a Technical Committee Meeting, IAEA-TC-624/31, Lyon, France, 18-21 May 1987.
25. Fuel Reliability Guidelines: Pellet-Cladding Interaction. EPRI, Palo Alto, CA: 2008. 1015453.
26. Y. Farawila, K. Wei, and R. Grummer, “XEDOR Evaluation of PCI Fuel Failure Risk due to Loss of Feedwater Heating in Boiling Water Reactors,” Paper No. 8142, Proceedings of the 2008 Water Reactor Fuel Performance Meeting, October 19~23, 2008.
27. *Eyeing PCI on the fly*, Nuclear Engineering International, September 2011.
28. Rashid, Y.R., Montgomery, R.O., Lyon, W.F. and Yang, R., A cladding failure model for fuel rods subjected to operational and accident transients, Paper 3.5, IAEA Technical Committee Meeting on Nuclear Fuel Behaviour Modelling at High Burnup and Its Experimental Support, June 18-23, 2000, Windermere, UK.
29. Fuel Reliability Guidelines: Pellet-Cladding Interaction. EPRI, Palo Alto, CA: 2008. 1015453
30. D. Gaston, C. Newman, G. Hansen, and D. Lebrun-Grandie, “MOOSE: parallel computational framework for coupled systems of nonlinear equations. Nucl. Eng. Design,” 239, p. 1768–1778, 209
31. Montgomery, R., et al., "Peregrine: Advanced Modeling of Pellet-Cladding Interaction (PCI) Failure in LWRs," Proceedings of the TopFuel 2012 Reactor Fuel Performance Conference, Manchester, United Kingdom, September 2-6, 2012
32. Y. R. Rashid, “Mathematical Modeling and Analysis of Fuel Rods,” Nucl. Engrg. Des., 29 (1974), 22-32.
33. *Fuel Analysis and Licensing Code: Falcon MOD01: Volume 1: Theoretical and Numerical Bases,* EPRI, Palo Alto, CA: 2004. 1011307.
34. Terje Tverberg, Masaki Amaya, "Study of thermal behaviour of UO2 and (U,Gd)O2 to high burnup (IFA-515)," HWR-671, February 2001

35. BISON Theory Manual (Draft), Idaho National Laboratory, June, 2013.
36. D. L. Hagrman et al., “MATPRO – Version 11 (Revision 2) A Handbook of Materials Properties for Use in the Analysis of Light Water Reactor Fuel Rod Behavior,” NUREG/CR-0479, TREE-1280, Nuclear Regulatory Commission and EG&G (1981).
37. P. M. Crosby and C. Vitanza, "Irradiation of the Pellet Roughness Rig IFA-562 Progress Report March 1988," HWR-238, March 1988.
38. M. R. Smith, "Final Report on the In-pile Results from the Pellet Roughness Test in Rig IFA-562," HWR-245, November 1989.
39. "The Third RisØ Fission Gas Project ANF Fuel (ANF-Data)," RISØ-FGP3-ANF, Pt.1, Sep. 1990.
40. "The Thrid RisØ Fission Gas Project BUMP Test AN8 (CB10)," RISØ-FGP3-AN8, Sep. 1990.
41. S. Djurle, "Final Report of the Super-Ramp Project," STUDSVIK-STSR-32, Dec. 1984.
42. R. O. Montgomery et al, “Peregrine: Validation and Benchmark Evaluation of Integrated Fuel Performance Modeling Using Test Reactor Data and Falcon,” L1.CASL.P7.02., June, 2013
43. Fuel Analysis and Licensing Code: Falcon MOD01: Volume 1: Theoretical and Numerical Bases, EPRI, Palo Alto, CA: 2004. 1011307.
44. N. Marchal et al, “Finite element simulation of Pellet-Cladding Interaction (PCI) in nuclear fuel rods,” *Computational Materials Science*, 45 (2009) 821-826.
45. Masaomi Oguma, “Cracking and Relocation Behavior of Nuclear Fuel Pellets during Rise to Power,” *Nuclear Engineering and Design* 76 (1983) 35-45
46. J. Rashid et al, “Modelling of PCI under steady state and transient operating conditions,” Technical committee on water reactor fuel element computer modelling in steady state, transient and accident conditions, Preston (UK) 18-22 Sep 1988, pp. 91-101
47. W. Lyon, R. Montgomery, Y. Rashid, “PCI Analysis and Fuel Rod Failure Prediction using FALCON,” Proc. TOPFUEL ’09, Paris, France, 2009.
48. B. Michel, J. Sercombe, G. Thouvenin, "A new phenomenological criterion for pellet cladding interaction rupture," *Nuclear Engineering and Design* 238 (2008) 1612–1628.
49. N. Marchal et al, “Finite element simulation of Pellet-Cladding Interaction (PCI) in nuclear fuel rods,” *Computational Materials Science*, 45 (2009) 821-826.
50. Fuel Reliability Guidelines: Pellet-Cladding Interaction. EPRI, Palo Alto, CA: 2008. 1015453
51. J.T.A. Roberts and F.E. Gelhaus, “Zircaloy Performance in Light Water Reactors,” Zirconium in the Nuclear Industry (Fourth Conference), ASTM STP 681, ASTM, 1979, pp. 19-39
52. Chris Powers, Peter Dewes, and Michel Billaux. "Hot cell examination results of non-classical PCI failures at La Salle," Proceedings of the Water Reactor Fuel Performance Meeting 2005, Kyoto, (2005).
53. Sylvie Lansiart and Bruno Michel, Pellet Cladding Interaction, Nuclear Fuels, CEA Nuclear Energy Division Monograph, Jean-François Parisot, Ed, CEA, 2009.
54. Sercombe,J., Michel,B., Thouvenin,G., Petitprez,B., Chatelet,R., Leboulch,D., Nonon,C., 2009. Multi-dimensional modeling of PCMI during base irradiation and ramp testing with ALCYONE V1.
55. EPRI Report 1012915, “PCI Analyses and Startup Ramp Rate Recommendations for Westinghouse Fuel in Exelon PWRs”, (2006).
56. B. W. Spencer, J. D. Hales, D. R. Gaston, D. A. Karpeev, R. L. Williamson, S. R.

Novascone, D. M. Perez, R. J. Gardner, and K. A. Gamble. BISON contact improvements CASL FY14 report. Technical Report INL/EXT-14-33285, Idaho National Laboratory, Idaho Falls, ID, September 2014.
57. D. S. Stafford and B.W. Spencer. Contact memory reduction CASL letter report. Technical report, Idaho National Laboratory, Idaho Falls, ID, January 2015.
58. SIERRA Solid Mechanics Team. Sierra/SolidMechanics 4.22 user's guide. Technical Report SAND2011-7597, Sandia National Laboratories, Albuquerque, NM, October 2011.
59. Turnbull, J.A.; CEA - Dept. des Reacteurs Nucleaires, 91191 Gif-sur-Yvette Cedex (France).
60. S. Djurle, "Final Report of the Super-Ramp Project," STUDSVIK-STSR-32, Dec. 1984.
61. S. Djurle, "Final Report of the Over-Ramp Project," STUDSVIK-STSR-37, Dec. 1980.
62. R. O. Montgomery et al, "Peregrine: Validation and Benchmark Evaluation of Integrated Fuel Performance Modeling Using Test Reactor Data and Falcon," L1.CASL.P7.02, June, 2013.
63. N. Capps, R. Montgomery, D. Sunderland, M. Pytel, and B.D. Wirth, "Evaluation of Missing Pellet Surface Geometry on Cladding Stress Distribution and Magnitude", Nuclear Engineering and Design (2015) under review.
64. Corie Glenn and Tyrone L. Stevens, Exelon Corp., personal communication (2015).
65. EPRI Report 1012915, "PCI Analyses and Startup Ramp Rate Recommendations for Westinghouse Fuel in Exelon PWRs", (2006).
66. Turnbull, J.A.; Studsvik Nuclear AB, SE-611 82 Nykoeping (Sweden).
67. Turnbull, J.A.; CEA - Dept. des Reacteurs Nucleaires, 91191 Gif-sur-Yvette Cedex (France).
68. W. Lyon, R. Montgomery, Y. Rashid, "PCI Analysis and Fuel Rod Failure Prediction using FALCON," Proc. TOP FUEL '09, Paris, France, 2009.
69. Westinghouse Letter PPE-05-159, "Generic Data Requirements for PCI Analysis," dated July 7, 2005.
70. Westinghouse Letter PCT-05-542, "Rod Power history Data for transmittal to ANATECH," July 1, 2005.
71. Westinghouse Letter PPT-05-54, "ANC Identification of Failed Rods in Braidwood Unit 1," July 5, 2005
72. Westinghouse Letter PCT-05-556, "Rod Power history Data for transmittal to ANATECH," July 14, 2005
73. Sabol, G. P., Comstock, R. J., Weiner, R. A., Larouere, P., and Stanutz, R. N., " In-Reactor Corrosion Performance of ZIRLO and Zircaloy-4," Zirconium in the Nuclear Industry: Tenth International Symposium, ASTM STP 1245, A. M Garde and E.R. Bradley, Eds.. American Society for Testing and Materials, Philadelphia, 1994. p 724-744.
74. M. F. Lyons, D. H. Coplin and C. G. Jones, GE Quarterly Progress Reports, GEAP - 3771-10 to -12 (1963/64)
75. Y. Aleshin, C. Beard, G. Mangham, D. Mitchell, E. Malek, and M. Young, "The Effect of Pellet and Local Power Variations on PCI Margin", Proceedings of Top Fuel 2010, September 26-29, 2010, Orlando, FL, USA, Paper 041.
76. Shah, Hemant, Aleshin, Yuriy, Sutharshan, Balendra ., Borell, Sten, & Widegren, Hans (2007). Enhanced fuel performance by improving pellet quality and fabrication technology. Proceedings of the ICONE-15 (Revised) The 15th international conference on nuclear engineering, (p. 3174). Japan: Japan Society of Mechanical Engineers.
77. S. Palmtag, CASL, personal communication (2015).

Vita

Nathan Allen Capps was born in Fort Smith, Ar to the parents of Barbara and Thomas Capps. He attended Van Buren High School, where he was a two year varsity starter in football and a three year starter in baseball. He attended the University of Arkansas at Fort Smith, where he played baseball for a year and a half. Upon transferring to the University of Tennessee at Knoxville, he earned a Bachelor of Science degree in Nuclear Engineering in May of 2012. He accepted a Graduate Research Assistant position within the Nuclear Engineering Department at the University of Tennessee upon graduation in 2012. Nathan earned a Master of Science degree in Nuclear Engineering in December of 2013, and will earn his PhD in Nuclear Engineering on May 12th 2016